Editor summary:

Benoit and colleagues identify the dopamine transporter antagonist vanoxerine as a suppressor of the G9a methyltransferase. Show that treatment leads to cancer stem cell suppression and restoration of an immune-responsive tumor microenvironment in CRC.

Peer Review Information:

Nature Cancer thanks Toshiro Sato and the other, anonymous, reviewer(s) for their contribution to the peer review of this work.

Figure or Table # Please group Extended Data items by type, in sequential order. Total number of items (Figs. + Tables) must not exceed 10.	Figure/Table title One sentence only	Filename Whole original file name including extension. i.e.: Smith_ED_Fig1.jpg	Figure/Table Legend If you are citing a reference for the first time in these legends, please include all new references in the main text Methods References section, and carry on the numbering from the main References section of the paper. If your paper does not have a Methods section, include all new references at the end of the main Reference list.
Extended Data Fig. 1	Supporting information on the high-throughput phenotypic assay used to identify cancer-selective inhibitors of H3K9me2 deposition	Bergin_ED_Fig1.jpg	**a,** OCT4 staining on t-hESCs upon drug treatments (5 μM, 48 h) and DMSO control (left panel, scale bar: 50 μm). Flutamide, clomiphene, and colistin sulfate are example of drugs tested for loss-of-pluripotency (n=2 biological replicates, 1 independent experiment). Quantification of OCT4-positive cells vs. counts scored from a validation set of 142 compounds relative to DMSO control (right panel). Values are expressed as log2 fold-changes (L2FC). Dashed box indicates loss-of-pluripotency hits (cut off: L2FC > -1.0). **b,** H3K9me2 immunostaining on t-hESCs treated with loss-of-pluripotency inducers (5 μM, 48 h, n=2 biological replicates from 2 independent experiments, scale bar: 100 μm). Thioridazine and niclosamide are examples of drugs further tested for H3K9me2 deposition. The G9a inhibitor

			BIX-01294 (1 μM, 48 h) was used as positive control. **c,** Quantification of H3K9me2 immunostaining signal in t-hESC cells vs. cell count scored for each loss-of-pluripotency inducer relative to DMSO. CWP232228 (100 nM, 48 h) and BIX-01294 (1 μM, 48 h) were used as positive controls for cell count and H3K9me2 inhibition, respectively (dashed lines) (n=2 biological replicates from 2 independent experiments). Prioritized hits (vanoxerine (VXN), niclosamide, clomiphene) were identified in circles. **d,** Heat map of the mean immunodetection signal from assessing total 5-methylated cytosine (5-meC) and histone marks H3K9me2, H3K9me3, and H3K27me3 levels in t-hESCs treated with different candidates vs. DMSO control (5 μM, 48 h, n=3 biological replicates from 3 independent experiments, color scale: Log2 fold-change signal vs. vehicle, cut off: >0.25). BIX-02492 (1 μM) and DZNep (1 μM) (S-adenosylhomocysteine synthesis and EZH2 inhibitor) were used as positive controls. **e,** Cancer-selective toxicity assessment for clomiphene and niclosamide using the human CRC cell lines HT29 (n=4 biological replicates), SW480 (n=3 biological replicates), and HCT116 (n=3 biological replicates) vs. normal intestinal progenitor line HIEC (n=6 biological replicates). Data from 1 independent experiment were best-fitted using a nonlinear curve fitting model. **f,** Dose-response cell growth experiment evaluating the EC50 of VXN in HT29 cells for 48 h vs. 72 h treatments (n=4 biological replicates from 1 independent experiment). **g,** Cell growth analysis comparing 2.5μM VXN treatments over 72 h vs. control in 3 independent cell lines from human colorectal, melanoma, ovarian, prostate, liver, lung, breast,

			glioblastoma, and kidney tumors (Data from 1 independent experiment, number of biological replicates (n) and p-values are indicated on graphs, mean values +/- SEM, unpaired multiple t-tests). See also Fig. 1, Supplementary Tables 1-3, Supplementary Note 1.
Extended Data Fig. 2	Transcriptomic profiling of cancer-selective effects of vanoxerine treatments	Bergin_ED_Fig2.jpg	**a,** Fold-change comparison plot of differentially expressed genes upon VXN treatments (10 μM, 48 h) vs. DMSO in HT29 and HIEC cells (n=2 biological replicates from 1 independent RNA-seq experiment, $p<0.05$). "HT29_VXN" represents the cancer-selective transcriptional signature to VXN treatments. **b,** GSEA plots showing a downregulation of genes overexpressed in human colorectal adenomas (Sabates) within the VXN cancer-selective signature in CRC cell. Such a relationship is not observed in VXN-treated HIEC cells (vs. DMSO). The expression of all SABATES genes highlighted by GSEA are presented in a heat map (RNA-seq data from **a**, Log2 fold-change expression vs. DMSO, NES and NOM p-value were calculated by the GSEA Software version 4.0.3). **c,** Heat map representing the expression of individual genes from curated lists of intestinal differentiation and progenitor (undifferentiated) markers in HIEC and HT29 cells treated with either VXN (10 μM, 48 h) or DMSO control (RNA-seq data from **a**, z-score of FPKM values). **d,** Enrichment plots for the GO_CANONICAL _WNT_SIGNALING_PATHWAY and the DOUGLAS_BMI1_TARGETS_DN (downregulated genes in *BMI1*-knockdown cells) signatures from GSEA performed on differentially expressed genes following VXN treatment (vs. DMSO) in HT29 and HIEC cells (RNA-seq data from **a**, NES and NOM p-value were calculated by the GSEA Software

			version 4.0.3). **e,** Changes of mRNA expression observed for common colon CSC markers upon VXN treatments in HT29 cells (10 μM, 48 h) vs. DMSO controls (Log2 fold-change expression, RNA-seq data from **a**, q-values calculated using the Benjamini-Hochberg's multiple correction testing method are indicated on graph). **f,** Transcriptional stem cell indexes calculated using one-class logistic regression machine-learning algorithm for t-hESC (CSC-like, n=2 biological replicates from 1 independent RNA-seq experiment), HIEC (normal intestinal, RNA-seq data from **a**), HCT116 (CRC, n=1 biological replicate from GSM2891824) and HT29 (CRC, RNA-seq data from **a**) vs. the mRNAsi distribution curve of the colon adenocarcinoma (COAD) patient cohort (TCGA: n=275 patients). **g,** GSEA plots showing a positive correlation between genes selectively modulated by VXN in HT29 cells (vs. DMSO, $p<0.05$) and gene signatures characteristic of a response to type-1 interferon. Such a profile is not observed at a significant level in VXN-treated HIEC cells (vs. DMSO) (NES and NOM p-value were calculated by the GSEA Software version 4.0.3). The expression of all type-1 interferon response genes highlighted by GSEA is presented in a heat map (RNA-seq data from **a**, Log2 fold-change expression) following VXN treatments (vs. DMSO) in HIEC and HT29 cells. See also Fig. 2, Supplementary Tables 4-5.
Extended Data Fig. 3	Comparison of vanoxerine response to other pharmacological compounds	Bergin_ED_Fig3.jpg	**a,** Correlation study of VXN sensitivity across the PRISM repurposing primary screen 19Q3 (top-6 entries). The epigenetic drug romidepsin significantly correlates with the VXN response (Pearson correlation (r) coefficient, two-tailed p-values are presented). **b,** Correlation plots of

			the chemotherapy drug idarubicin and the nootropic compound IDRA-21 vs. VXN for cell growth inhibition in 33 human CRC cell lines (n=33 cell lines, Pearson r test, two-tailed p-values indicated on graphs). **c,** Structure of VXN second-pass metabolite GBR-12935 and its impact on HT29 (CRC) and HIEC (normal) cell viability at 1.25, 2.5, and 5μM vs. DMSO (0μM) (Data from 3 independent experiments, number of biological replicates (n) for each condition is indicated on graphs, mean values +/- SEM, ***: p=0.0008). **d,** Correlation plots of benztropine-mesylate vs. VXN for cell growth inhibition in 33 human CRC and 108 lung cancer cell lines (CRC: n=33 cell lines, lung: n=108 cell lines, Pearson r test). Dashed box represents the expected distribution zone for correlated responses. **e,** Heat maps of mRNA expression for documented H3K9me and 5-meC regulators in HIEC and HT29 cells treated with VXN (10 μM, 48 h) vs. DMSO (n=2 biological replicates from 1 independent RNA-seq experiment, z-score of FPKM values). Adjusted p-values (q-values) calculated based on Benjamini-Hochberg's multiple correction testing method. **f,** Expression of G9a (*EHMT2*) (Data from 2 independent qPCR experiments, DMSO: n=3 biological replicates, VXN: HIEC n=3 and HT29 n=5 biological replicates, ***: p=0.0002, unpaired two-tailed t-test) and GLP (*EHMT1*) (RNA-seq data from **e**, normalized counts) encoding mRNA were measured following VXN treatments in HIEC and HT29 cells (mean values +/- SEM). **g,** Western blot analysis comparing G9a levels in HT29 (cancer) and HIEC (normal) cells. When detectable, G9a levels were decreased by VXN in HIEC cells. Actin was used as loading control (n=3 biological replicates from 3 independent experiments). **h,** Fold-

			change comparison plot of differentially expressed genes upon VXN (10 μM, 48 h) or BIX-1294 (1 μM, 48 h) treatments vs. DMSO in t-hESCs (n=2 biological replicates from 1 independent RNA-seq experiment, $p<0.05$, Benjamini-Hochberg's multiple correction test and false discovery estimation). **i,** Heat map showing mRNA expression of documented H3K9me and 5-meC regulators in t-hESCs treated with VXN (10 μM, 48 h) or BIX-01294 (1μM, 48 h) vs. DMSO controls. Arrows indicating downregulation by VXN but not by BIX. (RNA-seq data from **h**, z-score of FPKM values). **j,** GSEA enrichment plots showing correlations between genes significantly modulated by VXN in t-hESC and apoptosis (HALLMARK_APOPTOSIS), proliferation (E2F_TARGETS), pluripotency (WONG), MYC (HALLMARK_MYC), p53 (HALLMARK_P53), and colorectal cancer (GRADE_COLON_AND_RECTAL_CANCER_UP) signatures (RNA-seq data from **h**, NOM $p<0.05$, NES and NOM p-value were calculated by the GSEA Software version 4.0.3). **k,** Bubble plot of transcription factor binding sites (UCSC_TFBS) enrichment in genes from top-50 upregulated G9a/H3K9me2 target genes upon VXN treatments in HT29 and HIEC cells (ChIP-seq: n=1 sample series, RNA-seq: n=2 biological replicates, 1 independent experiment, one-sided p-values for Fisher's Exact test available in Source Data). See also Fig. 2, Supplementary Tables 4-6, and Supplementary Note 2.
Extended Data Fig. 4	Characterization of DAT as the main target of VXN in colon cancer	Bergin_ED_Fig4.jpg	**a,** Docking poses of VXN and cocaine interaction with DAT X-ray crystallographic structure (PDB 4xp1). The binding pocket surface is highlighted according to electrostatic properties (top). **b,** qPCR analysis of

			SLC6A3 mRNA expression in bulk, heterogeneous organoids and CSC-enriched fractions from primary CRC samples (n=3 biological replicates from 1 patient sample (Patient #92) in 2 independent experiments, mean values +/- SEM, ***: p<0.0001, unpaired two-tailed t-test). HIEC (n=4 biological replicates) and t-hESCs (n=4 biological replicates) were used as low and high-expressing controls for *SLC6A3*, respectively. **c,** UMAP plot of clustering analysis from scRNA-seq profiling (n=23 CRC patient samples). Each cluster represents a cell type-specific signature. Histograms are showing transcript levels of *SLC6A3* and *LGR5*-expressing epithelial and stromal cells across primary CRC tumors (T) and normal colon (N) samples. **d,** Representative micrograph of crypts from human normal colonic tissue showing the absence of DAT in E-cadherin stained epithelial cells (n=3 independent donors, scale bar: 100 μm). **e,** Representative single-cell protein signal observed for total histone H3 (cell occupancy control), DAT, phospho-H3S10, CD133 (colon CSC marker), chromogranin A (enteroendocrine cell marker), and neurofilament (NEFL, neuronal marker) on scWest chips loaded with either patient-derived CSC-enriched spheroids (n=5 CRC patient samples) or M17 neuroblastoma cells (n=3 biological replicates). **f,** Single-cell protein quantification of DAT and CD133-positive cells within primary bulk colorectal adenocarcinoma samples. Scatter plots are showing observed fluorescence intensity per individual cell. DAT-positive are highlighted in red on CD133 plots (n=3 samples, Patients #409 and #397 presented, 3 independent experiments). **g,** Single-cell protein quantification of DAT-positive cells in

			CD133-sorted fractions from primary colorectal adenocarcinomas. Scatter plots are showing observed fluorescence intensity per individual cell (n=2 CRC patient samples from 2 independent experiments). **h,** *SLC6A3* mRNA levels in HCT116 cells transduced with pInducer10-RFP vector containing a non-silencing scrambled control or an *SLC6A3*-targeting shRNA. shRNA expression was induced by doxycycline and qPCR measurements were performed on 90-95% RFP-positive populations (n=6 biological replicates from 2 independent experiments, mean values +/- SEM, ***: p=0.0007, unpaired two-tailed t-test). **I,** Representative micrographs of pInducer10-RFP shCTRL and sh*SLC6A3*-transduced HT29 cells immunostained for DAT. The punctate intracellular staining corresponding to DAT is reduced in RFP-positive sh*SLC6A3* cells (n=3 biological replicates from 2 independent experiments, scale bar: 30 μm). **j,** *SLC6A3* siRNA knockdown decreases growth in HT29 and HCT116 cells, with no additive effects when combined with VXN treatments (48 h, 5 μM) (1 independent experiment, biological replicates (n) and p-values indicated on the graphs, mean values +/- SEM, one-way ANOVA with Tukey's multiple comparisons test). Knockdown efficiency vs. scramble control (siCTRL) was confirmed by western blot (n=3 biological replicates from 3 independent experiments). **k,** Clonogenic spheroid formation experiment using HT29 cells transduced with shCTRL and sh*SLC6A3* pInducer10-RFP system and plated as single cells in Elplasia® microwell plates. Spheroid formation frequency and spheroid size in Dox-induced sh*SLC6A3* (RFP-positive) HT29 cells are presented vs. shRNA controls (n=18 biological replicates from 3 independent

			experiments, mean values +/- SEM, ***: p<0.0001, unpaired two-tailed t-test). **l,** Clonogenic organoid formation assay using si*SLC6A3* knockdown HCT116 cells (vs. siCTRL). Transient knockdown of *SLC6A3* significantly reduces HCT116 organoid formation frequency (n=3 biological replicates from 3 independent experiments, mean values +/- SEM, ***: p=0.0002, unpaired two-tailed t-test). See also Fig. 3-4, and Supplementary Note 3.
Extended Data Fig. 5	Relationship between the impact of vanoxerine on cancer cells and the dopamine pathway	Bergin_ED_Fig5.jpg	**a,** Cell growth experiment measuring the impact of increasing doses of dopamine (0.02 – 20 μM, 48 h) on HT29 cell sensitivity to VXN treatments (10 μM, 48 h, vs. DMSO control) (n=4 biological replicates from 2 independent experiments, ***: p<0.0001, **: p=0.0023, *: p=0.0493, one-way ANOVA with Bonferroni's multiple comparisons test). **b,** ELISA measuring dopamine levels in cell lysates and conditioned growth media from HIEC, HT29, t-hESCs, and primary human colorectal CSC (CCSC) cultures treated with VXN (10 μM, 48 h) or DMSO control. Complete growth media were also tested (n=3 biological replicates from 1 independent experiment, color scale: 1/absorbance 450 nm). Dopamine (DA) standard solutions were used as positive controls (8 – 530 nM). **c,** mRNA levels of putative VXN targets previously documented in the literature (SLC6A3: HIEC n=4 and HT29 n=3 biological replicates from 3 independent experiments. hERG/KCNA5, sigma receptor-1, and sigma receptor-2: n=2 biological replicates from 1 independent RNA-seq experiment), as well as dopamine receptors (n=2 biological replicates from 1 independent RNA-seq experiment) in HIEC (normal) and HT29 (CRC) cells

			(mean values +/- SEM, ***: p<0.0001, unpaired two-tailed t-test). **d,** Dose-response experiments measuring the effect of the sigma receptor-1/2 agonist ditolylguanidine (DTG, n=4 biological replicates) and the sigma receptor-2 antagonist SM-21 (HT29 n=3 and HIEC n=4 biological replicates) on HT29 and HIEC cell growth (48 h, data from 2 independent experiments, mean values +/- SEM, p-values indicated on graphs, two-way ANOVA with Bonferroni's multiple comparisons test). **e,** Cell growth experiment comparing the effect of VXN (10 μM, 48 h) to the dopamine receptor D2 antagonist haloperidol (10 μM, 48 h), in the presence or absence of dopamine (10 μM) vs. DMSO control (n=7 biological replicates from 1 independent experiment, mean values +/- SEM, ***: p<0.0001, **: p=0.0041, one-way ANOVA with Bonferroni's multiple comparisons test).
Extended Data Fig. 6	Impact of vanoxerine on intracellular signaling mechanisms in colon cancer cells	Bergin_ED_Fig6.jpg	**a,** GSEA showing significant enrichment of differentially expressed genes from sh*SLC6A3* (vs. shCTRL) and VXN-treated (10 μM, 48 h,vs. DMSO) HCT116 cells (n=3 biological replicates from 2 independent RNA-seq experiments), and VXN-treated HT29 and HIEC cells (vs. DMSO, n=2 biological replicates from 1 independent RNA-seq experiments) in AKT/mTOR-related transcriptional signatures. Bubble plot represents normalized enrichment scores (NES, color scale) and NOM p-values (circle size) for each gene signature (NES and NOM p-values calculated by the GSEA Software version 4.0.3). **b,** Expression of PI3K/AKT/mTOR target genes (from signatures in **a**) in shCTRL (DMSO and VXN 10 μM, 48 h) and sh*SLC6A3* (DMSO) HCT116 cells. mRNA levels are presented as FPKM values (n=3 biological replicates from 2 independent experiments,

			mean values +/- SEM, p-values indicated on graphs, one-tailed paired t-test). **c,** Extended kinome profiling data on 6 h, 12 h, and 24 h VXN-treated HT29 cells (10 μM) for the phosphorylation state of MAPK, JAK/STAT, p53, and Src family kinases (n=4 biological replicates from 2 independent experiments, *: $p<0.05$, **: $p=0.0019$, ***: $p<0.001$, exact p-values are in Source Data, one-way ANOVA with Bonferroni's multiple comparisons test, color scale: Log2 fold-change signal vs. vehicle). **d,** Western blot analysis of total and phospho-AKT levels (T308: n=3 biological replicates, S473: n=4 biological replicates) in HT29 *SLC6A3* knockdown vs. shCTRL cells. *SLC6A3* knockdown was confirmed by western blotting, and actin was used as a loading control (Data from 2 independent experiments). **e,** STRING analysis performed on the DAT interactome from the BioGRID database plus hits from the kinome profiling experiments in HT29 cells. Shell-connecting edges are based on interaction confidence (medium threshold: 0.4), and Kmean clustering analysis was performed to identify functional clusters related to the AKT-mTOR pathway and colorectal cancer (Cluster-1), dopamine processing (Cluster-2), and microtubules (Cluster-3). Dashed edges represent supported inter-cluster interactions. **f,** Western blot analysis of active and total β-catenin, and E-cadherin in VXN-treated (10 μM, 48 h vs. DMSO) and sh*SLC6A3* (vs. shCTRL) HT29 cells. OD signal quantification of active vs. total β-catenin and E-cadherin vs. actin is presented in bar graphs (n=3 biological replicates from 1 independent experiment, mean values +/- SEM, ***: $p=0.0007$, *: $p=0.0120$, unpaired two-tailed t-test). **g,** High-content immunofluorescence imaging analysis of E-

			cadherin and β-catenin distribution in DMSO (n=4 biological replicates), VXN-treated (10 μM, 48 h, n=5 biological replicates), shCTRL (n=4 biological replicates), and sh*SLC6A3* (n=4 biological replicates) HT29 cells. Signal colocalization analysis suggests increased adherens junction assembly in VXN-treated cells (4 independent experiments) but not in *SLC6A3* knockdown cells (1 independent experiment). Mean values +/- SEM, ***: p=0.0004, unpaired two-tailed t-test, scale bar: 30 μm). See also Fig. 4, and Supplementary Table 9.
Extended Data Fig. 7	Impact of vanoxerine on *EHMT2* promoter regulation in colon cancer cells	Bergin_ED_Fig7.jpg	**a,** Western blot analysis of total Nur77 levels in HCT116 cells treated with DMSO, AZD5362 (AKTi, 2.5 μM), and VXN (5μM) over 24 h (n=2 biological replicates from 1 independent experiment). Actin was used as a loading control. **b,** Expression of target genes transactivated by Nur77. mRNA levels in DMSO and VXN-treated HT29 and HIEC cells are presented (relative expression vs. DMSO, n=2 biological replicates from 1 RNA-seq experiment). **c,** SPP analysis of ChIP-seq data from the ChIP-Atlas database integrating MACS2 binding scores of different transcription factors around the transcription start site of *EHMT2* (+/- 10 kb). Each dot corresponds to an independent biological sample. Dashed boxes highlight candidate transcription factors enriched at the *EHMT2* promoter in several biological samples and representing potential regulators of G9a expression (CTCF, CEBPβ, and ZNF143). **d,** ChIP analysis of CEBPβ and ZNF143 transcription factor enrichment at the *EHMT2* proximal promoter in HCT116 cells treated with VXN (5 μM, 24 h) vs. DMSO controls (n=6 biological replicates from 4 independent experiments,

			mean values +/- SEM, p-values indicated on graph, unpaired two-tailed t-test). **e,** RRBS data from the ENCODE project database showing 5-methylated cytosine distribution around the *EHMT2* transcription start site in human normal and neoplastic tissues (Each row corresponds to 1 independent biological sample). **f,** Western blot analysis of G9a levels in pLenti CTRL (empty) and pLenti-G9a-transduced HCT116 cells treated with DMSO or VXN (10 μM, 48h). Relative G9a vs. actin OD ratios are presented in the bar graph (n=3 biological replicates from 2 independent experiments, mean values +/- SEM, **: p=0.0090, unpaired multiple t-tests). See also Fig. 5.
Extended Data Fig. 8	Vanoxerine inhibits tumor-initiating function in patient-derived colon cancer tissue samples	Bergin_ED_Fig8.jpg	**a,** Western blot analysis of G9a levels and H3K9me2 deposition following 48 h of VXN (5 μM) or BIX-01294 (1 μM) treatment (vs. DMSO controls) in HT29 (2D cultures) and patient-derived CSC-enriched spheroids (n=4 biological replicates from 3 independent experiments). Actin was used as a loading control. Optical density signal ratios for G9a and H3K9me2 vs. loading control are presented. **b,** Representative whole-well brightfield imaging of patient-derived CRC organoids from primary organoid series treated with increasing doses of VXN (7 days, 0.25 - 10μM) vs. DMSO controls (n=5 CRC patient samples, Patient #92 is presented). **c,** Relative size assessment of primary organoids treated with VXN (7 days, 0.25 - 10μM) vs. DMSO (n=5 CRC patient samples from 5 independent experiments, mean values +/- SEM, ***: p<0.0001, one-way ANOVA with Dunnett's multiple comparisons test). **d,** Representative whole-well brightfield imaging of secondary patient-derived CRC organoids from the primary series treated with 0.25 and 0.5

			μM of VXN vs. DMSO controls (n=5 CRC patient samples, Patient #181 is presented). **e,** Patient-specific response in secondary organoid formation assays for VXN-treated primary samples (0.25, 0.5, and 1μM) vs. DMSO controls (n=5 CRC patient samples). **f,** Representative whole-well brightfield imaging of donor-derived normal colonic organoids from primary and secondary plating series, treated with increasing doses of VXN (7 days, 0.25 - 1μM) vs. DMSO controls (n=5 biological replicates from 1 healthy tissue sample in 5 independent experiments). **g,** Secondary normal colonic organoid formation frequency observed upon VXN (0.25 - 10 μM, 7 days) vs. DMSO controls (n=5 biological replicates from 1 healthy tissue sample in 5 independent experiments, *: p=0.0112, one-way ANOVA with Dunnett's multiple comparisons test). Box plot center line corresponds to median, and whiskers represent min to max values. **h,** qPCR analysis of colon CSC markers as well as *SLC6A3* and *EHMT2* in MACS-sorted $CD133^{Low}$ and $CD133^{High}$ fractions isolated from CSC-enriched spheroids derived from 2 independent primary colon adenocarcinomas (*PROM1*: $CD133^{High}$: n=8, $CD133^{Low}$: n=9), *LGR5*: $CD133^{High}$: n=5, $CD133^{Low}$: n=6, *SLC6A3*: $CD133^{High}$: n=8, $CD133^{Low}$: n=9, *EHMT2*: $CD133^{High}$: n=6, $CD133^{Low}$: n=8). n. corresponds to biological replicates from 2 independent experiments, p-values are indicated on graphs, mean values +/- SEM, unpaired two-tailed t-test). **i,** Mean spheroid size measured from clonogenic experiments using $CD133^{High}$ (n=12 biological replicates) and $CD133^{Low}$ (n=11 biological replicates) fractions, treated with VXN (0.5 μM, 48 h) or DMSO control (Data from 2 CRC patient samples, in 11

			independent experiments, mean values +/- SEM, ***: p<0.0001, unpaired two-tailed t-test). **j,** Targeting strategy for the generation of patient-derived *LGR5-GFP* CRC organoids using a CRISPR-Cas9 knock-in system, where construct integration and endogenous *LGR5* expression is visualized via an RFP and a GFP reporter, respectively. *EF1-RFP-Puro* cassette was removed via transduction with Cre-expressing adenoviral particles (Ad-Cre). PCR reactions using primer pairs a/b and c/e detected knock-in of the 5′ and 3′ arms, respectively, in organoids treated with ad-Cre. Primer pair d/e detected the *RFP-puro* selection cassette in organoids not treated with Ad-Cre. Non-engineered parental patient sample was used as control (n=3 biological replicates from 1 CRC patient sample, in 3 independent experiments). **k,** CRC patient-derived *LGR5-GFP* cells were used in clonogenic organoid formation assay, treated with VXN (0.5 and 1.0 μM) or DMSO, and analyzed by high-content imaging for GFP signal at day-0, day-7, day-10, and day-14. Representative images of CRC *LGR5-GFP* organoids at each stage of the experiment (VXN 0.5 and 1.0 μM vs. DMSO, image acquisition at 4X, n=6 biological replicates from 4 independent experiments, scale bar: 30μm). **l,** Quantification of "LGR5-positive" primary organoids across all counted structures at day-0, day-7, day-10, and day-14 for DMSO and VXN (0.5 and 1 μM, 7 days) treatments (n=6 biological replicates from 4 independent experiments, mean values +/- SEM, p-values indicated on graph, two-way ANOVA with Dunnett's multiple comparisons test). **m,** Box plot (left) showing *LGR5-GFP* secondary organoid formation frequency observed for VXN (0.5 and 1 μM, 7 days) and DMSO-treated groups (n=6 biological replicates from 4

			independent experiments, ***: p<0.0001, one-way ANOVA with Dunnett's multiple comparisons test). Box plot center line corresponds to median, and whiskers represent min to max values. Violin plot (right) representing integrated GFP intensity per organoid was measured by high-content imaging in residual secondary organoids from each group (DMSO: n=1518 organoids, VXN 0.5 μM: n=287 organoids, VXN 1 μM: n=216 organoids). Dashed line within violin plots corresponds to median. See also Fig. 6, and Supplementary Table 8.
Extended Data Fig. 9	Impact of *in vivo* vanoxerine treatments on H3K9me2 deposition, tumor development, and normal tissue architecture	Bergin_ED_Fig9.jpg	**a,** Dose-response curves of VXN impact on the growth of mouse MC38 (C57BL/6) and CT26 (BALB/c) cell lines. Concentrations ranging from 0.32 to 20 μM were used over 48 h (Data from 3 independent experiments, number of biological replicates per dose/condition (n) is indicated on graphs, points represent mean values +/- SEM) vs. DMSO control. Data were best-fitted using a nonlinear curve fitting model, and the calculated EC50 is presented for each cell line. **b,** Assessment of *SLC6A3* mRNA levels (qPCR) in parental 2D cultured and primary *in vivo* MC38 tumors. GAPDH was used as housekeeping gene (n=6 biological replicates from 3 independent experiments, ***: p=0.0002, unpaired two-tailed t-test). **c,** Volcano plots representing modulation of gene expression in VXN-treated (25 mg/kg, 10 days) primary MC38 tumors vs. vehicle (saline) controls (n=2 biological replicates from 1 independent RNA-seq experiment). Dashed lines represent p-value <0.05 and ±1.0 log2 fold-change (L2FC) (Benjamini-Hochberg's multiple correction test and false discovery estimation). Clustering analysis of transcriptional responses to VXN (V) and vehicle (CTRL, C) treatments in each tumor sample is presented as an inset.

			d, Western blot analysis of G9a levels in primary syngeneic *in vivo* tumors (MC38 – C57BL/6) following 10 days of VXN treatments (25 mg/kg) vs. vehicle controls. Actin was used as loading control (n=3 independent tumor pairs from 2 independent experiments, mean values +/- SEM, *: p=0.0307, unpaired two-tailed t-test). **e,** Flow cytometry analysis of mouse stem cell antigen Sca-1 and CD44 levels in single-cell dissociated mouse primary tumors (MC38 – C57BL/6) from 10-day VXN-treated and vehicle control recipients (n=3 biological replicates from 1 independent experiment). Histograms show decreases in both stemness markers across live cell populations following VXN treatments. **f,** Schematic of immunofluorescence-based histological analysis performed on CRC tumors resected from mouse primary recipients (VXN vs. vehicle) and visualized by high-content imaging (HCI). **g,** Representative HCI-acquired images from mouse primary tumor histological sections stained for H3K9me2 and DAPI. Automated scoring of H3K9me2-positive cells across the whole scans are presented for VXN (n=14 tumors) and vehicle-treated (n=26 tumors) mouse recipients (fluorescence signal vs. HCI mask are presented, 3 independent experiments, scale bar: 2 mm). **h,** Western blot analysis of H3K9me2 levels in primary syngeneic *in vivo* tumors (MC38 – C57BL/6) following 10 days of VXN treatments (25 mg/kg) vs. vehicle controls. Total histone H3 was used as loading control (n=4 independent tumor pairs from 2 independent experiments, mean values +/- SEM, *: p=0.0262, unpaired two-tailed t-test). **i,** Measurement of residual tumor volume detected in secondary mouse recipients at experimental endpoint from VXN (n=3 tumors) and

			control (n=12 tumors) groups. CT26 – BALB/c secondary tumor sizes are presented in mm^3 (Data from 2 independent experiments, mean values +/- SEM, **: p=0.0067, unpaired two-tailed t-test). Representative imaging of normal intestine tissue architecture and homeostasis where **j,** crypt proliferative cells are immunostained with anti-Ki-67, and **k,** E-cadherin and alpha-smooth muscle actin respectively mark the epithelial sheath and myofibroblasts in VXN (25 mg/kg) and vehicle treated animals (C57BL/6, 10 days, scale bar in **j**: 50μm. Scale bar in **k**: 100 μm). Average proliferative cell counts and villus length for both experimental groups are presented in bar graphs (Number of biological units (n: crypts and villi) from 3 independent mice per condition is indicated on graphs, mean values +/- SEM). See also Fig. 7, and Supplementary Table 10.
Extended Data Fig. 10	Suppression of cancer stem cell activity by vanoxerine enhances CRC antitumor immune response *in vivo*	Bergin_ED_Fig10.jpg	**a,** Differential expression of transposable elements (TEs) in HCT116 cells treated with VXN (10 μM, 48 h) vs. DMSO controls (n=3 biological replicates from 2 independent RNA-seq experiments, p<0.05). **b,** Distribution of significantly and commonly upregulated TEs in VXN (10 μM) and BIX-01294 (1 μM) treated t-hESCs (vs. vehicle) across different TE classes (n= 2 independent tumor pairs from 1 independent RNA-seq experiment). **c,** Gene ontology analysis performed on differentially expressed genes from VXN *in vivo*-treated CRC tumors (vs. vehicle) showing significant enrichment of GO categories linked to T cells and anticancer immune response (RNA-seq data from **b**, exact p-values from hypergeometric test available in Source Data). **d,** GSEA enrichment plots showing a positive correlation between genes within the COATES_MACROPHAGE_M1_VS_M2_UP and

			FOSTER_TOLERANT _MACROPHAGES _UP signatures and genes upregulated by VXN treatments in CRC tumors *in vivo* (RNA-seq data from **b**, NES and NOM p-value were calculated by the GSEA Software version 4.0.3). **e, f,** Heat map representing the expression of individual genes from the GOTZMANN_EPITHELIAL_TO_ MESENCHYMAL_TRANSITION_UP _DOWN genesets in vehicle and VXN-treated (25 mg/kg, 10 days) CRC tumors (RNA-seq data from **b**, color scale: Log2 normalized counts). **g,** Representative pictures of hematoxylin and eosin staining showing lymphocyte infiltration in VXN-treated CRC tumors vs. vehicle controls. Tissue sections were analyzed by a certified pathologist, and arrowheads indicate the presence of lymphocytes (n=3 independent tumor pairs, 2 independent experiments, scale bar: 50 μm). **h,** Representative fluorescence micrograph of anti-CD8a immunostaining in vehicle and VXN-treated (25 mg/kg, 10 days) CRC tumor sections. Nuclei were stained using DAPI (n=3 independent tumor pairs, 2 independent experiments, scale bar: 50 μm). **i,** Representative HCI-acquired images of vehicle and VXN *in vivo*-treated mouse primary tumors co-stained for T cell CD8a and macrophage Iba-1 markers. Nuclei were counterstained using DAPI (Scale bar: 1 mm). CD8a and Iba-1-positive cell counts are presented in the bar graph (n=3 independent tumor pairs, 2 independent experiments, mean values +/- SEM, *: p=0.0117, ***: p=0.0007, unpaired multiple t-tests). **j,** qPCR analysis of T cell markers in bulk CT26-BALB/c tumors excised from vehicle and VXN-treated mouse primary recipients (n=5

			independent tumor pairs (except Il12b: n=4, and cd74: n=3), dots on bar graphs represent independent PCR experiments: bars are mean values +/- SEM, p-values are indicated on graphs, unpaired two-tailed t-test). **k,** qPCR analysis of T cell markers in bulk CT26 – BALB/c tumors excised from control IgG and anti-PD-L-injected mouse primary recipients (n=3 independent tumor pairs from 3 independent experiments, mean values +/- SEM, p-values indicated on graphs, unpaired two-tailed t-test). See also Fig. 8, and Supplementary Tables 5, 10-11.

Item	Present?	Filename Whole original file name including extension. i.e.: Smith_SI.pdf. The extension must be .pdf	A brief, numerical description of file contents. i.e.: *Supplementary Figures 1-4, Supplementary Discussion, and Supplementary Tables 1-4.*
Supplementary Information	Yes	Bergin_SI.pdf	Supplementary Notes 1-3, Supplementary Table 1, and Supplementary Figures 1-2
Reporting Summary	Yes	Bergin_Reporting_Summary.pdf	
Peer Review Information	No	*OFFICE USE ONLY*	

Type	Number Each type of file (Table, Video, etc.) should be numbered from 1 onwards. Multiple files of the same type should be listed in sequence, i.e.: Supplementary Video 1, Supplementary Video 2, etc.	Filename Whole original file name including extension. i.e.: *Smith_ Supplementary_Video_1.mov*	Legend or Descriptive Caption Describe the contents of the file
Supplementary Table	1	Bergin_Suppl_Tables_2_to_13.xlsx	Supplementary Tables 2 to 13

17
18

Parent Figure or Table	Filename Whole original file name including extension. i.e.: *Smith_SourceData_Fig1.xls*, or *Smith_ Unmodified_Gels_Fig1.pdf*	Data description i.e.: Unprocessed western Blots and/or gels, Statistical Source Data, etc.
Source Data Fig. 1	Source Data Figure 1 - Uncropped images.jpg	Uncropped blot Images for Figure 1
Source Data Fig. 1	Bergin_SourceData_Fig1.xlsx	Numerical Source Data for Figure 1
Source Data Fig. 2	Source Data Figure 2 - Uncropped images.jpg	Uncropped blot Images for Figure 2
Source Data Fig. 2	Bergin_SourceData_Fig2.xlsx	Numerical Source Data for Figure 2
Source Data Fig. 3	Source Data Figure 3 - Uncropped images.jpg	Uncropped blot Images for Figure 3
Source Data Fig. 4	Source Data Figure 4 - Uncropped images.jpg	Uncropped blot Images for Figure 4
Source Data Fig. 4	Bergin_SourceData_Fig4.xlsx	Numerical Source Data for Figure 4
Source Data Fig. 5	Bergin_SourceData_Fig5.xlsx	Numerical Source Data for Figure 5
Source Data Fig. 6	Bergin_SourceData_Fig6.xlsx	Numerical Source Data for Figure 6
Source Data Fig. 7	Bergin_SourceData_Fig7.xlsx	Numerical Source Data for Figure 7
Source Data Fig. 8	Bergin_SourceData_Fig8.xlsx	Numerical Source Data for Figure 8
Source Data Extended Data Fig./Table 1	Bergin_SourceData_ED_Fig1.xlsx	Numerical Source Data for Extended Data Figure 1
Source Data Extended Data Fig./Table 2	Bergin_SourceData_ED_Fig2.xlsx	Numerical Source Data for Extended Data Figure 2
Source Data Extended Data Fig./Table 3	Source Data Extended Data Figure 3 - Uncropped images.jpg	Uncropped blot Images for Extended Data Figure 3
Source Data Extended Data Fig./Table 3	Bergin_SourceData_ED_Fig3.xlsx	Numerical Source Data for Extended Data Figure 3
Source Data Extended Data Fig./Table 4	Source Data Extended Data Figure 4 - Uncropped images.jpg	Uncropped blot Images for Extended Data Figure 4

Source Data Extended Data Fig./Table 4	Bergin_SourceData_ED_Fig4.xlsx	Numerical Source Data for Extended Data Figure 4
Source Data Extended Data Fig./Table 5	Bergin_SourceData_ED_Fig5.xlsx	Numerical Source Data for Extended Data Figure 5
Source Data Extended Data Fig./Table 6	Source Data Extended Data Figure 6 - Uncropped images.jpg	Uncropped blot Images for Extended Data Figure 6
Source Data Extended Data Fig./Table 6	Bergin_SourceData_ED_Fig6.xlsx	Numerical Source Data for Extended Data Figure 6
Source Data Extended Data Fig./Table 7	Source Data Extended Data Figure 7 - Uncropped images.jpg	Uncropped blot Images for Extended Data Figure 7
Source Data Extended Data Fig./Table 7	Bergin_SourceData_ED_Fig7.xlsx	Numerical Source Data for Extended Data Figure 7
Source Data Extended Data Fig./Table 8	Source Data Extended Data Figure 8 - Uncropped images.jpg	Uncropped blot Images for Extended Data Figure 8
Source Data Extended Data Fig./Table 8	Bergin_SourceData_ED_Fig8.xlsx	Numerical Source Data for Extended Data Figure 8
Source Data Extended Data Fig./Table 9	Source Data Extended Data Figure 9 - Uncropped images.jpg	Uncropped blot Images for Extended Data Figure 9
Source Data Extended Data Fig./Table 9	Bergin_SourceData_ED_Fig9.xlsx	Numerical Source Data for Extended Data Figure 9
Source Data Extended Data Fig./Table 10	Bergin_SourceData_ED_Fig10.xlsx	Numerical Source Data for Extended Data Figure 10

The dopamine transporter antagonist vanoxerine inhibits G9a and suppresses cancer stem cell functions in colon tumors

Christopher J. Bergin[1], Aïcha Zouggar[1], Amanda Mendes da Silva[1], Tanguy Fenouil[1,2,3], Joshua R. Haebe[1], Angelique N. Masibag[1], Gautam Agrawal[1], Muhammad S. Shah[1], Tamara Sandouka[1], Mario Tiberi[1,4,5], Rebecca C. Auer[6,7,8,9], Michele Ardolino[6,8,9], and Yannick D. Benoit[1,10,*].

[1] Department of Cellular and Molecular Medicine, Faculty of Medicine, University of Ottawa, ON, Canada.
[2] Inserm U1052, CNRS UMR5286, Centre de Recherche en Cancérologie de Lyon, Université Claude Bernard Lyon 1, Lyon, France
[3] Institut de Pathologie Multisite des Hospices Civils de Lyon, Site Est, Groupement Hospitalier Est, Bron, France
[4] University of Ottawa Brain and Mind Research Institute, Ottawa, Ontario K1H 8M5, ON, Canada.
[5] Neuroscience Program, Ottawa Hospital Research Institute, Ottawa, ON, Canada
[6] Department of Biochemistry, Microbiology and Immunology, Faculty of Medicine, University of Ottawa, ON, Canada.
[7] Department of Surgery, Faculty of Medicine, University of Ottawa, ON, Canada.
[8] Center for Cancer Therapeutics, Ottawa Hospital Research Institute, Ottawa, ON, Canada
[9] Centre for Infection, Inflammation and Immunity, University of Ottawa, ON, Canada
[10] School of Pharmaceutical Sciences, Faculty of Medicine, University of Ottawa, ON, Canada

* To whom correspondence should be addressed:
Dr. Yannick D. Benoit Ph.D., Department of Cellular and Molecular Medicine, Faculty of Medicine, University of Ottawa, 451 Smyth Road, RGN 2231
Ottawa, Ontario, K1H 8M5, Canada, Phone: 613-562-5800 Extension: 7508
Email: ybenoit@uottawa.ca

Key Words: Colorectal cancer, colon cancer, Cancer Stem Cell, Epigenetic, Phenotypic screening, Dopamine transporter, Vanoxerine, GBR-12909.

ABSTRACT

Cancer stem cells (CSC), functionally characterized by self-renewal and tumor-initiating activity, contribute to decreased tumor immunogenicity while fostering tumor growth and metastasis. Targeting the histone methyltransferase (HMTase) G9a effectively blocks CSC functions in colorectal tumors by altering pluripotent-like molecular networks. However, existing molecules directly targeting G9a HMTase activity failed to reach clinical stages due to safety concerns. Using a stem cell-based phenotypic drug screening pipeline, we identified the dopamine transporter (DAT) antagonist vanoxerine, a compound with previously demonstrated clinical safety, as a cancer-specific downregulator of G9a expression. Here we show that gene silencing and chemical antagonism of DAT impede colorectal CSC functions by repressing G9a expression. Antagonizing DAT also enhanced tumor lymphocytic infiltration by activating endogenous transposable elements and type-I interferon response. Our study unveils the direct implication of the DAT-G9a axis in the maintenance of CSC populations and an approach to improve anti-tumor immune response in colon tumors.

MAIN TEXT

Immunotherapy substantially improved the therapeutic landscape of several cancers[1]. In colorectal cancer (CRC), the clinical benefits from immune checkpoint inhibitors were mainly observed in patients presenting high microsatellite instability and mismatch repair deficiency, representing only 15-20% of clinical cases[2-4]. Thus, chemotherapy remains the mainstay to treat advanced-stage and metastatic CRCs, using drugs with a known bias of enhancing cancer stem cell (CSC) functions within the intratumor heterogeneity[5,6]. Studies focused on tumor heterogeneity and cellular hierarchies support the existence of CSCs, which harbor self-renewal and tumor initiation capacity[7]. Akin to several human cancers, colon tumors are organized according to a cellular hierarchy governed by a population of highly tumorigenic CSCs[8]. Investigations on this rare subset of cells have highlighted the importance of understanding CSC biology to develop next-generation chemotherapeutic strategies.

A relationship was established between cancer stemness and tumor immunogenicity, where CSCs would promote immune evasion by repelling cytotoxic T cells[9,10]. Thus, identifying tools suppressing CSCs in CRC may promote lymphocytic infiltration in the tumor microenvironment or bolster response to immune checkpoint inhibitors.

Multiomics campaigns revealed shared molecular networks between human pluripotent stem cells and tumors[11,12]. Advances in cancer epigenetics showed central requirement for chromatin regulation during the emergence of CSCs and tumor initiation[13-15]. Combining pluripotency and CSC epigenetic determinants as readouts, we screened a collection of clinically safe drugs to identify colon CSC-bioactive compounds. We identified vanoxerine (VXN), a dopamine transporter (DAT) antagonist initially developed to treat cocaine addiction, as a candidate for context-specific inhibition of colon CSC activity. Specifically, VXN downregulates the HMTase G9a, which consequently blocks CSC functions and increases immune cell infiltration in CRC tumors. Moreover, DAT knockdown recapitulates VXN effects in CRC cells, suggesting an implication of the DAT-G9a axis in the maintenance of CSCs.

Vanoxerine alters the deposition of H3K9me2 in cancer cells

The histone methyltransferase G9a and its associated histone mark H3K9me2 are crucial to maintain CSC functions and pluripotent-like networks in colon cancer[13]. To identify clinically-safe drugs targeting molecular hallmarks of CSCs, we executed a cell-based chemical screening assay measuring the effect of a library of FDA-approved or late-stage development compounds on pluripotency and H3K9me2 deposition in a transformed variant of human embryonic stem cells (t-hESCs) (Fig. 1a)[16-19]. Fluctuations in Oct4 protein (pluripotency marker) and H3K9me2 deposition (CSC epigenetics) were quantified by high-content imaging (Fig. 1a, Extended Data Fig. 1a-d, Supplementary Tables 1-2, Supplementary Note 1). We identified the DAT antagonist vanoxerine (VXN), the estrogen receptor modulator clomiphene, and the antiparasitic agent niclosamide as drugs simultaneously reducing Oct4 and H3K9me2 levels in t-hESCs (Fig. 1b-c, Extended Data Fig. 1a-c). All three candidates also caused concomitant decreases in H3K9me2/3 and 5-cytosine DNA methylation (5-meC) levels in t-hESCs, akin to G9a inhibition using BIX-01294 (Extended Data Fig. 1d). Next, each candidate was tested for growth inhibition on human colon cancer lines (HT29, HCT116, SW480) and normal human intestinal crypt

cells (HIEC) (Fig. 1d, Extended Data Fig. 1e-f). VXN showed superior cancer-selective toxicity ($EC50_{cancer}$ <<< $EC50_{normal}$) compared to clomiphene and niclosamide, and similar to the effect of the CSC-selective drug CWP232228 (Fig. 1d-e, Extended Data Fig. 1e-f, Supplementary Table 3)[19]. Furthermore, VXN showed anticancer bioactivity across different models of tumors (*e.g.*, melanoma) where increased H3K9me2 deposition drives tumorigenesis (Extended Data Fig. 1g)[20]. Functional experiments showed that dose-dependent reduction in H3K9me2 levels and decreased cell proliferation caused by VXN were associated to increased apoptosis in HT29 cells, but not in normal intestinal cells (Fig. 1f-h).

Transcriptome profiling of the VXN response in HT29 and HIEC cells revealed a subset of 3175 genes differentially expressed in CRC cells but unaffected in their normal counterparts. Gene signature enrichment analysis (GSEA) performed on the cancer-selective response to VXN suggests a downregulation of genes overexpressed in CRC lesions (Fig. 2a, Extended Data Fig. 2a-b, Supplementary Tables 4-5). Accordingly, VXN selectively increased intestinal differentiation genes, repressed crypt markers, and downregulated Wnt/β-catenin target genes in HT29 cells (Fig. 2a, Extended Data Figure 2c-d)[21,22]. The upregulation of Bmi1-repressed genes by VXN is consistent with the role of this factor maintaining self-renewal in colorectal CSCs[22]. VXN also downregulated genes commonly used to enrich colon CSC populations, such as *LGR5* and *PROM1* (Extended Data Fig. 2e)[8,21]. Using a one-class logistic regression machine-learning approach, we calculated the transcriptional stem cell index (mRNAsi) for our experimental models versus a cohort of 375 colon adenocarcinoma samples (TCGA COAD). VXN-treated HT29 cells exhibited a lower mRNAsi than DMSO controls, supporting that VXN disrupts stemness networks in CRC cells (Extended Data Fig. 2f)[12,13]. Interestingly, genesets related to type-I interferon and viral defense responses were enriched in the cancer-selective VXN transcriptional signature (Fig. 2a, Extended Data Fig. 2g). This aligns with previous reports of epigenetic therapies promoting immune susceptibility of tumor cells[23,24].

Next, we performed a correlation analysis of cancer cell sensitivity to VXN versus other drugs through the DepMap PRISM drug repurposing initiative[25]. We identified the HDAC inhibitor and H3K9 modulator romidepsin[26,27] yielding a growth inhibitory response correlated to VXN in a panel of 34 human CRC lines (Fig. 2b, Extended Data Fig. 3a-b, Supplementary Table 6, Supplementary Note 2). While VXN analog GBR-12935 displayed cancer-selective toxicity in human intestinal models, the response to benztropine, a cancer-

bioactive DAT antagonist sharing structural similarities with VXN, did not correlate with VXN sensitivity in CRC and lung cancer lines (Extended Data Fig. 3d)[28,29]. The distinct DAT-binding mode of VXN versus other DAT antagonists could explain such a discrepancy with benztropine[30].

Our previous work showed that G9a inhibition alters pluripotent-like and CSC functions in CRC tissues[13]. Transcriptome profiling data suggest that *EHMT2* (G9a) is the only H3K9me/5-meC-associated regulator, including *EHMT1* (GLP), showing a downregulation in HT29 cells, but not in normal HIEC cells following VXN treatments (Extended Data Fig. 3e-f). Western blot analysis confirmed reduced G9a protein levels in VXN-treated HT29 cells and t-hESCs (Fig. 2c). G9a was either undetectable or observed as trace amounts in normal HIEC cells, supporting its potential implication in the cancer-specific response to VXN (Extended Data Fig. 3g). VXN also repressed *EHMT2* and stemness-associated signatures in t-hESCs (Extended Data Fig. 3h-j).

To understand the impact of VXN on G9a target loci in CRC, we applied a multi-omic integrative approach to functionally classify G9a and H3K9me2 co-enriched genes in human primary colon CSC-enriched populations (ChIP-seq) and showing a cancer-selective upregulation upon treatments (RNA-seq) (Fig. 2d, Supplementary Table 4). G9a targets in colon CSCs and specifically upregulated by VXN in HT29 cells showed enrichment in cell differentiation-associated signatures (Fig. 2e, Supplementary Table 4). These targets were also enriched in differentiation-inducing transcription factor consensus binding motifs (Extended Data Fig. 3k, Supplementary Table 4)[31]. Altogether, these observations constitute a basis to further investigate the mechanism of VXN in CRC.

Antagonizing DAT blocks G9a transactivation in colon cancer

VXN was characterized as a DAT ligand, blocking dopamine reuptake in the nucleus accumbens[32,33]. In silico analysis supported DAT as a selective target for VXN, binding the same motif than cocaine, but with a >35-fold higher affinity (Extended Data Fig. 4a, Supplementary Table 7). Aside from a potential role as a CRC diagnosis biomarker, DAT-encoding gene (*SLC6A3*) is not extensively documented in the mammalian digestive tract[34]. Western blot revealed DAT protein in human HT29, HCT116, and mouse MC38 CRC lines, while only trace amounts were detected in normal HIEC cells (Fig. 3a). DAT protein and mRNA levels were 4- and 15-fold higher,

146 respectively, in CSC-enriched, patient-derived CRC spheroids compared to heterogeneous organoids (Fig. 3a, Extended Data Fig. 4b).
147 Immunostaining experiments showed scattered patterns of DAT-marked dots in most cells within patient-derived spheroids and HCT116
148 cells, while only a few cells showed positive staining in heterogeneous CRC organoids (Fig. 3b-c). Human colon adenocarcinoma
149 sections also showed punctated intracellular distribution of DAT in rare epithelioid cells (Fig. 3b). DAT-positive specks did not
150 colocalize with the early endosome marker Rab5a or the late endosome/lysosome marker LAMP1 (Fig. 3c). This suggests that DAT
151 trafficking may favor specialized endomembranous compartments in CRC, as observed in other pathological contexts[35]. In silico
152 membrane permeability modeling supports VXN's passive transport across the plasma membrane, which does not appear as an obstacle
153 to reach DAT-containing structures in CRC cells (Supplementary Fig. 1)[36].

154 Single-cell transcriptomics (scRNA-seq) from 23 primary CRC samples showed negligible amounts of tumor epithelioid cells
155 presenting detectable levels of *SLC6A3* across tumor heterogeneity (1 for 16,000) (Extended Data Fig. 4c, Supplementary Note 3). DAT
156 protein and transcript (*SLC6A3*) were undetectable in normal colonic epithelial structures (Extended Data Fig. 4c-d). Documented
157 inconsistencies between *SLC6A3* mRNA and DAT protein levels in other systems motivated the characterization of DAT distribution
158 in CRC using single-cell protein analyses[37,38]. We detected DAT protein at an average frequency of 4.75% in bulk colorectal
159 adenocarcinoma cells, while sorting CD133-positive subfractions from bulk tumors increased this proportion to 43.5% (Fig. 3d,
160 Extended Data Fig. 4e-g, Supplementary Table 8). By multiplexing DAT and CD133 detection, we observed that only 35% of DAT-
161 positive cells are found within the CD133-positive population (Fig. 3d, Extended Data Fig. 4f). In CRC patient-derived spheroids, 72.8%
162 of the cells were DAT-positive, while the frequency of CD133 cells was only 30.75% (Fig. 3d). At the functional level, the average
163 frequency of cells showing tumor-initiating capacities in CRC patient-derived spheroids was established at 82.5%, suggesting DAT
164 could also be present in early tumor progenitor cells in addition to CD133-positive CSCs (Supplementary Table 8). We observed that
165 phospho-H3S10, which is restricted by H3K9me2 deposition in pluripotent-like cells, was only detected in 1.5% and 4.2% of the cells
166 in CD133-sorted CRC adenocarcinomas and patient-derived spheroids, respectively (Fig. 3e)[39]. Moreover, >94% of DAT-positive cells
167 were negative for phospho-H3S10, indirectly supporting an association between DAT-expressing cells and high H3K9me2 deposition

in CRC (Fig. 3e). Importantly, we confirmed that DAT-positive cells in CRC tumors do not correspond to enteroendocrine cells (chromogranin A) or tumor-associated neurons (Neurofilament) (Fig. 3f, g). Interestingly, VXN treatments decreased the number of DAT-positive cells in HT29 populations (Fig. 3h), supporting a direct impact on target-expressing cells.

To evaluate the potential link between DAT and CSC functions in CRC, we used an inducible shRNA system to knockdown *SLC6A3* in HCT116 cells (Extended Data Fig. 4h-i). *SLC6A3* knockdown decreased G9a protein and mRNA levels, while VXN treatments had no additive effect on such a downregulation nor on the growth rate of CRC cells (Fig. 4a-b, Extended Data Fig. 4j). *SLC6A3* knockdown also reduced the expression of the intestinal crypt progenitor markers *SOX9*, *BMI1*, *FOXM1*, and *MYBL2*, supporting the alteration of stem-like functions (Fig. 2g). Accordingly, *SLC6A3* knockdown impaired clonogenic tumor-initiating capacities compared to controls in CRC organoid and spheroid formation assays (Fig. 4d, Extended Data Fig. 4k). Transient knockdown of *SLC6A3* using siRNA also reduced tumor-initiating functions in HCT116 cells (Extended Data Fig. 4l). We performed a comprehensive GSEA analysis to compare transcriptional changes caused by *SLC6A3* knockdown versus the response to VXN in HCT116, HT29, and t-hESC cells. This revealed a consistent downregulation of pluripotency-associated and CRC gene signatures across all tested conditions (Fig. 4e, Supplementary Table 5). Similar gene enrichment profiles were observed for these signatures in t-hESCs treated with the G9a inhibitor BIX-01294 (Fig. 4e).

Acute cocaine administration was shown to decrease G9a expression in the nucleus accumbens, inducing profound changes in dopaminergic neuron epigenetic wiring[40]. Moreover, *G9a in vivo* knockdown reduced cocaine self-administration, which represents an interesting link with the initial purpose of VXN as an agent treating cocaine addictions[33,41]. While competition assays supported the implication of DAT in the VXN mechanism of action in CRC, dopamine remained undetected in basal and conditioned experimental media, as well as in lysates from all of our models (Extended Data Fig. 5a-b). This suggests dopamine might not be essential to DAT functions in CRC pathophysiology. Among other putative VXN targets, the sigma receptor-2 (*TMEM97*) appeared enriched in HT29 cells vs. normal HIECs (Extended Data Fig. 5c). Nevertheless, the use of sigma receptor blockers DTG and SM-21 failed to mimic the cancer-selective effects of VXN on human intestinal cell growth (Extended Data Fig. 5d). As documented in acute myeloid leukemia,

the dopamine receptor-encoding gene *DRD2* appeared upregulated in CRC cells vs. normal cells (Extended Data Fig. 5c)[17]. While the dopamine receptor antagonist haloperidol substantially decreased HT29 viability, most phenothiazines acting through dopamine D2 receptor blockade (*i.e.*, thioridazine, prochlorperazine, and fluphenazine) failed to modulate H3K9me2 levels in t-hESCs (Extended Data Fig. 1d and 5e).

The impact of DAT blockade on downstream signaling cascades in CRC cells is yet unknown. GSEA analysis from *SLC6A3* knockdown and VXN-treated CRC cell transcriptomes suggested a downregulation of the PI3K/AKT/mTOR pathway, which was not observed in VXN-treated HIEC cells (Extended Data Fig. 6a,-b). A profiling of the phosphorylation state of 46 human kinases in HT29 cells following VXN treatments (0, 6, 12, and 24 hours) identified members of the AKT/mTOR pathway showing reduced phosphorylation/activation levels (Fig. 4f, Extended Data Fig. 6c). Accordingly, *SLC6A3* knockdown decreased AKT phosphorylation on threonine-308 and serine-473 (Fig. 4g, Extended Data Fig. 6d). A STRING map analysis involving VXN-modulated kinases and the DAT interactome (BioGrid database) supported a functional association between DAT and the AKT pathway in cancer (Extended Data Fig. 6e, Supplementary Table 9). Consistently, single-cell protein analysis showed that 24 hours VXN treatment downregulates AKT phosphorylation only in DAT-positive HT29 cells (Fig. 4h). While VXN transcriptional response initially suggested an upregulation of adherens junction assembly and the downregulation of the canonical Wnt pathway (Fig. 4e), analyses measuring E-cadherin/β-catenin positive junctions and active-β-catenin levels failed to demonstrate a consistent relationship with *SLC6A3* knockdown in HT29 cells (Extended Data Fig. 6f-g). Thus, AKT downstream events represent the main exploration avenues to understand the impact of VXN on the CRC epigenome.

AKT signaling and G9a expression are linked in cancer via the orphan nuclear receptor Nur77, known to transactivate *EHMT2* in alveolar rhabdomyosarcoma cells[42]. Moreover, AKT-mediated phosphorylation of Nur77 (S351) is essential for its nuclear accumulation[43]. Both, VXN and AKT inhibition (AZD5363) blocked the nuclear accumulation of S351-phosphorylated Nur77 in human CRC cells (Fig. 5a, Extended Data Fig. 7a). The agonist of Nur77, Cytosporone B (CytoB), rescued the effect of VXN and AZD5363 on the nuclear levels phospho-Nur77 (Fig. 3a) [44]. Akin to *EHMT2*, Nur77 target genes *SLC2A2*, *IKBKE*, and *FBP2* were repressed by

VXN treatments, but CytoB rescued such an effect in HCT116 cells (Fig. 5b, Extended Data Fig. 7b)[45]. Similar results were observed functionally, where CytoB rescued tumor-initiating capacities in VXN-treated cells (Fig. 5c). However, CytoB failed to rescue the effect of VXN on general cell growth, as represented by unchanged organoid sizes (Fig. 5c). Altogether, these data support the involvement of Nur77 in the VXN-dependent silencing of G9a in CRC.

To determine whether Nur77 directly regulates G9a promoter in CRC, we performed chromatin immunoprecipitation (ChIP) assays and observed decreased p-Nur77 levels at *EHMT2* proximal promoter upon 24 hours of VXN treatment (Fig. 5d). This supports reduced mRNA and protein levels observed in VXN-treated t-hESCs and CRC cells. Using the ChIP Atlas database, we highlighted additional transcription factors regulating the *EHMT2* promoter, and observed induced C/EBPβ and ZNF143 recruitment in response to VXN (Fig. 5d, Extended Data Fig. 7c-d). Notably, C/EBPβ binding was previously reported at highly methylated loci in human ES cells[46]. Reduced representation bisulfite sequencing (RRBS) data showed enhanced CpG methylation around the *EHMT2* transcription start site in normal primary tissues (breast, liver, prostate, bronchus) and human pluripotent cells (H1), but not in tumorigenic models, including HCT116 and NT2/D1 (pluripotent) cells (Extended Data Fig. 7e). Thus, we performed MBD2-based DNA pulldowns quantifying changes in DNA methylation status at the *EHMT2* promoter, and observed a 3-fold increase in DNA methylation following VXN treatments compared to vehicle controls (Fig. 5d). This suggests that VXN causes long-term epigenetic silencing of G9a in DAT-expressing cells, which is potentially maintained across the CRC tumor heterogeneity (Fig. 3e).

To validate the implication of the DAT-G9a axis in the modulation of CSC-related functions, constitutive expression of full-length *EHMT2* was combined to VXN treatments in HCT116 cells, where the drug failed to decrease G9a levels (Extended Data Fig. 7f). Consequently, ectopic maintenance of *EHMT2* rescued HCT116 clonogenic capacities from VXN treatments (Fig. 5f), further supporting the implication of the DAT-G9a axis in mediating tumor-initiating functions. We also observed that forcing *EHMT2* expression alleviated VXN effects on *LGR5* silencing (CSC marker) and *DPP4* induction (differentiation marker) (Fig. 5g). Moreover, VXN failed to induce interferon type-I response genes *IFIT1*, *OAS3*, and *MX1* in ectopic *EHMT2*-expressing cells (Fig. 5h), strengthening the implication of G9a in VXN-dependent effects on stemness vs. differentiation states and tumor immune susceptibility.

VXN-mediated inhibition of G9a suppresses colon CSC activity

Considering the role of G9a in maintaining cancer stemness, we sought to determine whether VXN alters self-renewal and tumor-initiating functions in patient-derived CRC organoids and *in vivo* tumors. We used a serial organoid assay to measure the effect of VXN on CSC functions within primary CRC patient samples (Fig. 6a)[47]. Similar to 2D cultures, VXN reduced G9a levels and H3K9me2 deposition in CRC patient-derived spheroids (Extended Data Fig. 8a). Treating primary organoids from 5 independent CRC patients with escalating doses of VXN reduced organoid counts and average sizes (Fig. 6b, Extended Data Fig. 8b-c, Supplementary Table 8). Importantly, VXN blocked the capacity of dissociated primary organoids to initiate secondary organoid formation at doses as low as 0.25 μM, supporting the alteration of tumor-initiating functions within CRC samples (Fig. 6b, Extended Data Fig. 8d-e, Supplementary Table 8). In this context, the first-line CRC drug 5-fluorouracil (5-FU) failed to reduce secondary tumor organoid formation rates (Fig. 6b). Importantly, VXN had no effects on primary and secondary organoid formation from healthy colonic crypts at 0.25 or 0.5 μM doses, strengthening the concept of cancer-selective toxicity exerted by our candidate (Extended Data Fig. 8f-g).

Whereas a trend toward less proliferation (Ki-67) was observed, VXN significantly reduced Bmi1-positive cells inside primary CRC organoids, representing a hallmark of decreased self-renewal (Fig. 6c-d)[22]. This aligns with reduced *BMI1* expression observed in *SLC6A3* knockdown CRC cells (Fig. 4c). Next, patient-derived spheroids were sorted based on CD133 surface expression ($CD133^{High}$ and $CD133^{Low}$ fractions) and treated with VXN or vehicle control. Self-renewal activity was measured in each condition via a clonogenic spheroid formation assay (Fig. 6e). $CD133^{High}$ fractions presented 3-fold and 6-fold enrichments of *CD133* and *LGR5* expression, respectively, compared to $CD133^{Low}$ subpopulations, while DAT and G9a-encoding mRNAs were found in equal proportions in both fractions (Extended Data Fig. 8h). $CD133^{Low}$ CRC cells generated smaller spheroids and at a lower frequency (67.36%) than $CD133^{High}$ cells (96.2%) (Fig. 6f, Extended Data Fig. 8i). Moreover, VXN decreased self-renewal in the $CD133^{High}$ fraction at 0.25 and 0.5 μM (vs. DMSO), while no effects were observed in the $CD133^{Low}$ fraction (Fig. 6f). This finding confirms that VXN prominently alters the CSC compartment within CRC tumor hierarchy.

Next, we evaluated the effect of VXN on self-renewal *in situ*, using an *LGR5-GFP* knock-in reporter system in patient-derived CRC organoid formation assays (Fig. 6g, Extended Data Fig. 8j)[48]. Primary *LGR5-GFP* organoids were treated with VXN or vehicle control for seven days, and the presence of *LGR5*-expressing cells was monitored for 14 days post-treatment (Extended Data Fig. 8k). VXN treatments yielded a sustained decrease of LGR5-positive organoids (Extended Data Fig. 8l). Quantification of the GFP signal per individual organoids revealed that VXN also steadily decreased the frequency of LGR5-expressing cells (Fig. 6i), support that drug-mediated inhibition of G9a is blocking the re-emergence of LGR5-positive CSCs via cell plasticity. Still, residual secondary organoids formed upon re-plating of VXN-treated primary organoids showed no differences in *LGR5-GFP* intensity vs. controls, suggesting that such lingering tumor-initiating activity results from tolerant/unaffected CSCs (Extended Data Fig. 8m).

The translational applicability of VXN as a CSC-targeting agent *in vivo* was evaluated by syngeneic CRC tumor transplantation experiments (Fig. 7a). Daily injections of VXN (10 days, 25 mg/kg) reduced tumor growth in C57BL/6 and BALB/c mice engrafted with MC38 and CT26 CRC lines, respectively (Fig. 7b). VXN dosage was established from available *in vivo* safety and ADME data[49]. Both MC38 and CT26 parental cultures showed impaired growth rates upon VXN treatments, and higher expression of *SLC6A3* compared to heterogeneous *in vivo* tumors (Extended Data Fig. 9a-b). Transcriptome profiling of *in vivo*-treated tumors showed that VXN reduced *Ehmt2* expression and downshifted their mRNA stem cell index, indicating alterations in pluripotent-like molecular networks vs. vehicle controls (Fig. 7c, Extended Data Fig. 9c, Supplementary Table 10). This was accompanied by decreased levels of G9a protein, stemness-associated surface markers Sca-1 and CD44, and a drastic increase (>12-fold) in *Ehmt2* promoter methylation (Fig. 7c, Extended Data Fig. 9d-e). Accordingly, we observed a global decrease in H3K9me2-marked cells in whole tumor cross-sections and protein lysates from VXN-treated animals (vs. vehicle controls) (Fig. 7d, Extended Data Fig. 9f-h). Such a broader H3K9me2 reduction across bulk, heterogeneous tumors supports the long-lasting silencing of *Ehmt2* in the higher ranks of CRC cellular hierarchy. Serial tumor transplantation experiments showed that *in vivo* VXN treatments blocked secondary tumor formation in both the MC38 and CT26 models, confirming the deleterious impact of DAT antagonization on colorectal CSC activity (Fig. 7e). Limiting dilution analysis showed that CSC suppression by VXN is highly effective even at high doses of tumor cell injection (Fig. 7f). Moreover, residual

secondary tumors from VXN-treated groups showed significantly lower volumes compared to controls (Extended Data Fig. 9i). Remarkably, neither crypt cell proliferation nor tissue architecture was altered in the normal intestinal mucosa of VXN-treated animals (Extended Data Fig. 9j-k), which is consistent with the limited impact of VXN in HIEC cells and healthy colonic organoids.

VXN restores the immune response in colorectal tumors

Neoplastic stemness connects antigenicity, cellular heterogeneity, and immune suppression within the tumor microenvironment. Tumors presenting high stemness signatures were correlated with lower immune cell infiltration, cell-intrinsic suppression of endogenous transposable elements (TEs), and the type-I interferon response[10,12,23]. Reduced H3K9 methylation and G9a activity were also associated to enhanced TEs expression and restored tumor immunogenicity[20,50]. Considering the effect of VXN on type-I interferon and viral defense response genes, we sought to determine whether *SLC6A3* knockdown or drug-dependent H3K9me2 downregulation can impact TE expression. Transcriptomics showed that VXN increased TEs expression in HT29, HCT116, and t-hESC cells, akin to the G9a inhibitor BIX-01294 (Fig. 8a, Extended Data Fig. 10a, Supplementary Table 11). The *SLC6A3* knockdown mimicked the effect of VXN and BIX-01294 on TE expression in HCT116 cells (Fig. 8a). TEs from different classes were upregulated by VXN in CRC tumors, where LINE1, SINE, and ERVL elements displayed common regulation patterns versus HT29 cells (Fig. 8b, Supplementary Table 11). In contrast, common TE induction in t-hESCs was only observed in ERV1 class for VXN and BIX-01294 treatments, supporting the concept of tissue-specific silencing/activation patterns of retroelements (Extended Data Fig. 10b)[51]. Consistently, blocking retroelement transcription using reverse transcriptase inhibitors (RTi: zidovudine, nevirapine) suppressed VXN-dependent induction of type-I interferon response markers in HT29 cells (Fig. 8c).

Syngeneic CRC tumor transplantation models hold the advantage of testing the effects of VXN within an immune-competent system. GSEA and gene ontology analysis of transcriptomics from VXN *in vivo*-treated MC38 tumors highlighted significant enrichment of T cells, macrophages, and immune cytotoxicity signatures versus controls, while stemness indicators like pluripotency, Bmi1-mediated repression, and EMT signatures were down regulated (Fig. 8d-e, Extended Data Fig. 10c-f).

G9a inhibition is linked to enhanced effectiveness of immune checkpoint inhibitors and tumor-infiltrating T cells[20,52]. Thus, we combined *in vivo* VXN treatments with PD-L1 blockade to determine whether drug-induced CSC exhaustion and immune checkpoint inhibition display synergistic effects on CRC tumor growth. Consistent with the literature, anti-PD-L1 injections significantly reduced the growth of MC38 tumors[53], while no effects were observed in the CT26 model (Fig. 8f). When combined with VXN, checkpoint inhibition displayed only minor additive effects in the MC38 model and no changes in CT26 (Fig. 8f). High-content imaging analysis showed a significant increase in CD8-positive cells in anti-PD-L1-treated MC38 tumors but not in CT26 tumors (Fig. 8g). However, VXN treatments systematically increased the number of CD8-positive T cells in tumors from both systems (Fig. 8g), suggesting the observed tumor shrinkage is linked to enhanced T cell infiltration. Certified histopathological analysis of CRC tumor sections supported the enhanced presence of tumor-infiltrating lymphocytes in VXN-treated animals compared to controls (Extended Data Fig. 10g). Fluorescence scanning of MC38 and CT26 tumor sections revealed abundant pockets of CD8a-positive cells in tumors from VXN-treated animals, independent of anti-PD-L1 injections (Fig. 8h, Extended Data Fig. 10h). Tumors treated with VXN also showed a higher number of cells positive for the macrophage marker Iba-1 vs. controls (Extended Data Fig. 10i). Expression analysis of different T cell markers confirmed that VXN was effective at inducing T cell infiltration in CT26 tumors, while PD-L1 blockade failed to restore immunogenicity (Extended Data Fig. 10j-k). These results suggest that CSC suppression exerted by VXN activates TE expression and restores an immune-hot tumor microenvironment in CRC.

Discussion

Epigenetic drugs have gained attention as a strategy to reactivate tumor suppressors and reinstate normal-like functions in cancer. To date, molecules such as BIX-01294, UNC0642, and CM-272 were developed to block G9a activity[54]. However, very few *in vivo* follow-ups and no clinical trials emerged from these compounds, likely due to poor ADME and safety issues[54]. Benefited by drug repurposing and previously-demonstrated clinical safety, we identified VXN as a safe and effective agent targeting neoplastic stemness *in viv*o. Our study challenges current paradigms of epigenetic drug discovery by proposing to target a context-specific pathway rather

that direct catalytic activity to achieve CSC epigenome reprogramming. Our target-agnostic approach uncovered the DAT-G9a axis as a targetable pathway to block H3K9me2 deposition in CRC, rewiring the CSC epigenome and suppressing neoplastic self-renewal. Furthermore, the effect of VXN on enhancing tumor immune cell infiltration could alleviate the unresponsiveness to immune checkpoint inhibitors observed in CRC patients[55].

The expression pattern of DAT in CRC tumors supports its value as a biomarker of intratumor heterogeneity, encompassing CSCs and progenitors holding the capacity to revert to self-renewing entities via cell plasticity. The prominent localization of DAT within the endomembranous system of CRC cells was surprising, although emerging knowledge suggests a contribution from organelle membrane constituents to key signaling events in CSCs[56]. Moreover, independent proteomic profiling studies detected the presence of DAT in exosomes[57,58]. Thus, we cannot exclude the possibility that VXN-DAT interactions could contribute to decreased cancer stemness and tumor immunogenicity by impacting CSC-specific extracellular vesicle secretion. Despite our pioneering characterization of DAT distribution across CRC tumor heterogeneity, and its regulatory effects on the AKT/Nur77/G9a cascade, additional work will be necessary to fully understand the implication of DAT in cancer stemness.

Moreover, our findings align with extensive characterization of the effect of cocaine on DAT-expressing neurons, causing long-term G9a silencing and associated behavioral alterations[40,41]. Considering the original clinical application of VXN as a treatment for cocaine addiction, it would be interesting to further study the impact of cocaine on CSC functions using animal and patient-derived *ex vivo* systems[33,59]. While available longitudinal cohort studies might represent a starting point to determine whether cocaine consumption could impact cancer epigenetics and tumor heterogeneity, polysubstance abuses and detrimental lifestyle observed in cocaine use disorder are likely to mask significant effects on CRC incidence and treatment outcomes[60].

METHODS

Ethics statement

Our research complies with all the relevant ethical regulations. All *in vivo* procedures and protocols were approved by the University of Ottawa Animal Care Committee (Protocol# CMMe-3916). The maximum tumor burden indicated by the ethics review board is 1.7cm^3 per tumor. However, past this tumor size, monitoring of clinical indicators of animal distress, including lethargy, unresponsiveness, >20% weight loss (vs. control), lack of self-care, hunching, piloerection, abnormal discharges, respiratory distress, dehydration, and hypothermia was used to determine endpoints. This monitoring approach beyond the tumor burden limit was performed by the University of Ottawa Animal Care and Veterinary Services and approved by the University of Ottawa Animal Care Committee (Protocol# CMMe-3916). Control secondary recipient mice (Balb/c, 12 out of 12 individuals) injected with CT26 tumor cells presented at least one tumor >1.7cm^3 (Extended Data Fig. 9i). No animal reaching clinical indicators of distress were used in this study. The use of human pluripotent stem cells, as reported in this study, was approved by the Ottawa Health Science Network Research Ethics Board (OHSN-REB, Protocol# 20170635-01H). Primary normal and colorectal tumor samples were obtained with patient informed consent, as approved by the Ottawa Health Science Network Research Ethics Board (OHSN-REB, Protocol# 20200159-01H) via the Global Tissue Consenting initiative (GTC, OHRI) (see Supplementary Table 8 for patient-specific information).

Cell culture and reagents

Transformed human embryonic stem cells (t-hESCs), HT29, HCT116, SW480, M17, 293FT, human normal intestinal epithelial crypt cells (HIEC), MC38, and CT26 cell lines were cultured at 37°C in 5% CO_2, as presented in Supplementary Table 12. All commercial cell lines were authenticated by providers and routinely tested for mycoplasma in the lab (see Reporting Summary). Human colon tumor-initiating cells were derived from primary tumor tissues and maintained as spheroids in ultralow adhesion flasks, in the CSC media formulation reported in Supplementary Table 12 [47]. Normal colonic organoid cultures were established from fragments of healthy colonic mucosa. Gentle Cell Dissociation Reagent (STEMCELL Technologies) was used to dissociate epithelial crypt structures. Crypt suspensions were embedded in 3D Matrigel domes and maintained in IntestiCult™ Human Organoid Growth Medium (STEMCELL Technologies). Complete protocol available at: https://www.stemcell.com/technical-resources/area-of-interest/organoid-research.html. Isolation of CD133^{High} and CD133^{Low} populations from primary CRC tissues was performed by MACS cell separation using the human CD133 MicroBead kit (Miltenyi Biotech) according to the manufacturer's recommendations[47].

Immunohistochemistry

Cells in culture wells were fixed with 2% formalin and incubated in Perm/Wash buffer (BD Biosciences) at 4°C for 15-30 min prior to primary antibody incubation (overnight, 4°C)[19]. Nuclei were stained with Hoechst 33342. Histological sections of formaldehyde-fixed paraffin-embedded human primary colon carcinoma and mouse tumors were rehydrated, quenched (0.1 M glycine buffer), and blocked (2.5% BSA-PBS) prior to immunostaining[31]. Information on primary and secondary antibodies used for immunostaining is available in Supplementary Table 12. Histological sections were mounted using Vectashield mounting medium with DAPI (Vector labs). Cells and tissue sections were imaged with an ImageXpress Pico High-Content imaging system (Molecular Devices). Images were acquired and analyzed using CellReporterXpress software (v2.8.2). For

immunofluorescence on organoids and spheroids, samples grown in Matrigel domes in Ibidi 35 mm u-Dishes were fixed with 4% PFA+ 0.1% Triton X-100. 3D organoids were washed with a solution of 0.1% Triton X-100, 0.002% SDS and 0.2% BSA in PBS, blocked and incubated with primary antibodies overnight at 4°C [61]. Hoechst 33342 was added to the secondary antibody solution in organoid wash buffer. Samples were optically cleared using FUnGI clearing solution for 30 minutes at room temperature prior to imaging[61]. Z-stack images were captured using a ZEISS LSM800 confocal microscope with a 25X immersion objective using ZEN pro software (v3.6). Image renderings were generated using Imaris 9.5 (Oxford Instruments) utilizing dot and surface rendering functions.

High-throughput phenotypic drug screening assay

t-hESC cells were seeded at $5x10^3$ cells per well in 96-well plates in mTeSR Plus media. Media was replaced with fresh mTeSR Plus in which test drugs were diluted to 5 μM (stocks at 10 mM in DMSO) 24 hr post-seeding. t-hESCs were treated for 48 hr prior to fixation and immunofluorescence staining. Over the first phenotypic screening filter (loss of pluripotency, Fig. 1a), the impact of each compound (Supplementary Table 1) on the frequency of Oct4-positive cells was evaluated by high-content imaging vs. vehicle control (DMSO 0.1%) and positive control (CWP232228 100 nM), as previously documented[17,18,62]. Drugs inducing loss of pluripotency were tested for H3K9me2 modulation in t-hESCs. Similarly, upon drug treatment and fixation, cells were immunostained for H3K9me2, and high-content imaging analysis was performed to quantify drug-induced variations in the H3K9me2 signal vs. vehicle control. BIX-01294 (1 μM) was used as positive controls for H3K9me2 reduction (G9a inhibitor)[13]. Nuclei were stained with Hoechst 33342 (1:1000), and nuclear counts were used as a readout for cell growth[17]. Loss of pluripotency hits were validated through a backscreen step, including non-hit compounds. See Supplementary Tables 1-2, Supplementary Note 1, and Source Data.

Cell count and drug dose-response cell growth analysis

Cells were plated at a density of $5x10^3$ cells/well in 96-well culture plates 24 h prior to drug treatments. Small molecule inhibitors (VXN, clomiphene, niclosamide, GBR-12935, haloperidol, DTG, SM-21) were used at concentrations ranging from 0.002 to 20 μM for 48 or 72 hours. Equivalent volumes of vehicle DMSO were used as controls (≤0.1%). Cells were formalin-fixed and stained with Hoechst 33342, and plates were imaged with an ImageXpress Pico High-Content imaging system (Molecular Devices). Images were analyzed using CellReporterXpress software (v2.8.2), and half maximum effective concentration (EC_{50}) values were calculated using GraphPad Prism (v10.1.0).

Western blot analysis

Whole-cell extracts were prepared in Laemmli Sample Buffer (60 mM Tris-HCl pH 6.8, 2% SDS, 10% glycerol, 5% β-mercaptoethanol, 0.01% bromophenol blue), sonicated and thermo-reduced/denatured (5 min, 95°C) prior to electrophoresis on 12% or 15% polyacrylamide gels. Proteins were transferred onto nitrocellulose membranes and immunodetected as documented[19]. For total methylated DNA detection, dot blot experiments were performed on whole-cell extracts by directly spotting sonicated lysates onto membranes, which were air-dried for 30 min prior to blocking[13]. The membranes were blocked in PBS containing 5% skim milk and 0.1% Tween 20. Primary and secondary antibodies used are described in Supplementary Table 12. A full-range molecular mass marker (Full-Range Rainbow Marker, VWR) was used as a standard. Blot images were acquired using a ChemiDoc MP Imaging system with the Image Lab acquisition and analysis software (v6.1). Quantitative optical densitometry analysis of bands was performed using ImageJ software (v1.53k).

EdU incorporation assays

The proliferation rate of HT29 cells was determined using a 5-ethynyl-2'-deoxyuridine (EdU) Staining Proliferation kit (iFluor 647) (Abcam)[18,62]. Briefly, 5,000 cells per well were plated in 96-well plates. At 24 hours post-seeding, cells were treated with VXN for 48 hours vs. DMSO control. Two hours before the end of the drug incubation period, a pulse of EdU was added to all cultures according to the manufacturer's protocol. Cells were formalin-fixed (2% v/v), and EdU-positive cells were fluorescently labeled following a click chemistry reaction. Nuclei were stained with Hoechst 33342. Image acquisition and EdU-positive cell scoring were performed using an ImageXpress Pico High-Content imaging system (Molecular Devices).

Apoptosis detection assay

Apoptosis levels were determined using CellEvent Caspase-3/7 green detection reagent (ThermoFisher)[18,62]. HT29 and HIEC cells were plated at 5,000 cells per well in 96-well plates and maintained for 24 hours in standard growth media. Cells were treated with DMSO or VXN for 48 hours. Each cell line was also treated with 1 μM staurosporine for 6 h (positive control). 5 μM CellEvent™ Caspase 3/7 Green labeling reagent was added to each well and incubated for 30 min at 37 °C. Cells were washed and formalin-fixed (2% v/v) for 30 min. Hoechst 33342 was used to stain nuclei. Image acquisition and activated Caspase-3/7-positive cell scoring were performed using an ImageXpress Pico High-Content imaging system (Molecular Devices).

Transcriptome profiling and quantitative PCR analysis

RNA was extracted using the total RNA purification kit by Norgen Biotech Corp, following the manufacturer's guidelines. Quantification of total RNA samples was performed with a Qubit HS RNA assay (ThermoFisher Scientific), and fragment size was evaluated with a Fragment Analyzer HS NGS assay (AATI). RNA quality numbers (RQNs) of 8.0 and 6.0 (or higher) were considered satisfactory for human cultured cells and primary tumor library construction, respectively. Library construction was performed with a Truseq RNA v2 (Illumina). Libraries were prepared with unique barcodes compatible with the Illumina NextSeq 500 platform. Quantification of libraries and fragment size evaluation were performed with the Qubit HS DNA and Fragment Analyzer HS NGS assays, respectively. Libraries were normalized to the same concentration, and samples were pooled in equal amounts. Next-generation RNA sequencing was performed on an Illumina NextSeq 500 platform at StemCore facility (RRID:SCR_012601) using the NextSeq System Suite v2.2.0, according to 1 x 75 bp cycles of single-end sequencing, yielding 25 million reads per sample. PhiX ssDNA was spiked in each sample and used as a technical control for clustering reactions. For quantitative PCR analysis, cDNA was synthesized from 1 μg of total RNA using the SuperScript VILO cDNA Synthesis Kit (Invitrogen). qPCR reactions were carried out using Power SYBR Green Master Mix (ThermoFisher Scientific) per the manufacturer's recommendation. Amplification was performed using a Bio-Rad CFX96 Real-Time PCR System. The primer sequences used in this study are presented in Supplementary Table 13. All reactions were normalized to GAPDH as a reference gene, and relative gene quantification was calibrated against vehicle/control-treated samples according to the Pfaffl method[63].

Bioinformatics analysis

For RNA-seq transcriptome profiling, raw sequence data were processed with fastp v0.20.1[64] to perform automatic adapter trimming and read quality filtering, retaining reads with at least 60% of bases having Q≥15 and no more than 5 'N' bases. Transcripts were quantified using the Salmon transcript abundance method (v1.3.0) [65]. Data were loaded into R (v4.0.2) using the tximport library[66], and the gene/count matrix was filtered to

retain only genes with five or more mapped reads in two or more samples. Transposable element transcript profiling was conducted using the TEtranscripts package[67]. Differential expression between treatments and shCTRL/DMSO/vehicle replicates was calculated using the DESeq2 lfcShrink() function (v1.34.0)[68] by applying the apeglm method (v 1.12.0)[69]. Multiple testing correction was performed using the Benjamini-Hochberg's method and lists of significantly DE genes were identified using a q-value (*i.e.*, a corrected p-value) with a cut-off of 0.05. Hierarchically clustered heatmaps were generated with the pheatmap library (v1.0.12) (https://cran.r-project.org/package=pheatmap) using the R hclust function for hierarchical clustering. Venn diagrams of overlapping gene sets were generated with the R VennDiagram package (v1.6.20). Volcano plots were generated with the EnhancedVolcano package with points colored relative to p-value and log2FoldChange cutoffs. Gene signature enrichment analysis (GSEA) was performed using GSEA Software (v4.0.3)[70]. Gene ontology analysis was performed using the ICGC Data Portal v6.3.3 (https://dcc.icgc.org/), where enrichment analysis was performed against GO Molecular Function, GO Biological Process and GO Cellular Component with a p-value threshold of 0.01. Stem cell index calculation was performed using a one-class logistic regression machine-learning algorithm, as previously described[12]. ChIP-seq analysis from human primary colon CSC-enriched populations was performed as described in Bergin et al.[13]. Briefly, reads from GSE82131 data set were quantified in 1kb bins genome-wide for G9a and H3K9me2. Bins were filtered against the ENCODE blacklist and mitochondria as well as unmapped contig assemblies were excluded. Top 20K signal/bins for both G9a and H3K9me2 were overlapped, yielding 1,392 co-enriched regions. Nearest gene annotation was performed using the R ChIPseeker package (v1.38.0). A list of 968 genes associated with ≥1 bin(s) is presented in Supplementary Table 4. Top-50 lists of genes co-occupied by G9a/H3K9me2 in human colon CSCs upregulated by VXN treatments in HT29 and HIEC cells, used for GO and transcription factor binding site enrichment analyses (performed using DAVID web portal (v6.8) (https://david.ncifcrf.gov) are presented in Supplementary Table 4. scRNA-seq analysis was performed on the GSE132465 dataset, comprising 63,689 cells from 23 primary CRC and 10 normal mucosa samples, using the Seurat R package[71]. Chromatin immunoprecipitation (ChIP) data on transcription factor binding around the *EHMT2* transcription start site were obtained from ChIP-Atlas (https://chip-atlas.org) and analyzed through the Signaling Pathways Project online platform (SSP; https://www.signalingpathways.org/ominer)[72]. RRBS data were generated by Richard Myers' laboratory (HudsonAlpha Institute for Biotechnology), obtained from the ENCODE portal database, and visualized using the UCSC Genome Browser[73]. Drug response correlation analysis was performed using the PRISM drug repurposing resource (https://depmap.org/repurposing), part of the DepMAP portal (Supplementary Note 2)[25]. Protein-protein interaction network mapping was performed using the STRING Database v12.0 (https://string-db.org/)[74]. Compound activity prediction analysis, including putative target, main metabolites, and cellular localization, was performed using MetaDrug via a non-downloadable online version of the software v6.26 (Thomson Reuters/Clarivate) https://portal.genego.com/.

Single-cell protein analysis

Single-cell protein analyses of CRC tumor samples and human cell lines were performed using the ProteinSimple Milo platform according to the manufacturer's recommendations[38]. Briefly, standard scWest chips were used to capture individual cells and perform size-based electrophoretic protein separation. Single-cell suspensions were loaded onto the chips and inserted into the Milo instrument for cell lysis, in-chip migration, and UV crosslinking to immobilize separated proteins. Chips were probed with primary antibodies, followed by fluorescent secondary antibodies (Supplementary Table 12) for multiplexed detection of each target protein using a GenePix 4000B fluorescence microarray scanner (Molecular Devices). Detailed chip probing protocol can be found at: https://www.bio-techne.com/p/single-cell-western/milo_p100. Peak identification and quantification was performed using the Scout Software v2.2.1beta (ProteinSimple). Each signal was inspected to confirm that it was associated with a peak located at the correct distance from the well centre. Histone H3 was used as a cell occupancy control.

RNAi-based knockdown and ectopic expression experiments

Small hairpin RNA-mediated knockdown of *SLC6A3* was achieved using the doxycycline-inducible pInducer10 expression vector, including an RFP fluorescent reporter. Both, *SLC6A3*-targeting and non-silencing scrambled (shCTRL) hairpin sequences (Supplementary Table 13) were inserted in the pInducer10 vector (gift from Stephen Elledge; Addgene #44011) at the Genome Engineering and Molecular Biology (GEMb, RRID:SCR_022954) core facility at the University of Ottawa. These constructs were used for lentiviral particles production via co-transfection with pMD2. G (Addgene #12259) and psPAX2 (Addgene #12260) vectors in 293-FT cells using Lipofectamine LTX Reagent (ThermoFisher). Lentiviral particles were harvested at 24 and 48 h post-transfection, through conditioned media collection, centrifugation (to remove cells and debris), filtration through a 0.45 µm filter and then ultracentrifuged at 20,000 x g for 2 hr at 4°C [19]. Lentiviral transductions were performed on $5x10^5$ HT29 or HCT116 cells/well in 6-well plates and incubated with 0.5 mL of viral suspension + 8 µg/mL of polybrene (Millipore Sigma) for 16 hours. shRNA expression was induced using 100 ng/mL of doxycycline (DOX). For siRNA-based knockdown of *SLC6A3* expression, 5000 cells were seeded per well in 96-well plates and cultured for 48 hours. A pool of 6 independent predesigned *SLC6A3*-targeting siRNA duplexes (ThermoFisher Silencer Select, cat# 4392420) was diluted to 10 nM in 10 mL of OptiMEM and mixed with 0.1 mL of RNAiMAX diluted in 10 mL of OptiMEM. Preparations of a scrambled non-silencing siRNA duplex (siCTRL) were used as a control. Cells were washed with 100 mL of OptiMEM and incubated with 100 µl of siRNA-containing mixture for 6 hours. Cells were cultured for an additional 42 hours in fresh media (McCoy's, 10%FBS). *SLC6A3* knockdown experiments were performed 24 h post transfection. The human *EHMT2*/G9a expression plasmid (pLenti-GIII-CMV-EHMT2-GFP-2A-Puro) was purchased from Applied Biological Materials (ABM) and used along with the empty pLenti-GIII-CMV-GFP-2A-Puro vector to generate lentiviral particles and transduce HCT116 cells as described above.

Organoid and spheroid formation assay

Ex vivo assessment of tumor-initiating capacity in human primary colorectal tumor specimens was performed using a documented serial organoid formation protocol[47]. Briefly, patient-derived spheroids enriched with colorectal tumor-initiating cells dissociated using TrypLE reagent (ThermoFisher) and mixed with Matrigel in a specialized serum-free culture media (CSC media)[47] (1:1 ratio) to obtain a 1-cell/µl density. Mixtures were immediately plated as 300 µl domes in 6-well plates and incubated for 15 minutes at 37°C for Matrigel polymerization. Then, 2.5 mL of CSC media containing different doses of VXN, 5-FU, or vehicle control (DMSO) was added to each well. Drug treatment was maintained for 7 days, followed by a 7-day drug-free incubation period. At day 14, the plates were imaged using an ImageXpress Pico high-content imaging system to determine organoid counts and size using CellReporterXpress software (v2.8.2). For secondary organoid plating, primary organoids resulting from control and drug-treated wells were dissociated using gentle dissociation reagent (STEMCELL Technologies) and replated as described above but at a 50-cell/µl density[13]. Secondary organoids were grown for 14 days in sphere culture media with no further drug treatment. For organoids grown from HCT116 cells, VXN and/or Cytosporone B treatments, siRNA transfections, and EHMT2-GFP/CTRL-GFP lentiviral transductions were performed 24 hours prior to single-cell seeding. For organoid-based clonogenic experiments involving sh*SLC6A3* knockdown and shCTRL, HCT116 cells were induced with DOX 24 h post-transduction and induction was maintained over 72 h prior to single-cell seeding. RFP/GFP-positive or calcein green-stained organoid structures were imaged using an ImageXpress Pico high-content imaging system and scored using CellReporterXpress software (v2.8.2)[47]. 3D Spheroid formation experiments were performed in Corning Elplasia 96-well round bottom ultra-low adhesion microplates (Fisher Scientific) according to the manufacturer's recommendations. MACS-sorted $CD133^{High}$ and $CD133^{Low}$ suspensions of

primary colorectal tumor tissues were treated with VXN (0.125 - 1 μM, 48 h) or DMSO in CSC culture media. $CD133^{High}$ and $CD133^{Low}$ cultures were dissociated and seeded in Elplasia microplates (100 cells per well in CSC culture media). shRNA-transduced and DOX-induced HT29 cells were also plated at 100 cells per well in CSC media. At 7 days post-plating, live spheroids inside microcavities were stained with calcein green and imaged using an ImageXpress Pico high-content imaging system. Spheroid counts and size measurements were performed with CellReporterXpress software (v2.8.2).

Protein array analysis

Kinome proteomic profiling was performed using the R&D Systems Proteome Profiler Human Phospho-kinase chip technology (ARY003B) according to the manufacturer's instructions. HT29 cells were treated with VXN for 0, 6, 12, and 24 hours, and lysates were immediately incubated with Human Phospho-Kinase chips. Signals from each chip/condition were produced by enhanced chemiluminescence (Millipore Sigma Immobilon), and the phosphorylation state of each target analyzed was quantified by integrating spot specific ECL signals using ImageJ software (v1.53k)[75]. Data are presented as heat maps of log2-fold-change relative signal intensity for 6, 12, and 24 h VXN treatments vs. control.

Molecular docking analysis

The X-ray structure of the Drosophila dopamine transporter complexed with cocaine was obtained from the RSCB PDB database (4XP4). UCFS Chimera (v1.4) was used to convert the vanoxerine SMILES string into a PDB file. Molecular docking was performed using PyRx (v0.8), running AutoDock Vina, and a built-in PDBQT converter Open Babel was used to determine the docking energy for a minimum of 3 runs at an exhaustiveness ("E") of 50 and an RMSD = 0, as previously reported[62]. Output files from molecular docking analysis were generated with PyMOL software (v.2.4.x).

Dopamine ELISA assay

To detect the presence of dopamine in human colorectal cancer cells and other experimental models used in this study, a high-sensitivity dopamine ELISA kit was used according to the manufacturer's instructions (ENZO Life Sciences, ENZ-KIT188-0001). Briefly, 27 independent sample conditions, including fresh culture media, cell conditioned media (VXN-treated vs. untreated), cell lysates (VXN-treated vs. untreated), and dopamine standards, were tested in biological triplicate, and colorimetric detection was performed at 450 nm using a Synergy H1 Agilent-BioTek plate reader and the BioTek Gen5 software (v3.15.15).

Chromatin immunoprecipitation (ChIP) and methylated DNA pulldown assays

For each ChIP condition (DMSO, VXN 24 h, IgG control), $2x10^6$ HCT116 cells were cross-linked using 1% formaldehyde, quenched with 0.125 M glycine, and harvested by cell scraping. Chromatin was fragmented by sonication in buffer containing 1% NP-40 and 0.1% SDS to obtain fragments of ~250 bp length. Sonicated DNA was subjected to immunoprecipitation using 5 μg of anti-phospho-Nur77 (S351), anti-CTCF, anti-C/EBPb, and anti-ZNF143 primary antibodies (Supplementary Table 12) conjugated with Dynabeads Protein G (ThermoFisher). Control IgGs from corresponding isotypes (5 μg) were used as negative controls. Immunoprecipitated DNA was reverse cross-linked, purified using a Chromatin IP DNA purification kit (Active Motif), and subjected to quantitative PCR analysis to detect the *EHMT2* proximal promoter fragment (Supplementary Table 13). Relative chromatin enrichment values were calculated based on the standard curve equation[19,62]. For MBD2-based locus-specific quantification of methylated

DNA, genomic DNA was extracted from HCT116 cells or *in vivo*-treated mouse primary tumors using the DNeasy Blood & Tissue kit (Qiagen). Next, DNA samples were sonicated to obtain 500 – 800 bp fragments. Methylated fragments (5-meC) were captured using the EpiMark Methylated DNA Enrichment Kit (New England Biolabs) according to the manufacturer's instructions[13]. Input and output fractions were analyzed by qPCR to assess variation in human (*EHMT2*) and mouse (*Ehmt2*) G9a proximal promoter methylation. Pulldowns executed with non-MBD2-conjugated beads were used as negative controls.

Generation of patient-derived LGR5-GFP CRC tissues

CRISPR-Cas9 knock-in of *LGR5* exon 18 to insert a GFP reporter cassette tracing endogenous *LGR5* expression in primary CRC tissues was performed at the GEMb core facility in the Faculty of Medicine at the University of Ottawa, using the HR180-LGR5-GFP construct generated by Dr. Toshiro Sato (Addgene 129092)[48] and gRNA sequences reported in Supplementary Table 13. The construct includes an mRuby fluorescence cassette driven by EF1 promoter allowing visual confirmation of knock-in. Briefly, cell preparations from CSC-enriched spheroids (patient #92, Supplementary Table 8) were transduced by electroporation with the knock-in *LGR5*-targeting construct system. Electroporated cells were grown in CSC culture media under non-adherent conditions and subjected to puromycin selection (2 μg/ml). RFP-positive spheroids were manually isolated and expanded prior to EF1-RFP-Puro cassette excision using human adenovirus type5 Cre recombinase-expressing particles transduction[76]. GFP+/RFP- spheroids were used for subsequent organoid growth experiments. Targeting construct integration (Ad-Cre-) and Cre-excised EF1-RFP-Puro (Ad-Cre+) knock-ins were validated by PCR (Extended Data Figure 8j)[48], using primer sequences reported in Supplementary Table 13.

Serial in vivo tumor transplantation assay

Assessment of the capacity of VXN to target CSC functions *in vivo* was conducted in a serial syngeneic mouse tumor transplantation assay[62]. Briefly, colorectal adenocarcinoma MC38 (C57BL/6) and CT26 (BALB/c) cultures were dissociated and resuspended in a 1:1 HBSS:Matrigel mixture prior to subcutaneous injection into the flanks of 6 to 8-week-old C57BL/6 (Charles River, C57BL/6NCrl) and BALB/c (Charles River, BALB/cAnNCrl) female mouse recipients, at a density of $1x10^6$ cells per injection. Seven days post-injection, daily doses of vanoxerine (25 mg/kg) or control saline (HBSS vehicle) were intraperitoneally injected into tumor-bearing animals for 10 days. Primary tumour growth was measured daily using a digital caliper. The ellipsoidal tumour volume was calculated according to V = (L x W x W)/2. Mouse behavioural and clinical assessments were performed daily following drug administration, according to uOttawa animal care committee guidelines. On experimental day 18, primary tumors were surgically extracted, dissociated with 100 U/mL collagenase IV and 100 μg/mL DNase I, and passed through a 70 μm strainer to eliminate debris and cell clumps. Tumor cells were reinjected subcutaneously into the flanks of secondary mouse recipients. Secondary mice injected with tumor cells from control and drug-treated groups were maintained for 14 days without any treatments. At endpoint, secondary recipient mice were injected with 10 nmoles of IRDye-800CW-2-deoxyglucose (IR800-2-DG) in the tail vein, and the presence/absence of secondary tumors was assessed by *in vivo* fluorescence imaging using an IVIS Spectrum In Vivo Imaging System and the Living Image software v4.7.3 (PerkinElmer) at the University of Ottawa Preclinical Imaging Core Facility (RRID:SCR_021832). Cell doses ranging from $1x10^6$ to $2.5x10^4$ were injected into secondary recipients to establish a limiting dose assay for secondary tumor formation[8]. For experiments evaluating the impact of immune checkpoint inhibition on tumor growth, daily injections of 100μ of an anti-PD-L1 (clone 10F.9G2, Millipore Sigma)[77] vs. control IgG were performed in primary mouse recipients over 4 days between experimental days 14 and 17. All mice were housed in ambient temperatures (20-25°C) with humidity maintained between 20-70% and following 12h light and 12 dark cycles. Food and water were available ad libitum.

Flow cytometry

In vivo-treated mouse primary CRC tumors (saline vs. VXN, 10 days) were dissociated using a gentle magnetic-activated cell sorting dissociator (Miltenyi). Following dissociation, the single-cell suspension was passed through a 40-µm filter, and the cells were washed and resuspended in PBS for staining. Specifically, 100K tumor cells per mL were incubated with antibodies for 1 hour at 4°C, washed with 10 volumes of PBS and then stained with the Zombie NIR Fixable Viability Dye (BioLegend) for 20 min in PBS to label and exclude dead cells during the analysis. Single-cell suspensions were stained using anti-Sca-1-BV510 and anti-mouse CD44-BV421 (see Supplementary Table 12). Flow cytometry analysis was performed at the University of Ottawa Flow Cytometry and Virometry Core Facility (RRID:SCR_023306) on a BD LSR Fortessa 16-colour analyser with FACSDIVA software (v9.0), and data analysis was conducted using FlowJo v10.9 (Tree Star Inc)[19]. A description of the gating strategies is detailed in Supplementary Fig. 2.

Statistics & Reproducibility

GraphPad Prism v.10.1.0 was used for statistics. Results are expressed as means ± SEM unless otherwise indicated in figure legends. The number of independent experiments performed, and biological replicates implicated are indicated as "n" in the figure legends. See source data for exact values for each experiment with numerical graphic presentation. All statistical analyses were generated from at least three biological replicates, except for specific data derived from RNA-seq, where two biological replicates per group were subjected to the Benjamini Hochberg method for multiple testing correction and false discovery rate estimation (q-values (adj. p-value). p and q-values below 0.05 were considered statistically significant. Technical replicates plotting was clearly indicated in the figure legend and in source data. No statistics were derived from technical replicates. All statistical tests and multiple corrections are mentioned in the figure legends. Data distribution was assumed to be normal, but this was not formally tested. No statistical method was used to pre-determine sample size, but our sample sizes are similar to those reported in previous publications[14,18,78]. No data were excluded from the analyses. All animals were randomized before treatment with saline, VXN, and immune checkpoint inhibitor aPD-L1. Randomization was not applied to *in vitro*, and *ex vivo* experiment design. The investigators were blinded during animal experiments and high-content imaging data acquisition. Blinding was also applied to all next-generation sequencing data generated in this study, where technical staff were not provided with sample identifying information. For all other experiments, investigators were not blinded during procedures and outcome assessment.

Reporting summary

Further information on research design is available in the Nature Portfolio Reporting Summary linked to this article.

ONLINE METHODS REFERENCES

61 van Ineveld, R. L., Ariese, H. C. R., Wehrens, E. J., Dekkers, J. F. & Rios, A. C. Single-Cell Resolution Three-Dimensional Imaging of Intact Organoids. *J Vis Exp* (2020). https://doi.org/10.3791/60709

62 Masibag, A. N. *et al.* Pharmacological targeting of Sam68 functions in colorectal cancer stem cells. *iScience* **24**, 103442 (2021). https://doi.org/10.1016/j.isci.2021.103442
63 Pfaffl, M. W. A new mathematical model for relative quantification in real-time RT-PCR. *Nucleic Acids Res* **29**, e45 (2001).
64 Chen, S., Zhou, Y., Chen, Y. & Gu, J. fastp: an ultra-fast all-in-one FASTQ preprocessor. *Bioinformatics* **34**, i884-i890 (2018). https://doi.org/10.1093/bioinformatics/bty560
65 Patro, R., Duggal, G., Love, M. I., Irizarry, R. A. & Kingsford, C. Salmon provides fast and bias-aware quantification of transcript expression. *Nat Methods* **14**, 417-419 (2017). https://doi.org/10.1038/nmeth.4197
66 Soneson, C., Love, M. I. & Robinson, M. D. Differential analyses for RNA-seq: transcript-level estimates improve gene-level inferences. *F1000Res* **4**, 1521 (2015). https://doi.org/10.12688/f1000research.7563.2
67 Jin, Y. & Hammell, M. Analysis of RNA-Seq Data Using TEtranscripts. *Methods Mol Biol* **1751**, 153-167 (2018). https://doi.org/10.1007/978-1-4939-7710-9_11
68 Love, M. I., Huber, W. & Anders, S. Moderated estimation of fold change and dispersion for RNA-seq data with DESeq2. *Genome Biol* **15**, 550 (2014). https://doi.org/10.1186/s13059-014-0550-8
69 Zhu, A., Ibrahim, J. G. & Love, M. I. Heavy-tailed prior distributions for sequence count data: removing the noise and preserving large differences. *Bioinformatics* **35**, 2084-2092 (2019). https://doi.org/10.1093/bioinformatics/bty895
70 Subramanian, A. *et al.* Gene set enrichment analysis: a knowledge-based approach for interpreting genome-wide expression profiles. *Proc Natl Acad Sci U S A* **102**, 15545-15550 (2005). https://doi.org/10.1073/pnas.0506580102
71 Lee, H. O. *et al.* Lineage-dependent gene expression programs influence the immune landscape of colorectal cancer. *Nat Genet* **52**, 594-603 (2020). https://doi.org/10.1038/s41588-020-0636-z
72 Ochsner, S. A. *et al.* The Signaling Pathways Project, an integrated 'omics knowledgebase for mammalian cellular signaling pathways. *Sci Data* **6**, 252 (2019). https://doi.org/10.1038/s41597-019-0193-4
73 Davis, C. A. *et al.* The Encyclopedia of DNA elements (ENCODE): data portal update. *Nucleic Acids Res* **46**, D794-D801 (2018). https://doi.org/10.1093/nar/gkx1081
74 Szklarczyk, D. *et al.* STRING v10: protein-protein interaction networks, integrated over the tree of life. *Nucleic Acids Res* **43**, D447-452 (2015). https://doi.org/10.1093/nar/gku1003
75 Mailly, L. *et al.* Clearance of persistent hepatitis C virus infection in humanized mice using a claudin-1-targeting monoclonal antibody. *Nat Biotechnol* **33**, 549-554 (2015). https://doi.org/10.1038/nbt.3179
76 Baron, K. D. *et al.* Recruitment and activation of SLK at the leading edge of migrating cells requires Src family kinase activity and the LIM-only protein 4. *Biochim Biophys Acta* **1853**, 1683-1692 (2015). https://doi.org/10.1016/j.bbamcr.2015.04.003
77 Hasim, M. S. *et al.* When killers become thieves: Trogocytosed PD-1 inhibits NK cells in cancer. *Sci Adv* **8**, eabj3286 (2022). https://doi.org/10.1126/sciadv.abj3286

78 Orlando, L. *et al.* Chemical genomics reveals targetable programs of human cancers rooted in pluripotency. *Cell Chem Biol* (2023). https://doi.org/10.1016/j.chembiol.2023.06.004

DATA AVAILABILITY

All sequencing data generated in this study and supporting these findings were deposited at Gene Expression Omnibus under accession codes GSE154057, GSE207032, GSE226324, and GSE226377. Single-cell RNA sequencing data that support the findings of this study is available at GEO under accession code GSE132465. Reposited ChIP-seq data were re-analysed in this study and the original dataset is available in GEO under accession code GSE82131. The human colon adenocarcinoma dataset used to derive mRNA stem cell indexes from the TCGA Research Network: http://cancergenome.nih.gov/. Other databases/datasets used in this study include PRISM drug repurposing portal (https://depmap.org/repurposing), the RSCB PDB database (https://www.rcsb.org)accession number 4XP4), the Signaling Pathways Project online platform (https://www.signalingpathways.org/ominer), the ENCODE project database (https://www.encodeproject.org/), the ChIP Atlas database (https://chip-atlas.org/), the PerMM web portal (https://permm.phar.umich.edu), and the BioGrid database (https://thebiogrid.org/). Source data for Fig. 1-8 and Extended Data Fig. 1-10 have been provided as Source Data files. All other data supporting the findings of this study are available from the corresponding author on reasonable request.

CODE AVAILABILITY

All the code used in this study is available at https://gitlab.com/ohri/the-dopamine-transporter-antagonist-vanoxerine-inhibits-g9a-and-suppresses-cancer-stem-cell-functions-in-colon-tumors.

ACKNOWLEDGMENTS

This work was supported by grants from the Cancer Research Society (#22778, #24039, and #942363, to Y.D.B.), the Ontario Ministry of Research, Innovation and Science (ER17-13-012, to Y.D.B.), the CIHR (PJT-17354 and 201302MFE-300637-197755, to Y.D.B.), and the Natural Sciences and Engineering Research Council (RGPIN-2018-06521 and DGECR-2018-00029, to Y.D.B.). The GEMb facility is supported by CFI-36490, CFI-37607 and CFI-36940. The authors would like to thank Drs. Mickie Bhatia (McMaster University), and Jean-François Beaulieu (Université de Sherbrooke) for sharing key cell models. Thanks to Drs. Christopher Porter and Gareth Palidwor (the Ottawa Bioinformatics Core Facility, OHRI, RRID:SCR_022466) for computational analysis, as well as Dr. Chloë Van Oostende-Triplet at the uOttawa Cell Biology and Image Acquisition Core Facility (RRID:SCR_021845). Collection of human tissue for this study was made possible by the Global Tissue Consent and Collection Program at the Ottawa Hospital Research Institute and Dr. Catherine O'Brien at the Toronto General Hospital Research Institute. Thanks to Dr. Tony J. Collins for critical input on HTS, to Dr. Luc A. Sabourin and Samuel Delisle for providing Ad-Cre particles. Thanks to François M. Desrochers and Ajanta Chatterji for technical assistance. Graphic elements of Figures 1, 2, 4, 5, 6, and 7, and Extended Data 8 and 9 were generated using BioRender.

AUTHOR CONTRIBUTION STATEMENT

C.J.B., and A.Z., designed and performed experiments, analyzed/interpreted data and wrote the manuscript; A.M.dS. performed experiments, analyzed and interpreted data; T.F. performed experiments and tissue pathological analysis; J.R.H. A.N.M, G.A. and T.S. performed experiments; M.S.S. analyzed data; M.T. provided results interpretation and wrote the manuscript; R.C.A. provided primary tissue samples and results interpretation; M.A. designed experiments, performed experiments, provided results interpretation, and wrote the manuscript; Y.D.B. supervised the project, designed experiments, performed experiments, provided results interpretation, and wrote the manuscript.

COMPETING INTERESTS STATEMENT

Y.D.B. relatives hold shares in Gibiex Biotech Inc. M.A. received monetary compensation from Alloy Therapeutics for consulting. M.A. is under a contract agreement to perform sponsored research with Actym Therapeutics and Dragonfly Therapeutics. Neither consulting nor sponsored research are related to the present article. The remaining authors declare no competing interests.

FIGURE LEGENDS

Fig. 1 | Multiparametric high-throughput phenotypic drug screening pipeline identifies vanoxerine as a repurposed compound displaying cancer-selective growth inhibition effects.

a, Schematic of the high-throughput phenotypic pipeline used to identify repurposed drugs inducing loss of the pluripotency marker Oct4, decreased H3K9me2 deposition, and cancer-selective growth inhibition. **b,** Structure of three main hits identified by phenotypic screening on t-hESCs. **c,** Micrographs showing simultaneous inhibitory effect of VXN (5 μM, 48h) on Oct4 expression (pluripotency) and H3K9me2 deposition in t-hESCs (n=2 samples, 2 independent experiments, scale bar: 100 μm). **d, e,** VXN shows selective growth inhibition in all CRC cell lines tested (HT29: n=3, SW480: n=2, and HCT116: n=3 biological replicates, 1 independent experiment) vs. normal human intestinal progenitors HIEC (n=4 biological replicates, 1 independent experiment). **f,** Dose-response inhibition of H3K9me2 levels in human CRC cells (HT29) upon 48 h of VXN treatment. Loss of H3K9me2 is accompanied by increased levels of the activating mark H3K9ac. Average optical density ratios for each histone mark vs. loading control total H3 are presented (n=3 biological replicates, 3 independent experiments). **g,** EdU incorporation assays indicate that VXN (48 h, 10 μM, n=3 biological replicates) blocks proliferation of HT29 cells compared to vehicle control (DMSO: n=4 biological replicates) (2 independent experiments, mean values +/- SEM, ***: p=0.0005, unpaired two-tailed t-test, scale bar: 100 μm). **h,** Active caspase-3/7 staining (CellEvent) supports significant apoptosis induction in HT29 cells (n=4 biological replicates) but not in HIEC (n=4 biological replicates) cells following VXN treatments (48 h, 10 μM). Staurosporine (n=3 biological replicates) was used as a positive control (2 independent experiments, mean values +/- SEM, two-way ANOVA with Tukey's multiple comparisons test, p-values (vs. DMSO) are indicated on graph, scale bar: 100μm). See also Extended Data Fig. 1, and Supplementary Tables 1-3.

Fig. 2 | Multi-omic characterization of VXN cancer-selective effect on cell functions.

a, Transcriptome profiling identifies genes modulated by VXN in colon cancer cells (HT29) but not in normal HIEC cells (RNA-seq: n=2 biological replicates, 1 independent experiment). Gene signature enrichment analysis (GSEA) suggest a downregulation of key cancer and stemness pathways, and increased INF type-1 response in VXN-treated CRC cells. Circles and bars represent normalized enrichment scores (NES) for VXN-treated HT29 and HIEC, respectively (vs. DMSO) and nominal (NOM) p-value is represented by color-coding (Dashed lines indicate a +/-1.3 NES cut-off , exact NES and NOM p-values available in Source Data). **b,** Viability response to VXN in the DepMap CRC cell line panel correlates with the epigenetic drug romidepsin (n=33 cell lines, Pearson coefficient: 0.34, *: p=0.049). **c,** VXN decreases G9a protein levels in HT29 (n=3 biological replicates) and t-hESCs (n=4 biological replicates). Actin was used as a loading control (1 independent experiment, mean values +/- SEM, p-values (vs. control) are indicated on graph, unpaired two-tailed t-test). **d,** ChIP-seq analysis of G9a and H3K9me2 co-occupied loci performed in human primary colon CSC-enriched fraction (n=1 sample series). An integrative analysis comparing co-occupied annotated regions with genes modulated by VXN only in

HT29 cells (RNA-seq, n=2 biological replicates, 1 independent experiment) was performed to identify direct G9a targets impacted by drug treatments in colon cancer. **e,** Bubble plot of gene ontology terms (GOTERM_BP) enriched in lists of top-50 upregulated ("derepressed") G9a/H3K9me2 target genes upon VXN treatments in HT29 and HIEC cells (one-sided p-values for Fisher's Exact test available in Source Data). See also Extended Data Fig. 2-3, and Supplementary Tables 4-6.

Fig. 3 | Dopamine transporter (DAT) distribution across human colorectal intratumor heterogeneity.

a, Western blot assessment of DAT levels in normal intestinal epithelial cells (HIEC), human (HT29, HCT116) and mouse (MC38) CRC cells, and t-hESCs. DAT is increased in CSC-enriched spheroid fractions vs. heterogenous organoids grown from corresponding human primary CRC samples (n=3 biological replicates, 3 independent experiments). Average optical density ratios for DAT vs. actin loading control are presented. **b,** Immunofluorescence detection of DAT in CSC-enriched spheroids and heterogeneous CRC tumor organoids imaged by confocal microscopy (upper panel). Arrowhead indicates a DAT-positive cell observed in heterogeneous organoids. DAT immunostaining of primary human colon adenocarcinoma sections (lower panel) highlights a similar punctate pattern in a rare subset of tumor cells (n=3 independent patients, scale bar: 25 μm). E-cadherin was used to stain epithelial-like structures. **c,** Immunofluorescence staining of DAT in HCT116 CRC cells. Co-staining was performed using phalloidin (filamentous actin), the early endosome marker Rab5a, and the late endosome/lysosome marker LAMP1 (n=3 biological replicates, 2 independent experiments, scale bar: 10 μm). **d,** Single-cell protein quantification of DAT-positive cell frequency in bulk primary CRC adenocarcinoma (n=3 CRC patient samples, Patient #411 presented) and patient-derived CSC-enriched spheroids (n=1 CRC patient sample, Patient #181). Scatter plots of DAT and CD133 signal intensity are showed vs. cell occupancy control histone H3. DAT-positive cells were found in both, CD133-positive and CD133-negative fractions. **e,** Single-cell protein analysis comparing DAT distribution and phospho-H3S10 was performed in CD133-sorted fractions from human primary colon adenocarcinoma (n=3 CRC patient samples, Patient #409 presented) and patient-derived CSC-enriched spheroids (n=1 CRC patient sample, Patient #181). Single-cell protein analysis of **f,** chromogranin A and **g,** neurofilament distribution across primary bulk colorectal adenocarcinoma samples and neuroblastoma cell populations. Fluorescence intensity per individual cell is presented in the scatter plots. DAT-positive cells are highlighted in red. Total histone H3 was used as a cell occupancy control (n=3 CRC patient samples, Patient #397 presented). **h,** Single-cell protein quantification of DAT-positive cells in DMSO (n=3235 cells) and VXN-treated (n=1606 cells) HT29 populations (1 independent experiment, ***: $p<0.0001$, Fisher's exact test). See also Extended Data Fig. 4, and Supplementary Table 8.

Fig. 4 | Vanoxerine alters stem-like functions in colon cancer cells by blocking DAT.

a, Dox-inducible knockdown of *SLC6A3* in human HCT116 cells reduces G9a protein levels (*: p=0.0257), along with decreased DAT levels (*: p=0.0483) vs. non-silencing scrambled control (shCTRL) (n=3 biological replicates, 1 independent experiment, mean values +/- SEM, unpaired two-tailed t-test). **b,** Expression of EHMT2 transcript is reduced in RFP-positive *SLC6A3* knockdown HCT116 cells

independently of VXN treatments (48h, 10 μM) (n=3 biological replicates, 1 independent experiment, mean values +/- SEM, p-values indicated on graph, one-way ANOVA with Dunnett's multiple comparisons test). **c,** Effect of *SLC6A3* knockdown in HCT116 cells on intestinal progenitor markers vs. control shRNA (RNA-seq: n=3 biological replicates, 2 independent experiments, FPKM values, paired two-tailed t-test, p-values indicated on graphs). **d,** Clonogenic organoid formation assay using HCT116 cells transduced with Dox-inducible sh*SLC6A3* or shCTRL expression vectors. Data are presented as organoid formation frequency and residual organoid size for shRNA-expressing organoids (RFP-positive) (n=4 biological replicates, 2 independent experiments, mean values +/- SEM, p-values indicated on graphs, unpaired two-tailed t-test). **e,** Comprehensive GSEA highlighting commonly modulated signatures in *SLC6A3* knockdown (vs. shCTRL, n=3 biological replicates, 2 independent experiments) HCT116 cells, VXN-treated HCT116 (n=3 biological replicates, 2 independent experiments), HT29 (n=2 biological replicates, 1 independent experiment), and t-hESCs (n=2 biological replicates, 1 independent experiment), as well as BIX-01294-treated t-hESCs (n=2 biological replicates, 1 independent experiment) (vs. DMSO). Consistent negative enrichment scores are observed across all experimental conditions for genes upregulated in colorectal cancer (Grade), genes associated to pluripotent stem cells (Wong), and Myc transcriptional targets (color scale: NES values, circle size: NOM p-values. Exact NES and NOM p-values available in Source Data). **f,** Kinome proteomic profiling of 6 h, 12 h, and 24 h VXN-treated HT29 cells (10 μM) identifies significant changes in AKT (T308/S473), eNOS (S1177), FAK (Y397), and p70 S6 kinase (T389) phosphorylation (n=4 biological replicates, 2 independent experiments, mean values +/- SEM, ***: $p<0.0001$, **: $p<0.01$, *: $p<0.05$, exact p-values are in Source Data, one-way ANOVA with Bonferroni's multiple comparisons test, color scale: Log2 fold-change signal vs. vehicle). **g,** *SLC6A3* knockdown recapitulates VXN effect on AKT T308 (n=3 biological replicates) and S473 (n=4 biological replicates) (vs. control) in HT29 cells (2 independent experiments, mean values +/- SEM, **: $p=0.0016$, *: $p=0.0224$). **h,** Single-cell protein analysis on S473-AKT phosphorylation in DAT-positive and negative HT29 cells upon VXN treatment (vs. DMSO) (DAT-positive: DMSO: n=29 cells, VXN: n=19 cells. DAT-negative: DMSO: n=7 cells, VXN: n=8 cells. 1 independent experiment, p-value indicated on graph, unpaired two-tailed t-test). See also Extended Data Fig. 6, and Supplementary Tables 4-5.

Fig. 5 | Vanoxerine is inhibiting G9a expression in colorectal cancer via the AKT-Nur77 axis

a, High-content imaging quantification of phospho-Nur77 (S351) in HCT116 cells treated with DMSO (n=4 biological replicates), AZD5363 (AKTi, 2.5 μM, n=4 biological replicates), VXN (5 μM, n=4 biological replicates), and cytosporone B (CytoB, 10 μM, n=3 biological replicates) over 24 h. The effect of AZD5363 and VXN on p-Nur77 nuclear signal is rescued by co-treatment with CytoB (n=3 biological replicates) (2 independent experiments, mean values +/- SEM, ***: $p<0.0001$, one-way ANOVA with Dunnett's multiple comparisons test, scale bar: 20μm). **b,** qPCR analysis of G9a and other documented Nur77 targets mRNA level in HCT116 cells treated with VXN or VXN+CytoB vs. DMSO (24 h). The number of biological replicates (n) per condition, independent experiments for each gene (Exp), and p-values are indicated on the graphs (mean values +/- SEM, one-way ANOVA with Dunnett' multiple comparisons test). **c,** Clonogenic organoid formation assay using HCT116 cells treated with either VXN alone (1 μM), VXN+CytoB (1 and 10 μM,

respectively), or DMSO control (7 days). Organoid formation frequency is significantly reduced upon VXN treatments, while the addition of CytoB is rescuing tumor initiation capacity in HCT116 cells (n=3 biological replicates from 3 independent experiments, mean values +/- SEM, p-values indicated on graphs, one-way ANOVA with Tukey's multiple comparisons test). **d,** Chromatin immunoprecipitation (ChIP: p-Nur77: n=5 biological replicates, CTCF: n=4 biological replicates) and methylated DNA pulldown (5-meC: n=5 biological replicates) assays measuring the impact of VXN (5 μM, 24 h) on *EHMT2* (G9a) proximal promoter regulation in HCT116 cells (2 independent experiments, mean values +/- SEM, p-values indicated on graphs, unpaired two-tailed t-test), and supporting **e,** the implication of Nur77 in G9a repression upon DAT antagonization. **f,** Organoid formation assay using pLenti-G9a-GFP transduced HCT116 cells (vs. empty-GFP). Ectopic G9a expression rescues tumor-initiating capacity of HCT116 cells treated with VXN (1 μM, 7 days) (n=3 biological replicates from 3 independent experiments, mean values +/- SEM, *: p=0.0165, one-way ANOVA with Dunnett's multiple comparisons test). **g, h,** qPCR analysis of LGR5 (stem cell marker, n=3 biological replicates, 2 independent experiments), DPP4 (intestinal differentiation, n=3 biological replicates, 2 independent experiments) and interferon type-1 response genes IFIT1 (n=3 biological replicates, 3 independent experiments), OAS3 (n=5 biological replicates, 1 independent experiment), and MX1 (n=6 biological replicates, 4 independent experiments) levels upon VXN treatments in pLenti control-GFP and G9a-GFP transduced HCT116 cells (vs. DMSO, mean values +/- SEM, p-values indicated on graphs, One-way ANOVA with Tukey's multiple comparisons test). See also Extended Data Fig. 7.

Fig. 6 | Vanoxerine alters colorectal cancer stem cell functions in patient-derived tumor organoids.

a, Schematic of the serial organoid formation assay using primary human CRC samples to test tumor-initiating function. **b,** Primary and secondary organoid formation frequency observed upon VXN or 5-FU treatments (0.25 - 10 μM, 7 days) vs. DMSO controls. Each dot on the graphs corresponds to one biological replicate. Bar graph represents mean +/- SEM, box plot center line corresponds to median, and whiskers represent min to max values (number of biological replicates (n) from 5 independent patient samples, and p-values are indicated on graphs, one-way ANOVA with Dunnett's multiple comparisons test). **c,** Renderings of CSC-enriched spheroids and primary CRC organoids from fluorescence confocal imaging of Ki-67 and **d,** Bmi1 following VXN treatments (1 μM, 7 days) vs. DMSO (Ki-67: n=3 organoids. Bmi1: DMSO: n=3 organoids, VXN: n=4 organoids. Data from 3 independent patient samples, presented as mean values +/- SEM, **: p=0.0070, #: p=0.0709, unpaired one-tailed t-test, scale bar: 30μm). **e,** Clonogenic capacity assessment of $CD133^{High}$ and $CD133^{Low}$ fractions sorted from patient-derived colorectal tumor spheroids. Subfraction were seeded as single cells in an ultralow adhesion microwell system. **f,** Spheroid formation frequency observed upon single cell plating of $CD133^{High}$ and $CD133^{Low}$ fractions, treated with VXN or DMSO control (48h, 2 independent patients in 2 independent experiments). Each dot on the graph corresponds to one biological replicate ($CD133^{High}$: DMSO: n=20, VXN 0.125 – 0.5 μM: n=3, VXN 1 μM: n=11. $CD133^{Low}$: DMSO: n=22, VXN 0.125 – 0.5 μM: n=3, VXN 1 μM: n=11). Bars represent mean values +/- SEM, p-values are indicated on the graph, two-way ANOVA with Sidak's multiple comparisons test. Live spheroids were visualized using calcein green. **g,** LGR5-GFP knock-in cells

generated from patient-derived CRC tissues were used in tumor organoid formation assays. **h,** Representative pictures of DMSO and VXN-treated (1 μM, 7 days) LGR5-GFP organoids at post-treatment stage (n=4 biological replicates, 4 independent experiments, scale bar: 30μm). **i,** Integrated GFP intensity per organoid was measured by high-content imaging in primary LGR5-GFP organoids at 7-days (DMSO: n=530 organoids, VXN 0.5 μM: n=206 organoids, VXN 1 μM: n=130 organoids), 10-days (DMSO: n=634 organoids, VXN 0.5 μM: n=146 organoids, VXN 1 μM: n=99 organoids), and 14-days (DMSO: n=826 organoids, VXN 0.5 μM: n=243 organoids, VXN 1 μM: n=188 organoids) following treatment initiation p-values indicated on graphs, one-way ANOVA with Dunnett's multiple comparisons test). Dashed line within violin plots corresponds to median. See also Extended Data Fig. 8, and Supplementary Table 8.

Fig. 7 | Vanoxerine alters colorectal cancer stem cell activity *in vivo*.

a, Schematics of the murine syngeneic serial tumor transplantation assay used to measure CSC activity *in vivo*. Only primary mouse recipients were treated with VXN. Presence/absence of secondary tumors was determined by live fluorescence tumor imaging (IVIS, IRDye 800CW 2-DG, 10 nM per mouse). **b,** CRC tumor growth measurement of control saline (vehicle) and VXN-treated (25 mg/kg, 10 days) primary recipient mice (MC38-C57BL/6: Vehicle: n=14 mice, VXN: n=12 mice. CT26-BALB/c: Vehicle: n=6 mice, VXN: n=4 mice). Relative tumor volumes (vs. pre-treatment) are presented for injection days 5 to 10. The number of independent tumors measured for each condition/time point is indicated on graphs (data from 2 independent experiments, p-values indicated on the graph, mixed-effect analysis with Sidak's multiple comparison test). Center line on violins corresponds to median. **c,** Transcriptome profiling in primary MC38 tumors confirms reduced mRNA stem cell index following VXN *in vivo* treatments (25 mg/kg, 10 days) vs. vehicle controls (n=2 independent tumor pairs, 1 independent RNA-seq experiment). Methylated DNA pulldown assays showed increased 5-meC levels at the *Ehmt2* proximal promoter region (n=2 independent tumor pairs, 3 technical replicates per tumor, 2 independent experiments), along with reduced *Ehmt2* (G9a) mRNA expression (FPKM values, n=2 independent tumor pairs, 1 independent RNA-seq experiment) following *in vivo* VXN treatment (vs. vehicle) (bars represent mean values, q-value = 0.0008, calculated from Benjamini-Hochberg test for false discovery rate estimation). **d,** Immunofluorescence staining of H3K9me2 and Ki-67 on histological sections from vehicle and VXN-treated MC38 tumors (Ki-67: Vehicle: n=6 tumors, VXN: n=5 tumors. H3K9me2: Vehicle: n=26 tumors, VXN: n=14 tumors). Data from 3 independent experiments, mean values +/- SEM, p-values are indicated on graphs, unpaired two-tailed t-test, scale bar: 50μm. **e,** Frequency of secondary tumors observed in vehicle and VXN-treated groups in the MC38-C57BL/6 and CT26-BALB/c syngeneic models. Tumor formation rates (per injection site) are represented above each column of the histogram (MC38-C57BL/6: Vehicle: n=16 mice, VXN: n=8 mice. CT26-BALB/c: Vehicle: n=6 mice, VXN: n=6 mice). Data from 2 independent experiments, p-values are indicated on graphs, two-sided Fisher's exact test. Representative live fluorescence tumor images are presented. **f,** Secondary MC38 tumor transplants performed as a limiting dilution assay with doses ranging between $1x10^6$ and $2{,}5x10^4$ cells from vehicle and VXN-treated (25 mg/kg, 10 days) primary recipients. Number of injections per cell doses are indicated on the graph (***: $p<0.0001$, two-sided Fisher's exact test). $1x10^6$ cells: Saline: n=9 mice, VXN: n=3 mice. $5x10^5$ cells: Saline: n=4 mice,

VXN: n=2 mice. $1x10^5$ cells: Saline: n=3 mice, VXN: n=3 mice. $2.5x10^4$ cells: Saline: n=2 mice, VXN: n=2 mice. See also Extended Data Fig. 9, and Supplementary Table 10.

Fig. 8 | Epigenetic changes induced by vanoxerine suppress immune evasion in colorectal tumors

a, Differential expression of transposable elements (TEs) in VXN-treated HT29 cells (10 μM, 48 h, n=2 biological replicates, 1 independent RNA-seq experiment) (vs. DMSO), sh*SLC6A3* HCT116 cells (vs. shCTRL, n=3 biological replicates, 2 independent RNA-seq experiments), as well as in t-hESCs treated with VXN (10 μM) or BIX-01294 (1 μM) vs. respective DMSO controls (48 h, n=2 biological replicates, 1 independent RNA-seq experiment, $p<0.05$). **b,** Distribution of significantly upregulated TEs in VXN-treated primary MC38 tumors (vs. vehicle) (upper plot, n=2 independent tumor pairs, 1 independent RNA-seq experiment) and commonly upregulated TEs in VXN-treated HT29 cells (lower plot, n=2 biological replicates, 1 independent RNA-seq experiment) across different classes of TEs. **c,** qPCR analysis of the type-1 interferon response genes IFIT1, ISG15, MX1, IFI27, and OAS3 in HT29 cells treated with VXN (10 μM) and/or reverse transcriptase inhibitors (RTi: zidovudine and nevirapine: 20 μM) vs. DMSO (48 h, n=3 biological replicates from 3 independent experiments, mean values +/- SEM, One-way ANOVA with Tukey's multiple comparisons test). **d,** GSEA indicating a significant enrichment of cytotoxic T cell and junction/adhesion gene signatures in the CRC tumor transcriptional response to *in vivo* VXN treatments vs. vehicle (n=2 independent tumor pairs, 1 independent RNA-seq experiment). Dashed lines indicate a +/- 1.3 NES cut-off (Exact p-values available in Source Data). **e,** Heat map representing the expression of individual genes from the KEGG_Natural_Killer _mediated_Cytotoxicity gene set in independent pairs of VXN-treated and vehicle control CRC tumors (n=2 independent tumor pairs, 1 independent RNA-seq experiment, z-score of FPKM values). **f,** CRC tumor growth curves of MC38-C57BL/6 and CT26-BALB/c syngeneic models treated with vehicle or VXN (25 mg/kg, 10 days) and exposed to *in vivo* injections of either anti-PD-L1 (100 μg, from day 14 to day 17) or a matched control isotype antibody. Data points represent mean +/- SEM. Statistical significance was calculated by unpaired two-tailed t-test from relative tumor size at day 10 (vs. day 0). Number of tumors measured for each condition (n) and p-values are indicated on graphs (Data from 2 independent experiments). **g,** High-content imaging analysis of CD8 immunofluorescence staining on MC38 and CT26 tumors treated with VXN/anti-PD-L1, saline/anti-PD-L1, VXN/control isotype, and saline/control isotype. The percentage of CD8-positive cells is presented for each model/condition (MC38-C57BL/6: Vehicle/control isotype: n=15 tumors, Vehicle/anti-PD-L1: n=14 tumors, VXN/control isotype: n=12 tumors, VXN/anti-PD-L1: n=12 tumors. CT26-BALB/c: Vehicle/control isotype: n=16 tumors, Vehicle/anti-PD-L1: n=16 tumors, VXN/control isotype: n=19 tumors, VXN/anti-PD-L1: n=12 tumors). Data from 2 independent experiments, p-values are indicated on graphs, mean values +/- SEM, one-way ANOVA with Holm-Sidak's multiple comparisons test. **h,** Representative fluorescence scans of whole tumor cross-sections descriped in **g**, showing CD8-positive and negative cells in MC38 and CT26 tumors treated with saline/control isotype, saline/anti-PD-L1, VXN/control isotype, and VXN/anti-PD-L1 (scale bar: 6 mm). See also Extended Data Fig. 10 and Supplementary Tables 5, 10-11.

REFERENCES

1 Waldman, A. D., Fritz, J. M. & Lenardo, M. J. A guide to cancer immunotherapy: from T cell basic science to clinical practice. *Nat Rev Immunol* **20**, 651-668 (2020). https://doi.org/10.1038/s41577-020-0306-5

2 Darvin, P., Toor, S. M., Sasidharan Nair, V. & Elkord, E. Immune checkpoint inhibitors: recent progress and potential biomarkers. *Exp Mol Med* **50**, 1-11 (2018). https://doi.org/10.1038/s12276-018-0191-1

3 Le, D. T. *et al.* Mismatch repair deficiency predicts response of solid tumors to PD-1 blockade. *Science* **357**, 409-413 (2017). https://doi.org/10.1126/science.aan6733

4 Ciardiello, D. *et al.* Immunotherapy of colorectal cancer: Challenges for therapeutic efficacy. *Cancer Treat Rev* **76**, 22-32 (2019). https://doi.org/10.1016/j.ctrv.2019.04.003

5 Brenner, H., Kloor, M. & Pox, C. P. Colorectal cancer. *Lancet* **383**, 1490-1502 (2014). https://doi.org/10.1016/S0140-6736(13)61649-9

6 Cho, Y. H. *et al.* 5-FU promotes stemness of colorectal cancer via p53-mediated WNT/β-catenin pathway activation. *Nat Commun* **11**, 5321 (2020). https://doi.org/10.1038/s41467-020-19173-2

7 Kreso, A. & Dick, J. E. Evolution of the cancer stem cell model. *Cell Stem Cell* **14**, 275-291 (2014). https://doi.org/10.1016/j.stem.2014.02.006

8 O'Brien, C. A., Pollett, A., Gallinger, S. & Dick, J. E. A human colon cancer cell capable of initiating tumour growth in immunodeficient mice. *Nature* **445**, 106-110 (2007). https://doi.org/nature05372 [pii]10.1038/nature05372

9 Bayik, D. & Lathia, J. D. Cancer stem cell-immune cell crosstalk in tumour progression. *Nat Rev Cancer* **21**, 526-536 (2021). https://doi.org/10.1038/s41568-021-00366-w

10 Miranda, A. *et al.* Cancer stemness, intratumoral heterogeneity, and immune response across cancers. *Proc Natl Acad Sci U S A* **116**, 9020-9029 (2019). https://doi.org/10.1073/pnas.1818210116

11 Ben-Porath, I. *et al.* An embryonic stem cell-like gene expression signature in poorly differentiated aggressive human tumors. *Nat Genet* **40**, 499-507 (2008). https://doi.org/10.1038/ng.127

12 Malta, T. M. *et al.* Machine Learning Identifies Stemness Features Associated with Oncogenic Dedifferentiation. *Cell* **173**, 338-354.e315 (2018). https://doi.org/10.1016/j.cell.2018.03.034

13 Bergin, C. J. *et al.* G9a controls pluripotent-like identity and tumor-initiating function in human colorectal cancer. *Oncogene* **40**, 1191-1202 (2021). https://doi.org/10.1038/s41388-020-01591-7

14 Lima-Fernandes, E. *et al.* Targeting bivalency de-represses Indian Hedgehog and inhibits self-renewal of colorectal cancer-initiating cells. *Nat Commun* **10**, 1436 (2019). https://doi.org/10.1038/s41467-019-09309-4

15 Wainwright, E. N. & Scaffidi, P. Epigenetics and Cancer Stem Cells: Unleashing, Hijacking, and Restricting Cellular Plasticity. *Trends Cancer* **3**, 372-386 (2017). https://doi.org/10.1016/j.trecan.2017.04.004
16 Werbowetski-Ogilvie, T. E. *et al.* Characterization of human embryonic stem cells with features of neoplastic progression. *Nat Biotechnol* **27**, 91-97 (2009). https://doi.org/10.1038/nbt.1516
17 Sachlos, E. *et al.* Identification of drugs including a dopamine receptor antagonist that selectively target cancer stem cells. *Cell* **149**, 1284-1297 (2012). https://doi.org/10.1016/j.cell.2012.03.049
18 Benoit, Y. D. *et al.* Targeting SUMOylation dependency in human cancer stem cells through a unique SAE2 motif revealed by chemical genomics. *Cell Chem Biol* (2021). https://doi.org/10.1016/j.chembiol.2021.04.014
19 Benoit, Y. D. *et al.* Sam68 Allows Selective Targeting of Human Cancer Stem Cells. *Cell Chem Biol* **24**, 833-844.e839 (2017). https://doi.org/10.1016/j.chembiol.2017.05.026
20 Kato, S. *et al.* Gain-of-function genetic alterations of G9a drive oncogenesis. *Cancer Discov* (2020). https://doi.org/10.1158/2159-8290.CD-19-0532
21 de Sousa e Melo, F. *et al.* A distinct role for Lgr5(+) stem cells in primary and metastatic colon cancer. *Nature* **543**, 676-680 (2017). https://doi.org/10.1038/nature21713
22 Kreso, A. *et al.* Self-renewal as a therapeutic target in human colorectal cancer. *Nat Med* **20**, 29-36 (2014). https://doi.org/10.1038/nm.3418
23 Roulois, D. *et al.* DNA-Demethylating Agents Target Colorectal Cancer Cells by Inducing Viral Mimicry by Endogenous Transcripts. *Cell* **162**, 961-973 (2015). https://doi.org/10.1016/j.cell.2015.07.056
24 Stone, M. L. *et al.* Epigenetic therapy activates type I interferon signaling in murine ovarian cancer to reduce immunosuppression and tumor burden. *Proc Natl Acad Sci U S A* **114**, E10981-E10990 (2017). https://doi.org/10.1073/pnas.1712514114
25 Corsello, S. M. *et al.* Discovering the anti-cancer potential of non-oncology drugs by systematic viability profiling. *Nat Cancer* **1**, 235-248 (2020). https://doi.org/10.1038/s43018-019-0018-6
26 Mayr, C. *et al.* HDAC Screening Identifies the HDAC Class I Inhibitor Romidepsin as a Promising Epigenetic Drug for Biliary Tract Cancer. *Cancers (Basel)* **13** (2021). https://doi.org/10.3390/cancers13153862
27 Furumai, R. *et al.* FK228 (depsipeptide) as a natural prodrug that inhibits class I histone deacetylases. *Cancer Res* **62**, 4916-4921 (2002).
28 Cherstniakova, S. A. *et al.* Metabolism of vanoxerine, 1-[2-[bis(4-fluorophenyl)methoxy]ethyl]-4-(3-phenylpropyl)piperazine, by human cytochrome P450 enzymes. *Drug Metab Dispos* **29**, 1216-1220 (2001).
29 Sogawa, C. *et al.* Antiparkinson Drug Benztropine Suppresses Tumor Growth, Circulating Tumor Cells, and Metastasis by Acting on SLC6A3/DAT and Reducing STAT3. *Cancers (Basel)* **12** (2020). https://doi.org/10.3390/cancers12020523

30 Schmitt, K. C. *et al.* Interaction of cocaine-, benztropine-, and GBR12909-like compounds with wild-type and mutant human dopamine transporters: molecular features that differentially determine antagonist-binding properties. *J Neurochem* **107**, 928-940 (2008). https://doi.org/10.1111/j.1471-4159.2008.05667.x

31 Benoit, Y. D. *et al.* Cooperation between HNF-1alpha, Cdx2, and GATA-4 in initiating an enterocytic differentiation program in a normal human intestinal epithelial progenitor cell line. *Am J Physiol Gastrointest Liver Physiol* **298**, G504-517 (2010). https://doi.org/10.1152/ajpgi.00265.2009

32 Zhang, Y. *et al.* Synthesis and transporter binding properties of bridged piperazine analogues of 1-[2-[bis(4-fluorophenyl)methoxy]ethyl]-4-(3-phenylpropyl)piperazine (GBR 12909). *J Med Chem* **43**, 4840-4849 (2000).

33 Preti, A. New developments in the pharmacotherapy of cocaine abuse. *Addict Biol* **12**, 133-151 (2007). https://doi.org/10.1111/j.1369-1600.2007.00061.x

34 Vega-Benedetti, A. F. *et al.* Colorectal Cancer Early Detection in Stool Samples Tracing CpG Islands Methylation Alterations Affecting Gene Expression. *Int J Mol Sci* **21** (2020). https://doi.org/10.3390/ijms21124494

35 Bu, M., Farrer, M. J. & Khoshbouei, H. Dynamic control of the dopamine transporter in neurotransmission and homeostasis. *NPJ Parkinsons Dis* **7**, 22 (2021). https://doi.org/10.1038/s41531-021-00161-2

36 Lomize, A. L. *et al.* PerMM: A Web Tool and Database for Analysis of Passive Membrane Permeability and Translocation Pathways of Bioactive Molecules. *J Chem Inf Model* **59**, 3094-3099 (2019). https://doi.org/10.1021/acs.jcim.9b00225

37 Pak, K. *et al.* Limited power of dopamine transporter mRNA mapping for predicting dopamine transporter availability. *Synapse* **76**, e22226 (2022). https://doi.org/10.1002/syn.22226

38 Chan, L. N. *et al.* Signalling input from divergent pathways subverts B cell transformation. *Nature* **583**, 845-851 (2020). https://doi.org/10.1038/s41586-020-2513-4

39 Chen, C. C. L. *et al.* H3S10ph broadly marks early-replicating domains in interphase ESCs and shows reciprocal antagonism with H3K9me2. *Genome Res* **28**, 37-51 (2018). https://doi.org/10.1101/gr.224717.117

40 Maze, I. *et al.* Essential role of the histone methyltransferase G9a in cocaine-induced plasticity. *Science* **327**, 213-216 (2010). https://doi.org/10.1126/science.1179438

41 Anderson, E. M. *et al.* Knockdown of the histone di-methyltransferase G9a in nucleus accumbens shell decreases cocaine self-administration, stress-induced reinstatement, and anxiety. *Neuropsychopharmacology* **44**, 1370-1376 (2019). https://doi.org/10.1038/s41386-018-0305-4

42 Shrestha, R., Mohankumar, K., Jin, U. H., Martin, G. & Safe, S. The Histone Methyltransferase Gene G9A Is Regulated by Nuclear Receptor 4A1 in Alveolar Rhabdomyosarcoma Cells. *Mol Cancer Ther* **20**, 612-622 (2021). https://doi.org/10.1158/1535-7163.MCT-20-0474

43 Han, Y. H. *et al.* Regulation of Nur77 nuclear export by c-Jun N-terminal kinase and Akt. *Oncogene* **25**, 2974-2986 (2006). https://doi.org/10.1038/sj.onc.1209358

44 Zhan, Y. *et al.* Cytosporone B is an agonist for nuclear orphan receptor Nur77. *Nat Chem Biol* **4**, 548-556 (2008). https://doi.org/10.1038/nchembio.106

45 Herring, J. A., Elison, W. S. & Tessem, J. S. Function of Nr4a Orphan Nuclear Receptors in Proliferation, Apoptosis and Fuel Utilization Across Tissues. *Cells* **8** (2019). https://doi.org/10.3390/cells8111373

46 Luo, X. *et al.* Effects of DNA Methylation on TFs in Human Embryonic Stem Cells. *Front Genet* **12**, 639461 (2021). https://doi.org/10.3389/fgene.2021.639461

47 Bergin, C. J. & Benoit, Y. D. Protocol for serial organoid formation assay using primary colorectal cancer tissues to evaluate cancer stem cell activity. *STAR Protoc* **3**, 101218 (2022). https://doi.org/10.1016/j.xpro.2022.101218

48 Shimokawa, M. *et al.* Visualization and targeting of LGR5. *Nature* **545**, 187-192 (2017). https://doi.org/10.1038/nature22081

49 Dittrich, H. C. *et al.* COR-ART: A multicenter, randomized, double-blind, placebo-controlled dose-ranging study to evaluate single oral doses of vanoxerine for conversion of recent-onset atrial fibrillation or flutter to normal sinus rhythm. *Heart Rhythm* **12**, 1105-1112 (2015). https://doi.org/10.1016/j.hrthm.2015.02.014

50 Zhang, S. M. *et al.* KDM5B promotes immune evasion by recruiting SETDB1 to silence retroelements. *Nature* **598**, 682-687 (2021). https://doi.org/10.1038/s41586-021-03994-2

51 Larouche, J. D. *et al.* Widespread and tissue-specific expression of endogenous retroelements in human somatic tissues. *Genome Med* **12**, 40 (2020). https://doi.org/10.1186/s13073-020-00740-7

52 Kelly, G. M. *et al.* G9a Inhibition Enhances Checkpoint Inhibitor Blockade Response in Melanoma. *Clin Cancer Res* **27**, 2624-2635 (2021). https://doi.org/10.1158/1078-0432.CCR-20-3463

53 Efremova, M. *et al.* Targeting immune checkpoints potentiates immunoediting and changes the dynamics of tumor evolution. *Nat Commun* **9**, 32 (2018). https://doi.org/10.1038/s41467-017-02424-0

54 Haebe, J. R., Bergin, C. J., Sandouka, T. & Benoit, Y. D. Emerging role of G9a in cancer stemness and promises as a therapeutic target. *Oncogenesis* **10**, 76 (2021). https://doi.org/10.1038/s41389-021-00370-7

55 Boland, P. M. & Ma, W. W. Immunotherapy for Colorectal Cancer. *Cancers (Basel)* **9** (2017). https://doi.org/10.3390/cancers9050050

56 Jain, V., Bose, S., Arya, A. K. & Arif, T. Lysosomes in Stem Cell Quiescence: A Potential Therapeutic Target in Acute Myeloid Leukemia. *Cancers (Basel)* **14** (2022). https://doi.org/10.3390/cancers14071618

57 Fraser, K. B. *et al.* LRRK2 secretion in exosomes is regulated by 14-3-3. *Hum Mol Genet* **22**, 4988-5000 (2013). https://doi.org/10.1093/hmg/ddt346

58 Perez-Hernandez, D. *et al.* The intracellular interactome of tetraspanin-enriched microdomains reveals their function as sorting machineries toward exosomes. *J Biol Chem* **288**, 11649-11661 (2013). https://doi.org/10.1074/jbc.M112.445304

59 Kadric, S., Mohler, H., Kallioniemi, O. & Altmann, K. H. A Multicenter, Randomized, Placebo-Controlled Study to Evaluate the Efficacy and Safety of Long-Acting Injectable Formulation of Vanoxerine (Vanoxerine Consta 394.2 mg) for Cocaine Relapse Prevention. *World Journal of Neuroscience* **9**, 113-137 (2019). https://doi.org/10.4236/WJNS.2019.93008

60 Sanvisens, A. *et al.* Long-Term Outcomes of Patients With Cocaine Use Disorder: A 18-years Addiction Cohort Study. *Front Pharmacol* **12**, 625610 (2021). https://doi.org/10.3389/fphar.2021.625610

Bergin et al. Figure 1

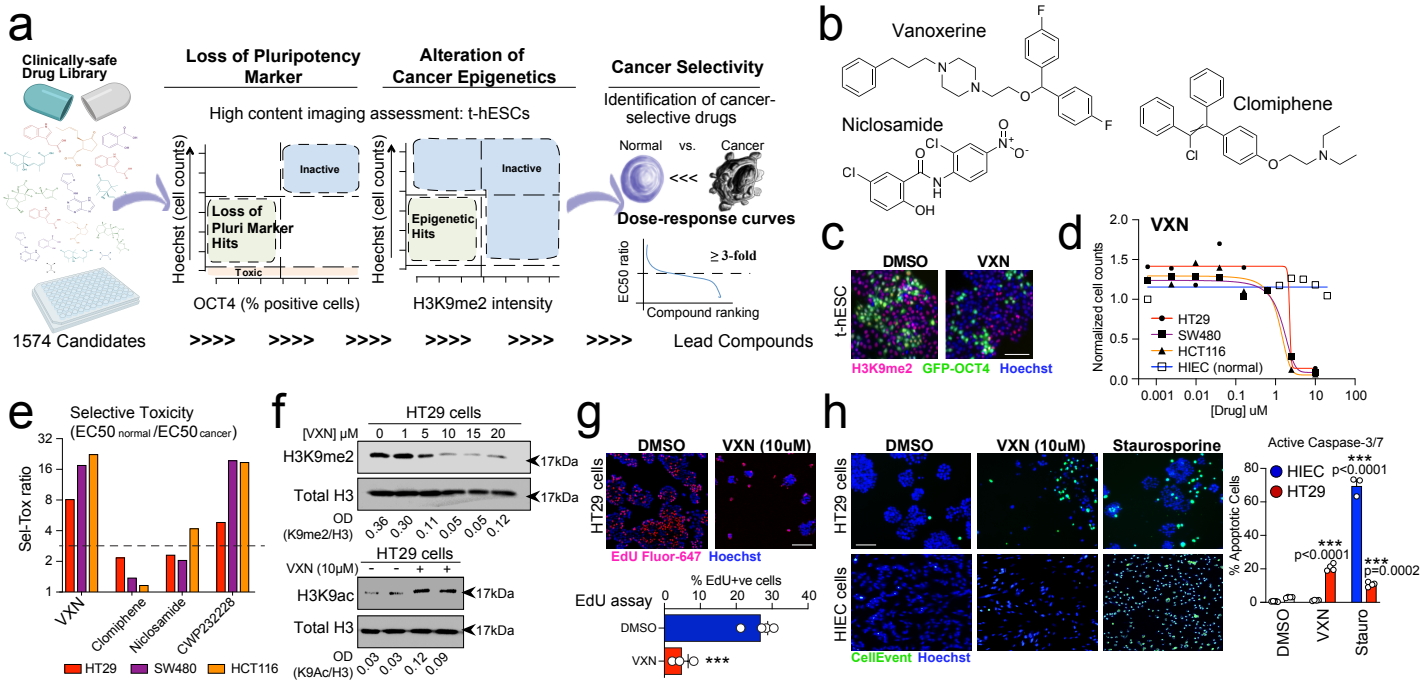

Bergin et al. Figure 2

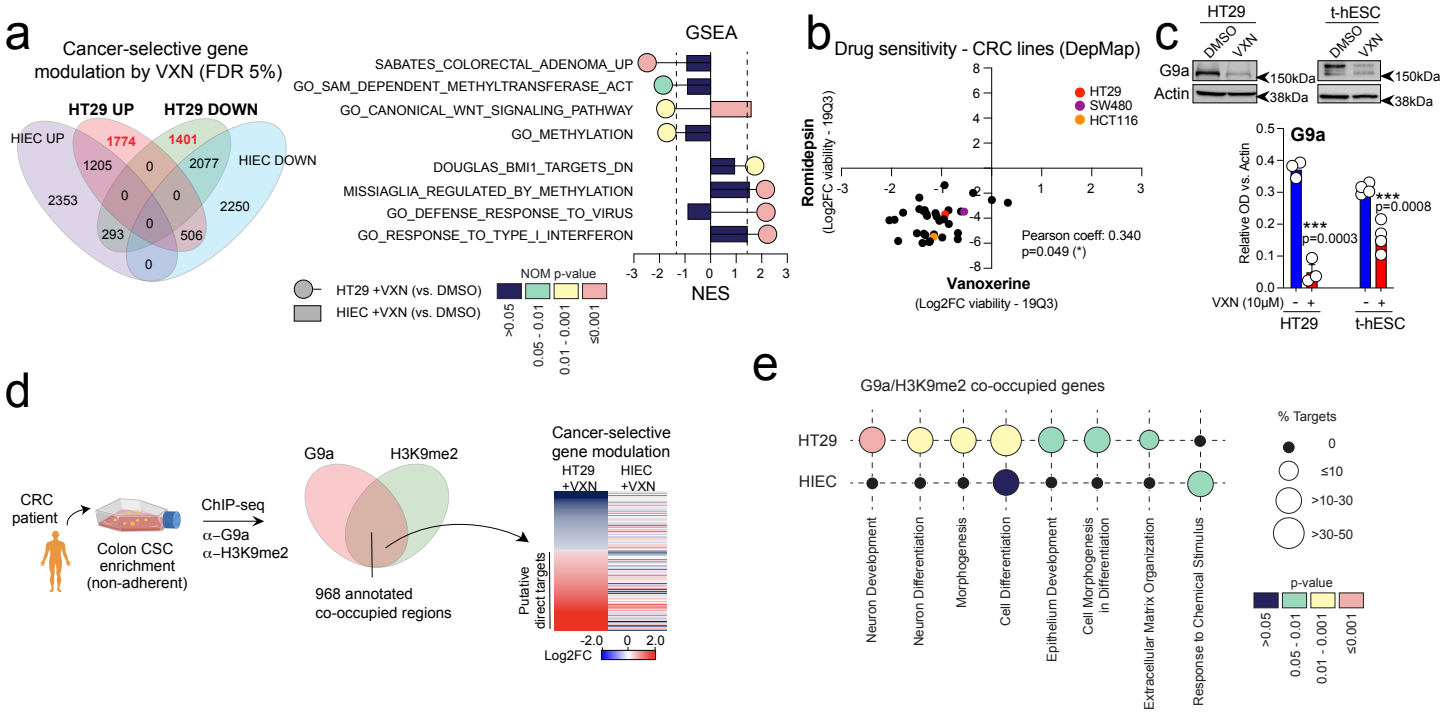

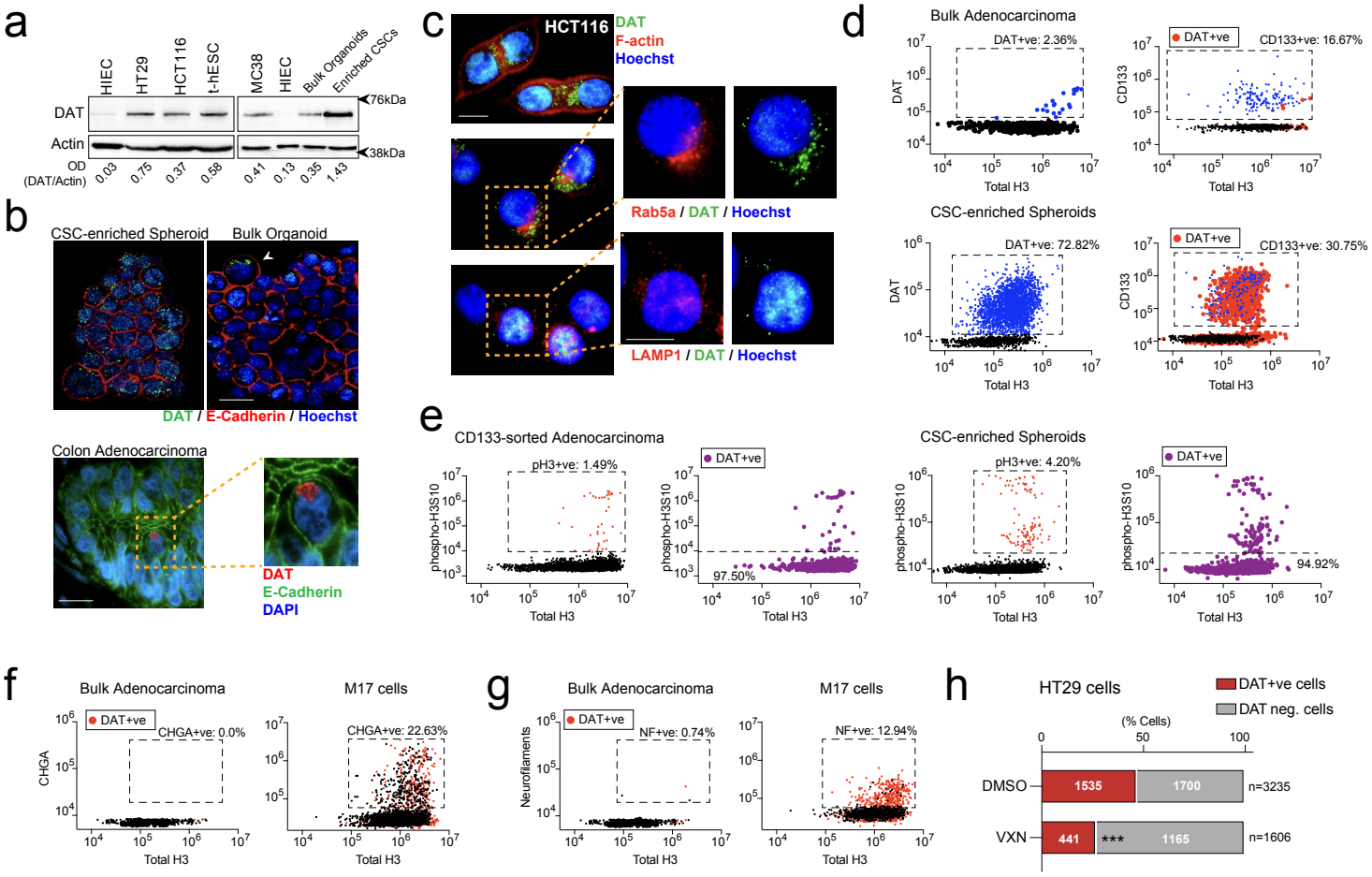
a
HIEC
HT29
HCT116
t-hESC
MC38
HIEC
Bulk Organoids
Enriched CSCs
DAT
Actin
76kDa
38kDa
OD (DAT/Actin)
0.03
0.75
0.37
0.58
0.41
0.13
0.35
1.43
b
CSC-enriched Spheroid
Bulk Organoid
DAT / E-Cadherin / Hoechst
Colon Adenocarcinoma
DAT
E-Cadherin
DAPI
c
HCT116
DAT
F-actin
Hoechst
Rab5a / DAT / Hoechst
LAMP1 / DAT / Hoechst
d
Bulk Adenocarcinoma
DAT+ve: 2.36%
DAT+ve
CD133+ve: 16.67%
CSC-enriched Spheroids
DAT+ve: 72.82%
DAT+ve
CD133+ve: 30.75%
Total H3
e
CD133-sorted Adenocarcinoma
pH3+ve: 1.49%
DAT+ve
97.50%
CSC-enriched Spheroids
pH3+ve: 4.20%
DAT+ve
94.92%
phospho-H3S10
Total H3
f
Bulk Adenocarcinoma
M17 cells
DAT+ve
CHGA+ve: 0.0%
CHGA+ve: 22.63%
CHGA
Total H3
g
Bulk Adenocarcinoma
M17 cells
DAT+ve
NF+ve: 0.74%
NF+ve: 12.94%
Neurofilaments
Total H3
h
HT29 cells
DAT+ve cells
DAT neg. cells
(% Cells)
0
50
100
DMSO
1535
1700
n=3235
VXN
441
***
1165
n=1606

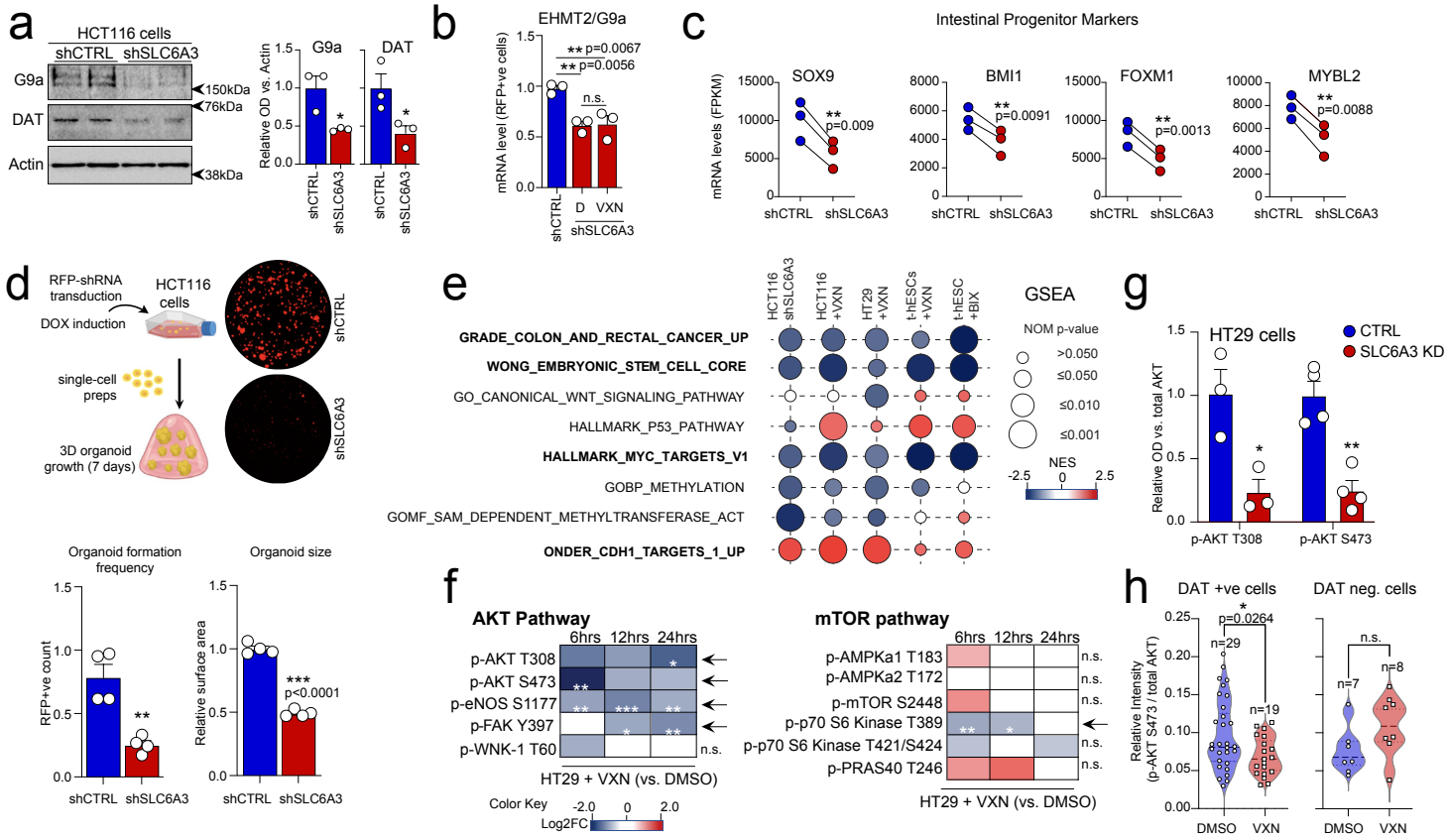
a
HCT116 cells
shCTRL shSLC6A3
G9a
DAT
Actin
150kDa
76kDa
38kDa
Relative OD vs. Actin
G9a
DAT
shCTRL shSLC6A3
b
EHMT2/G9a
mRNA level (RFP+ve cells)
** p=0.0067
** p=0.0056
n.s.
shCTRL D VXN
shSLC6A3
c
Intestinal Progenitor Markers
mRNA levels (FPKM)
SOX9
** p=0.009
BMI1
** p=0.0091
FOXM1
** p=0.0013
MYBL2
** p=0.0088
shCTRL shSLC6A3
d
RFP-shRNA transduction
HCT116 cells
DOX induction
single-cell preps
3D organoid growth (7 days)
shCTRL
shSLC6A3
Organoid formation frequency
RFP+ve count
Organoid size
Relative surface area
*** p<0.0001
e
GSEA
HCT116 shSLC6A3
HCT116 +VXN
HT29 +VXN
t-hESCs +VXN
t-hESC +BIX
GRADE_COLON_AND_RECTAL_CANCER_UP
WONG_EMBRYONIC_STEM_CELL_CORE
GO_CANONICAL_WNT_SIGNALING_PATHWAY
HALLMARK_P53_PATHWAY
HALLMARK_MYC_TARGETS_V1
GOBP_METHYLATION
GOMF_SAM_DEPENDENT_METHYLTRANSFERASE_ACT
ONDER_CDH1_TARGETS_1_UP
NOM p-value
>0.050
≤0.050
≤0.010
≤0.001
NES
f
AKT Pathway
6hrs 12hrs 24hrs
p-AKT T308
p-AKT S473
p-eNOS S1177
p-FAK Y397
p-WNK-1 T60
n.s.
HT29 + VXN (vs. DMSO)
Color Key
Log2FC
mTOR pathway
p-AMPKa1 T183
p-AMPKa2 T172
p-mTOR S2448
p-p70 S6 Kinase T389
p-p70 S6 Kinase T421/S424
p-PRAS40 T246
g
HT29 cells
CTRL
SLC6A3 KD
Relative OD vs. total AKT
p-AKT T308
p-AKT S473
h
DAT +ve cells
DAT neg. cells
Relative Intensity (p-AKT S473 / total AKT)
p=0.0264
n=29
n=19
n=7
n=8
n.s.
DMSO VXN

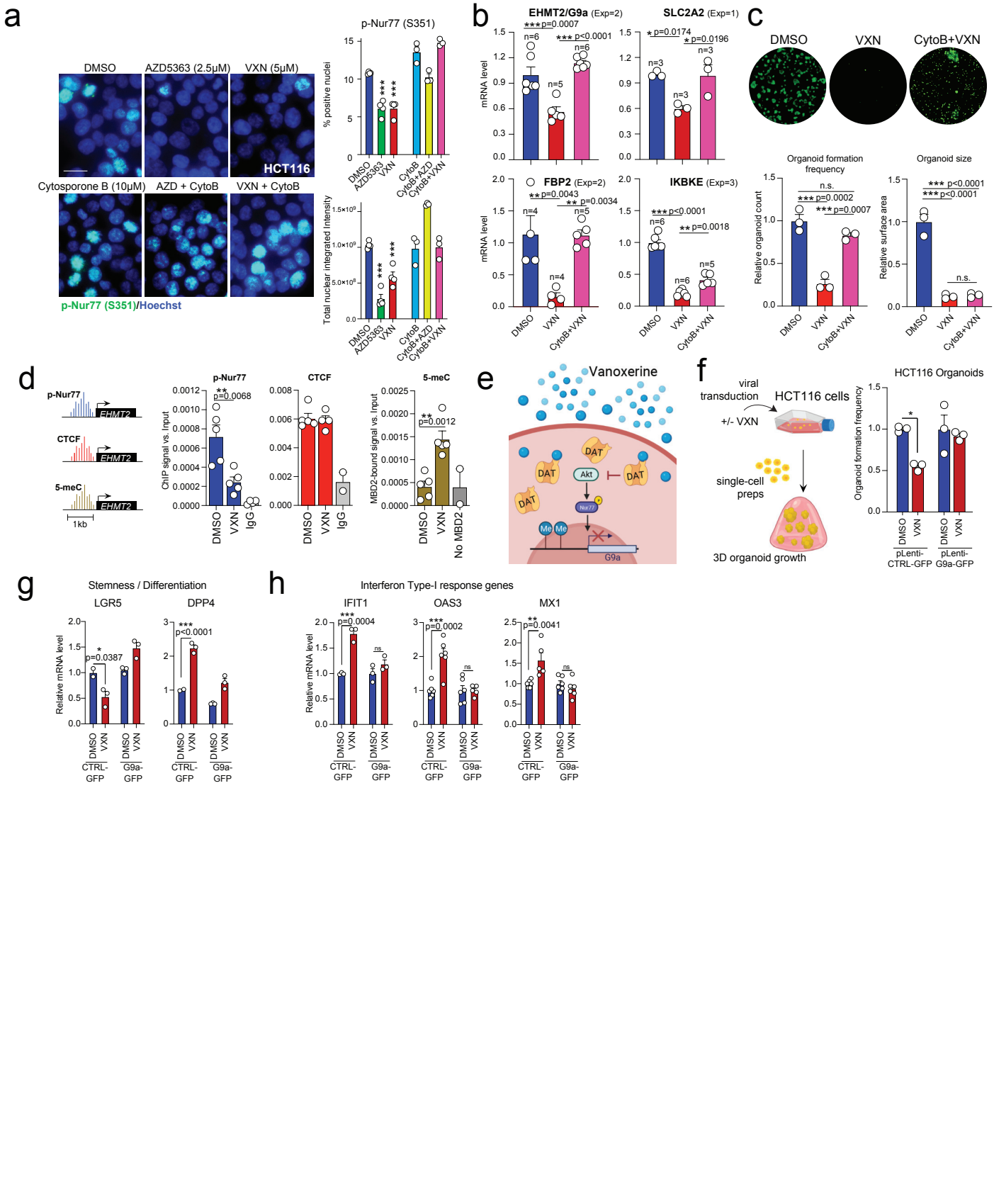
a
DMSO
AZD5363 (2.5μM)
VXN (5μM)
HCT116
Cytosporone B (10μM)
AZD + CytoB
VXN + CytoB
p-Nur77 (S351)/Hoechst
p-Nur77 (S351)
% positive nuclei
Total nuclear integrated Intensity
DMSO
AZD5363
VXN
CytoB
CytoB+AZD
CytoB+VXN
b
EHMT2/G9a (Exp=2)
SLC2A2 (Exp=1)
FBP2 (Exp=2)
IKBKE (Exp=3)
mRNA level
c
DMSO
VXN
CytoB+VXN
Organoid formation frequency
Organoid size
Relative organoid count
Relative surface area
d
p-Nur77
CTCF
5-meC
EHMT2
1kb
ChIP signal vs. Input
MBD2-bound signal vs. Input
IgG
No MBD2
e
Vanoxerine
DAT
Akt
Me
G9a
f
viral transduction
HCT116 cells
+/- VXN
single-cell preps
3D organoid growth
HCT116 Organoids
Organoid formation frequency
pLenti-CTRL-GFP
pLenti-G9a-GFP
g
Stemness / Differentiation
LGR5
DPP4
Relative mRNA level
CTRL-GFP
G9a-GFP
h
Interferon Type-I response genes
IFIT1
OAS3
MX1

Bergin et al. Figure 6

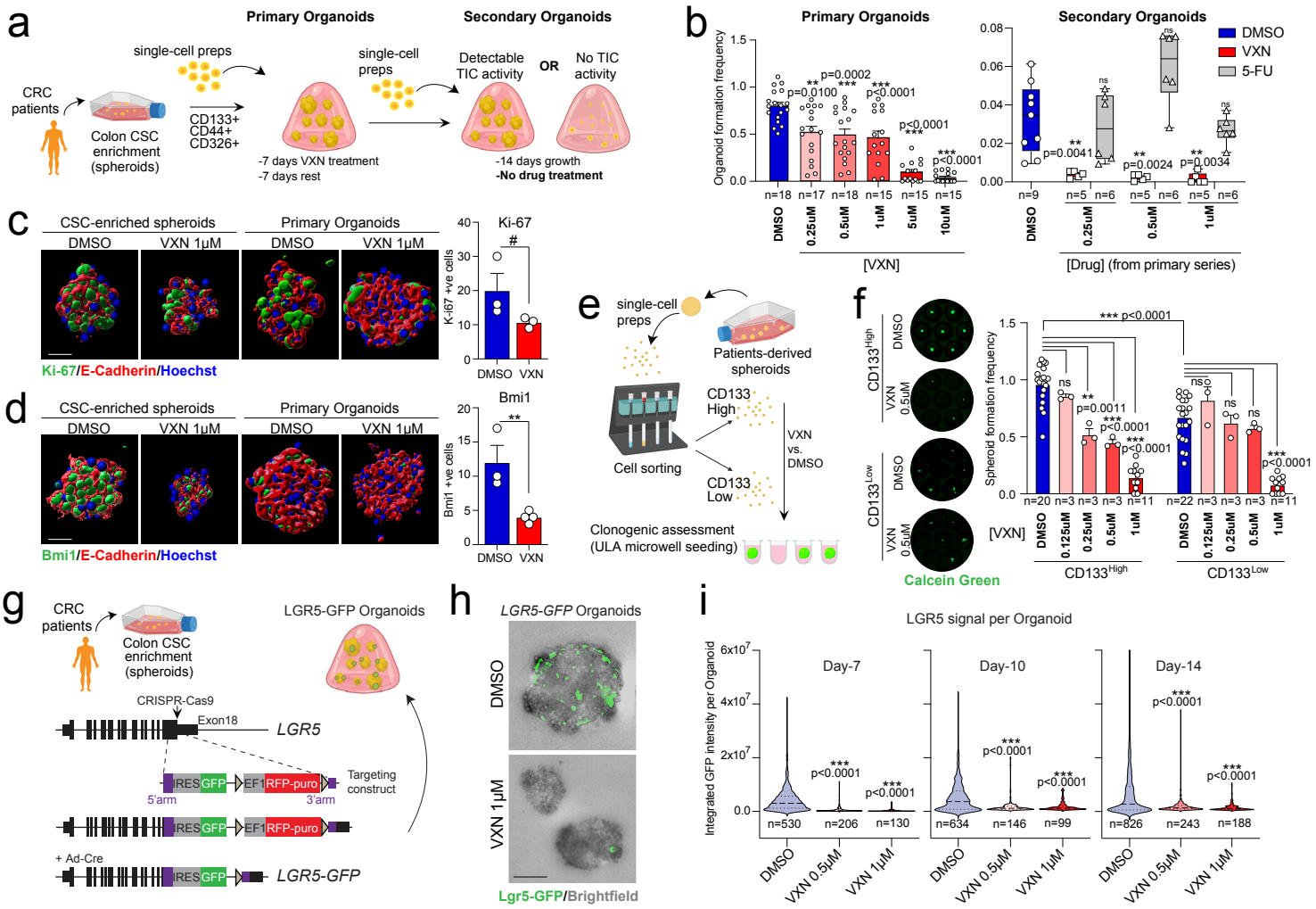

Bergin et al. Figure 7

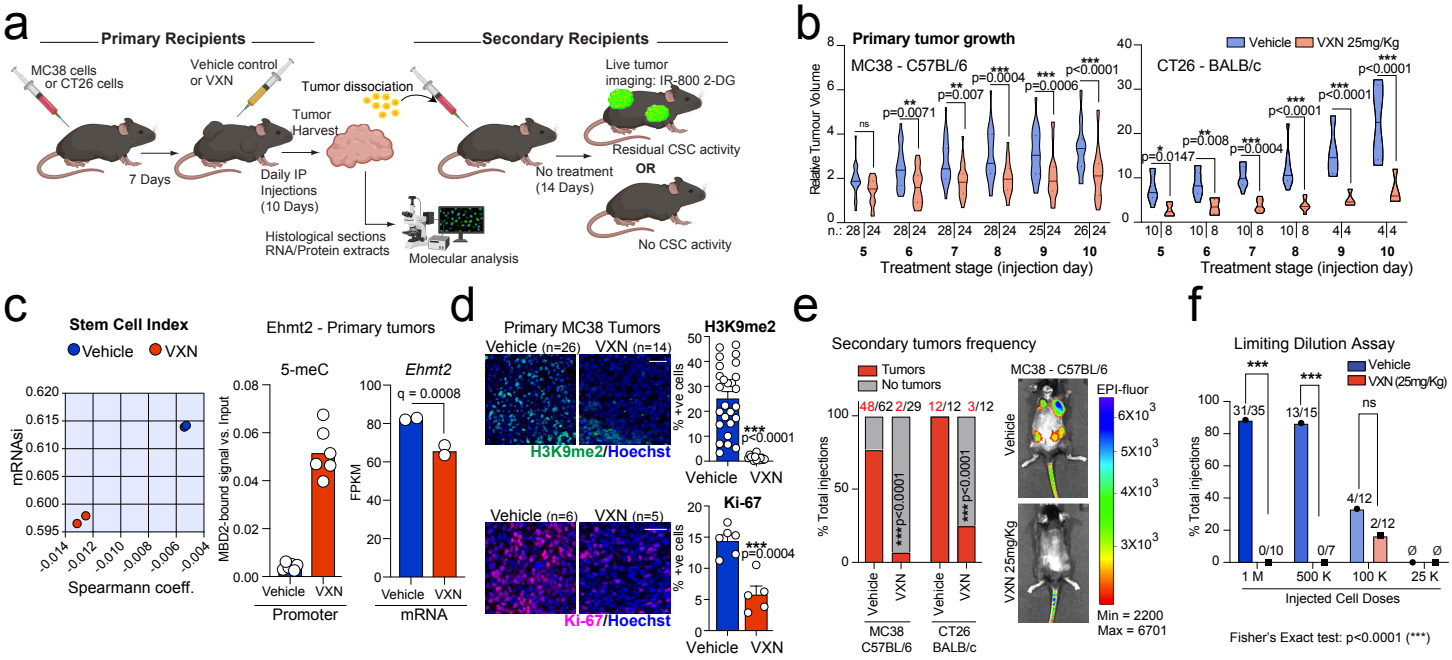

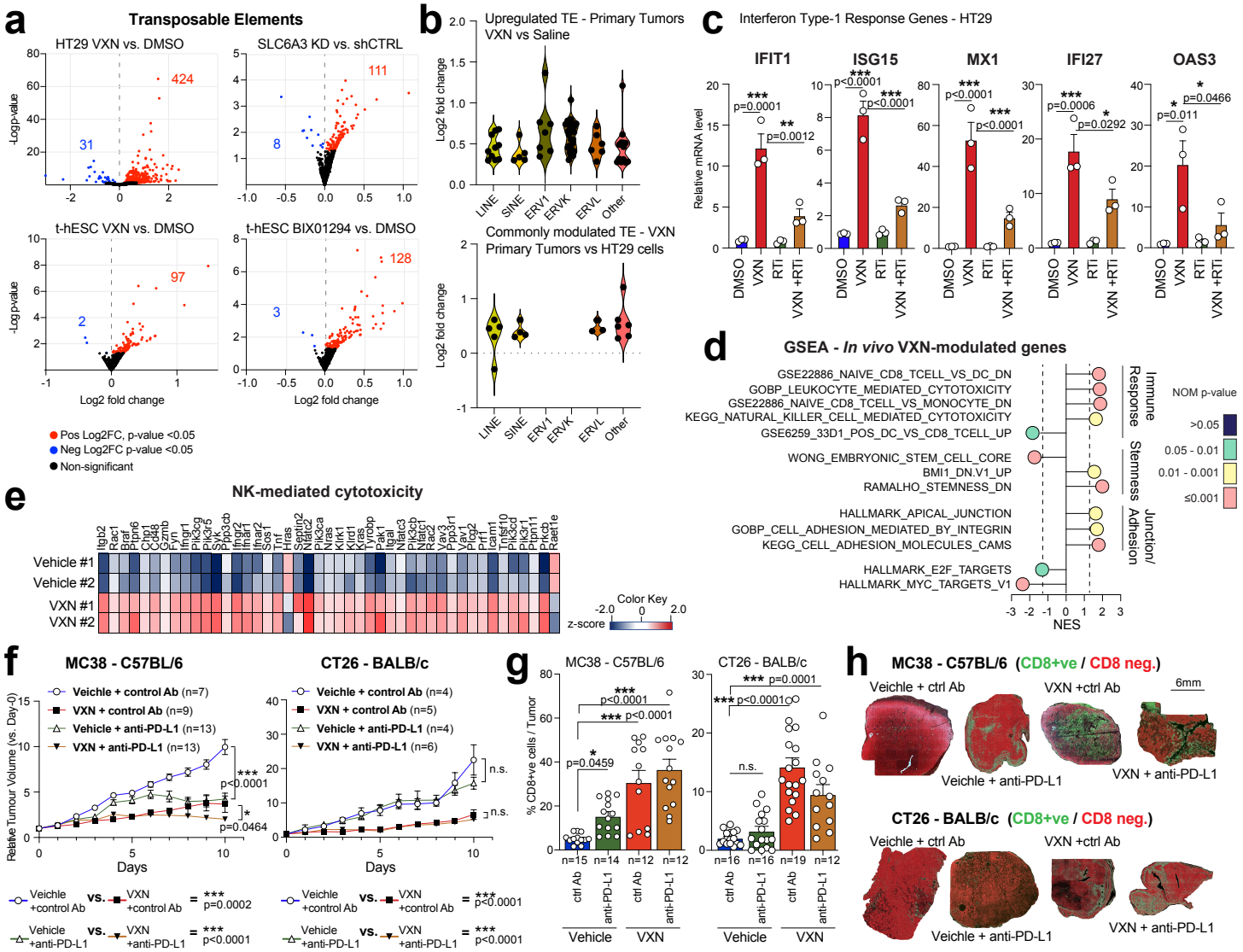
a
Transposable Elements
HT29 VXN vs. DMSO
SLC6A3 KD vs. shCTRL
t-hESC VXN vs. DMSO
t-hESC BIX01294 vs. DMSO
-Log p-value
Log2 fold change
424
31
111
8
97
2
128
3
Pos Log2FC, p-value <0.05
Neg Log2FC p-value <0.05
Non-significant
b
Upregulated TE - Primary Tumors
VXN vs Saline
Commonly modulated TE - VXN
Primary Tumors vs HT29 cells
Log2 fold change
LINE
SINE
ERV1
ERVK
ERVL
Other
c
Interferon Type-1 Response Genes - HT29
IFIT1
ISG15
MX1
IFI27
OAS3
Relative mRNA level
DMSO
VXN
RTi
VXN +RTi
d
GSEA - In vivo VXN-modulated genes
GSE22886_NAIVE_CD8_TCELL_VS_DC_DN
GOBP_LEUKOCYTE_MEDIATED_CYTOTOXICITY
GSE22886_NAIVE_CD8_TCELL_VS_MONOCYTE_DN
KEGG_NATURAL_KILLER_CELL_MEDIATED_CYTOTOXICITY
GSE6259_33D1_POS_DC_VS_CD8_TCELL_UP
WONG_EMBRYONIC_STEM_CELL_CORE
BMI1_DN.V1_UP
RAMALHO_STEMNESS_DN
HALLMARK_APICAL_JUNCTION
GOBP_CELL_ADHESION_MEDIATED_BY_INTEGRIN
KEGG_CELL_ADHESION_MOLECULES_CAMS
HALLMARK_E2F_TARGETS
HALLMARK_MYC_TARGETS_V1
Immune Response
Stemness
Junction/ Adhesion
NOM p-value
NES
e
NK-mediated cytotoxicity
Vehicle #1
Vehicle #2
VXN #1
VXN #2
Color Key
z-score
f
MC38 - C57BL/6
CT26 - BALB/c
Veichle + control Ab (n=7)
VXN + control Ab (n=9)
Vehicle + anti-PD-L1 (n=13)
VXN + anti-PD-L1 (n=13)
Veichle + control Ab (n=4)
VXN + control Ab (n=5)
Vehicle + anti-PD-L1 (n=4)
VXN + anti-PD-L1 (n=6)
Relative Tumour Volume (vs. Day-0)
Days
p=0.0002
p<0.0001
g
MC38 - C57BL/6
CT26 - BALB/c
% CD8+ve cells / Tumor
ctrl Ab
anti-PD-L1
Vehicle
VXN
h
MC38 - C57BL/6 (CD8+ve / CD8 neg.)
CT26 - BALB/c (CD8+ve / CD8 neg.)
Veichle + ctrl Ab
VXN +ctrl Ab
Veichle + anti-PD-L1
VXN + anti-PD-L1
6mm

Bergin et al. Extended Data Figure 1

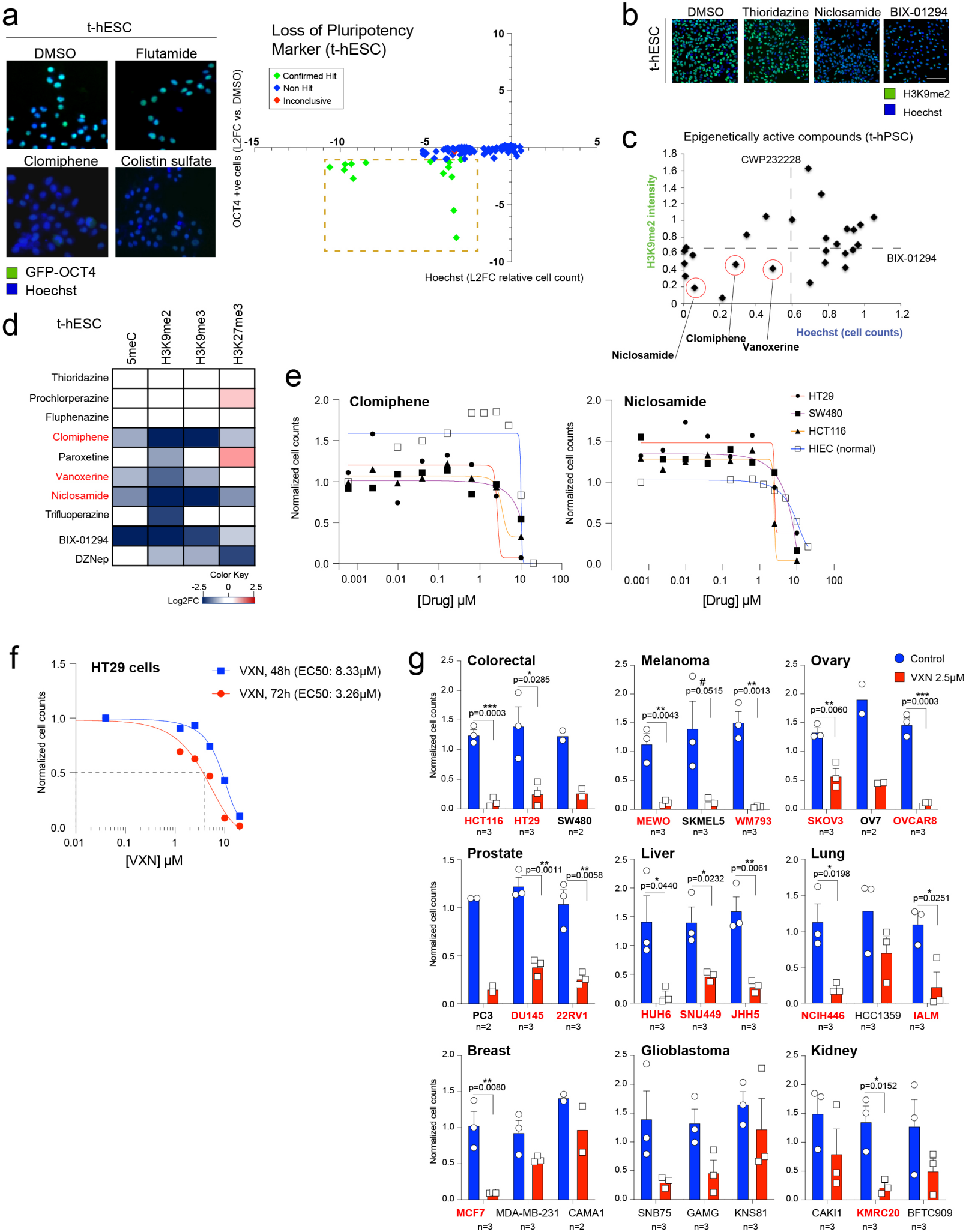

Bergin et al. Extended Data Figure 2

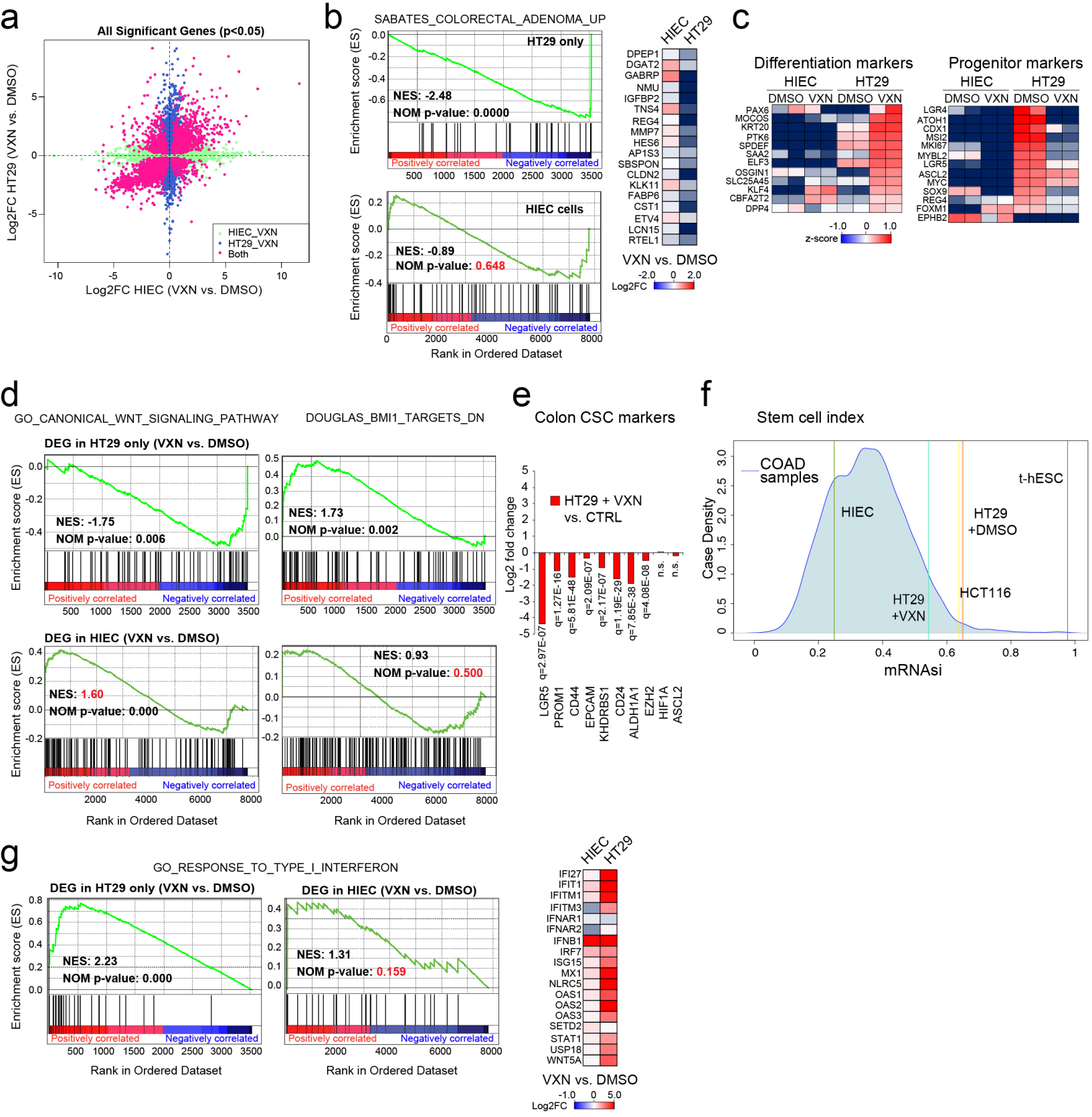

a

DepMap Drug Sensitivity (PRISM Repurposing Primary Screen- 19Q3) in colorectal cancer

Compound	Correlation (Pearson r) vs. VXN	P-value (two-tailed)	Mechanism of Action
Idarubicin	0.432	0.011	Genotoxic, Topoisomerase-II interference
IDRA-21	0.404	0.020	Positive modulator of AMPA receptor
Oprozomib	0.367	0.030	Proteasome inhibitor
Romidepsin	**0.340**	**0.049**	**Epigenetic inhibitor (HDAC, G9a, DNMTs)**
ZM-306416	0.239	0.173 (ns)	VEGF/EGFR inhibitor
Tempol	0.077	0.664 (ns)	ROS modulator

b

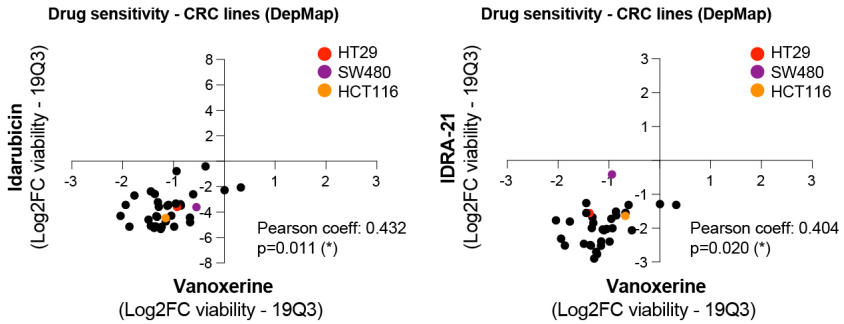

c

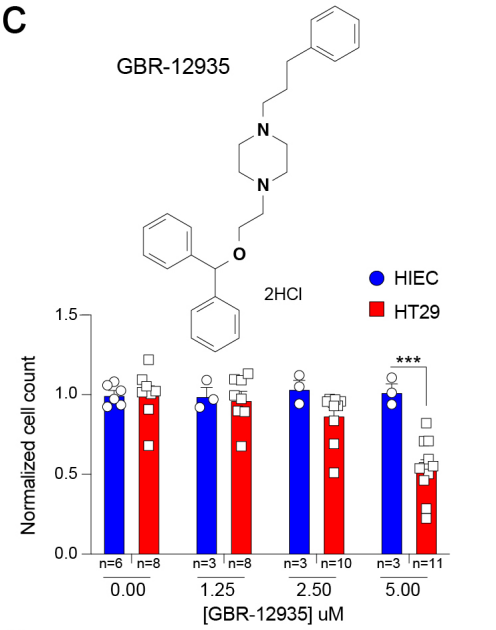

d

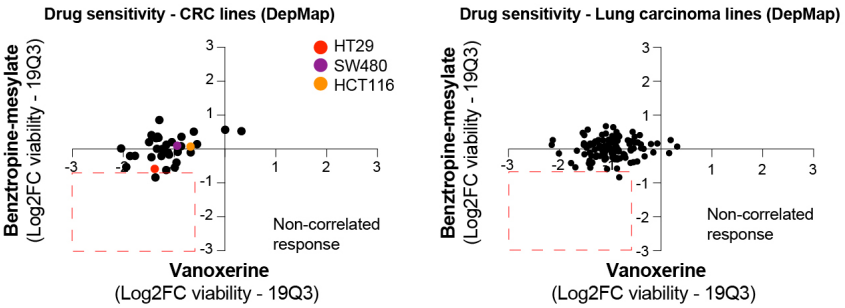

e

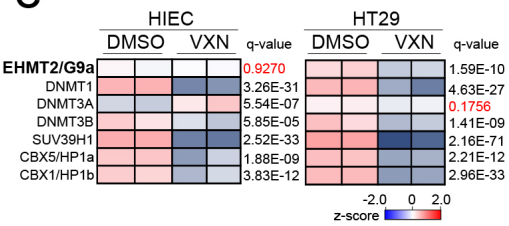

f

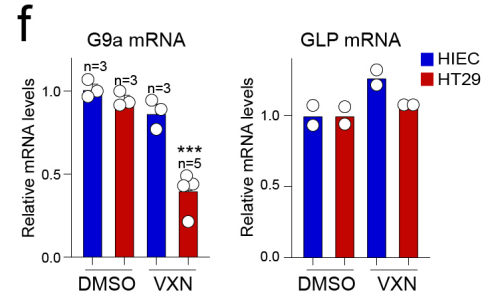

g

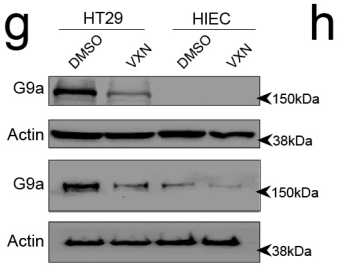

h

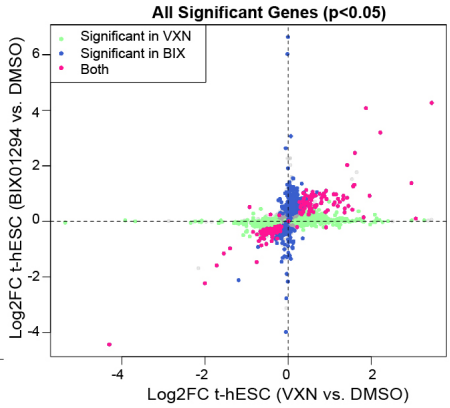

i

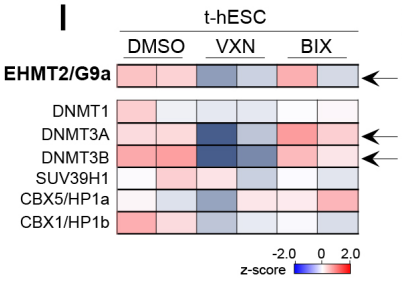

j

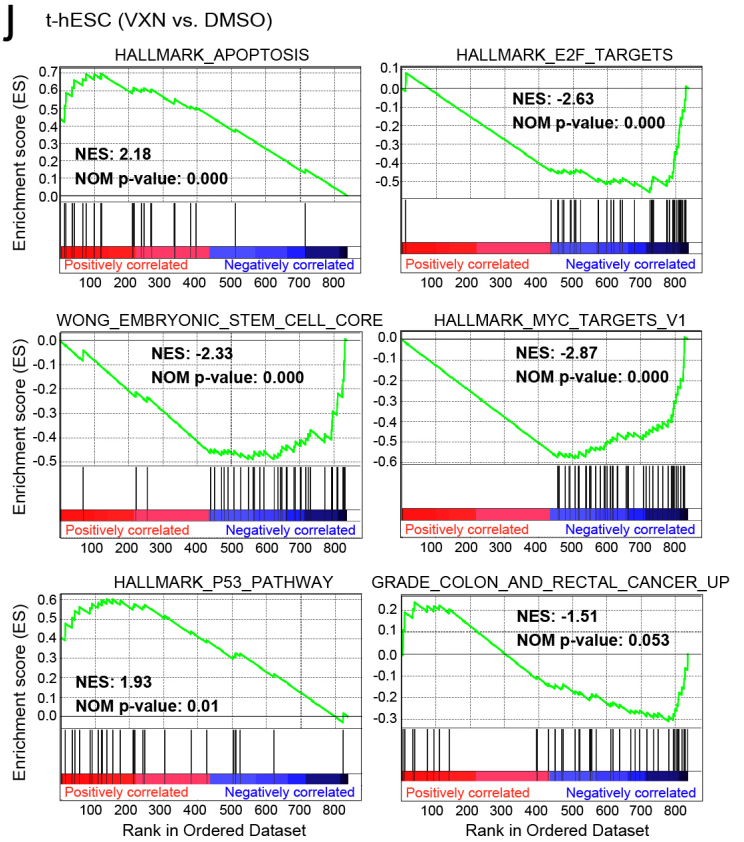

k

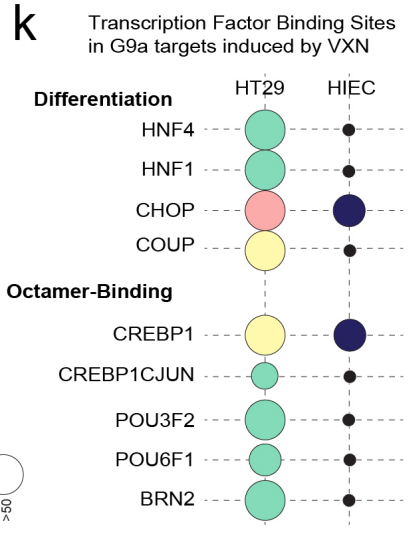

Bergin et al. Extended Data Figure 4

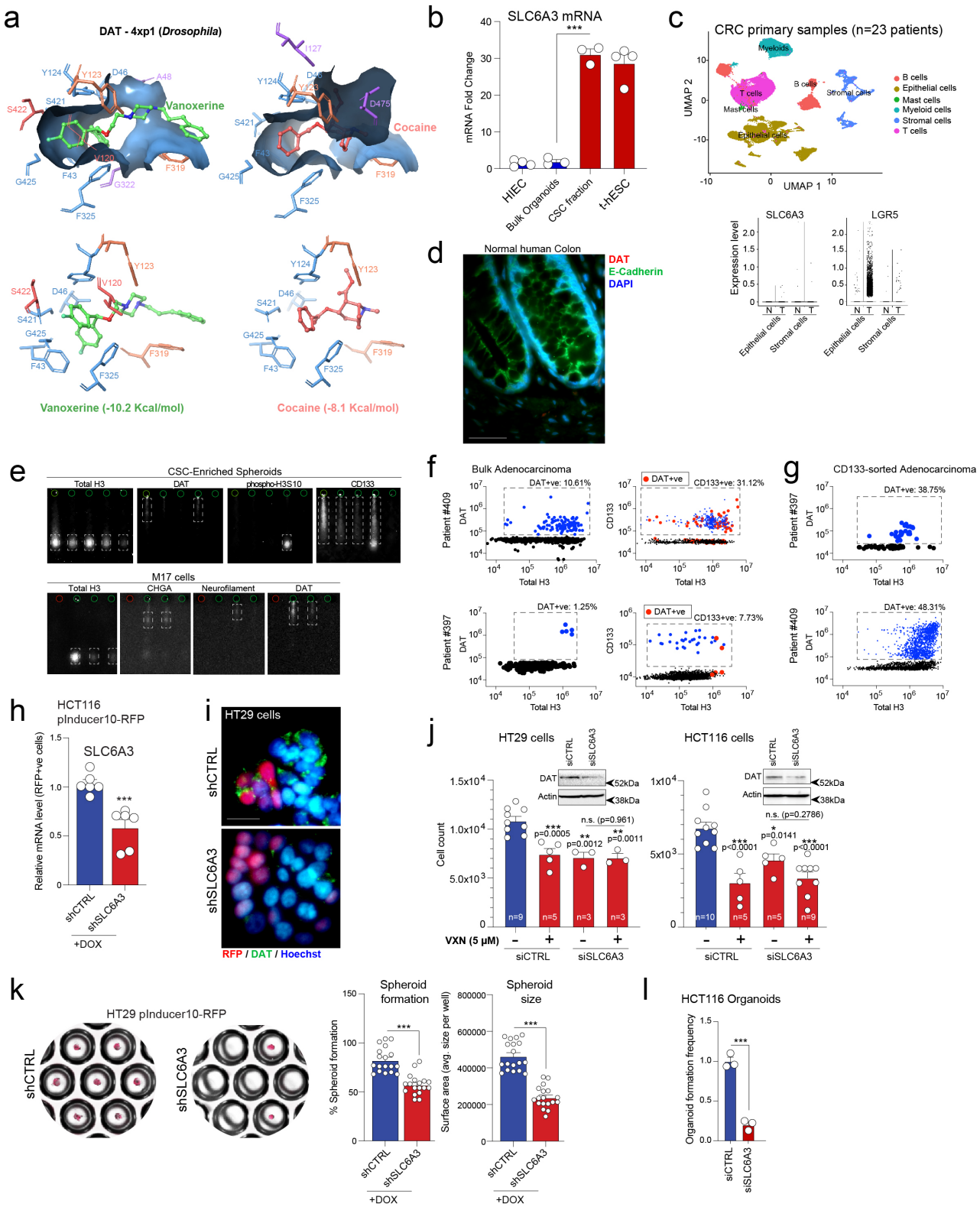

Bergin et al. Extended Data Figure 5

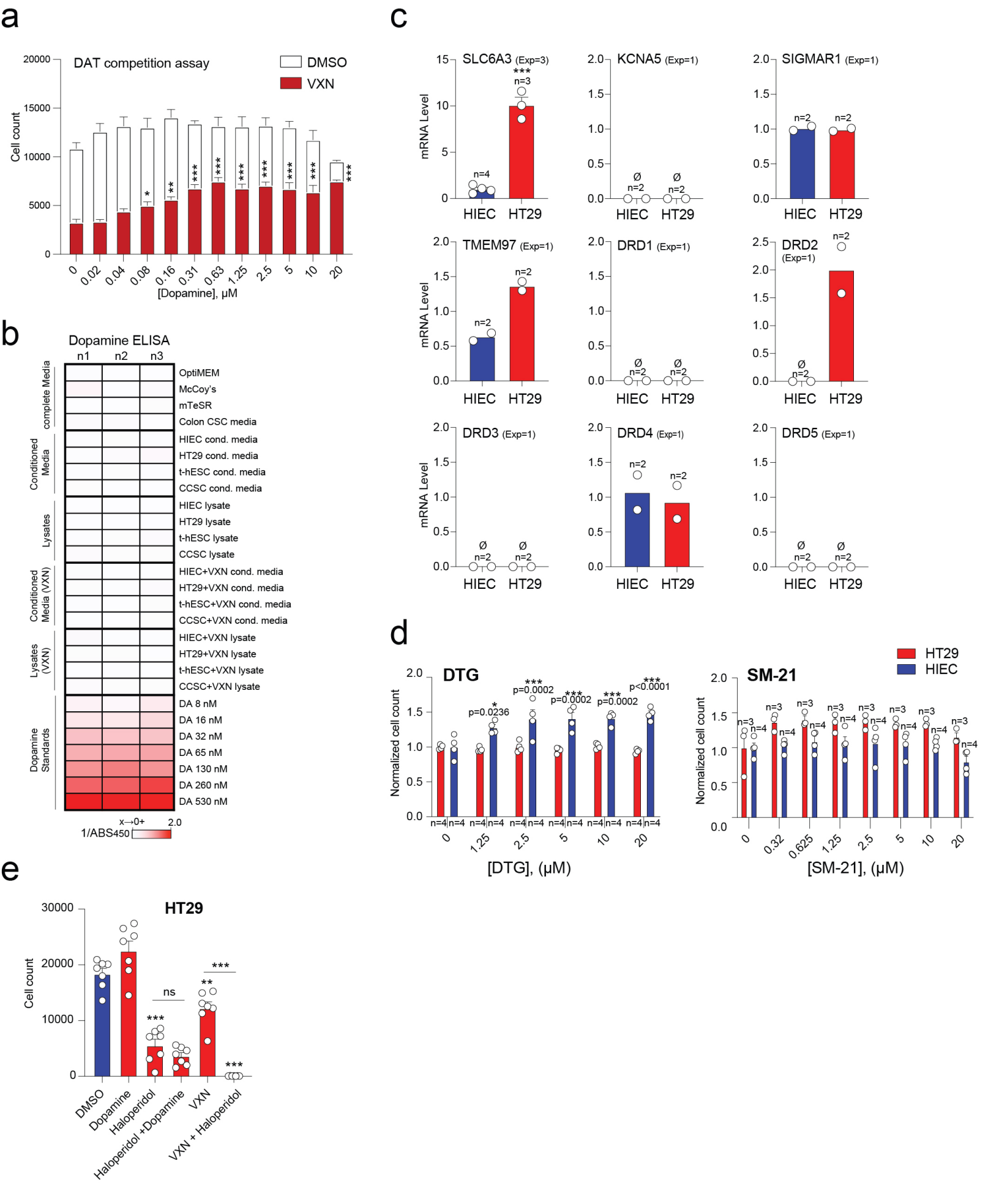

Bergin et al. Extended Data Figure 6

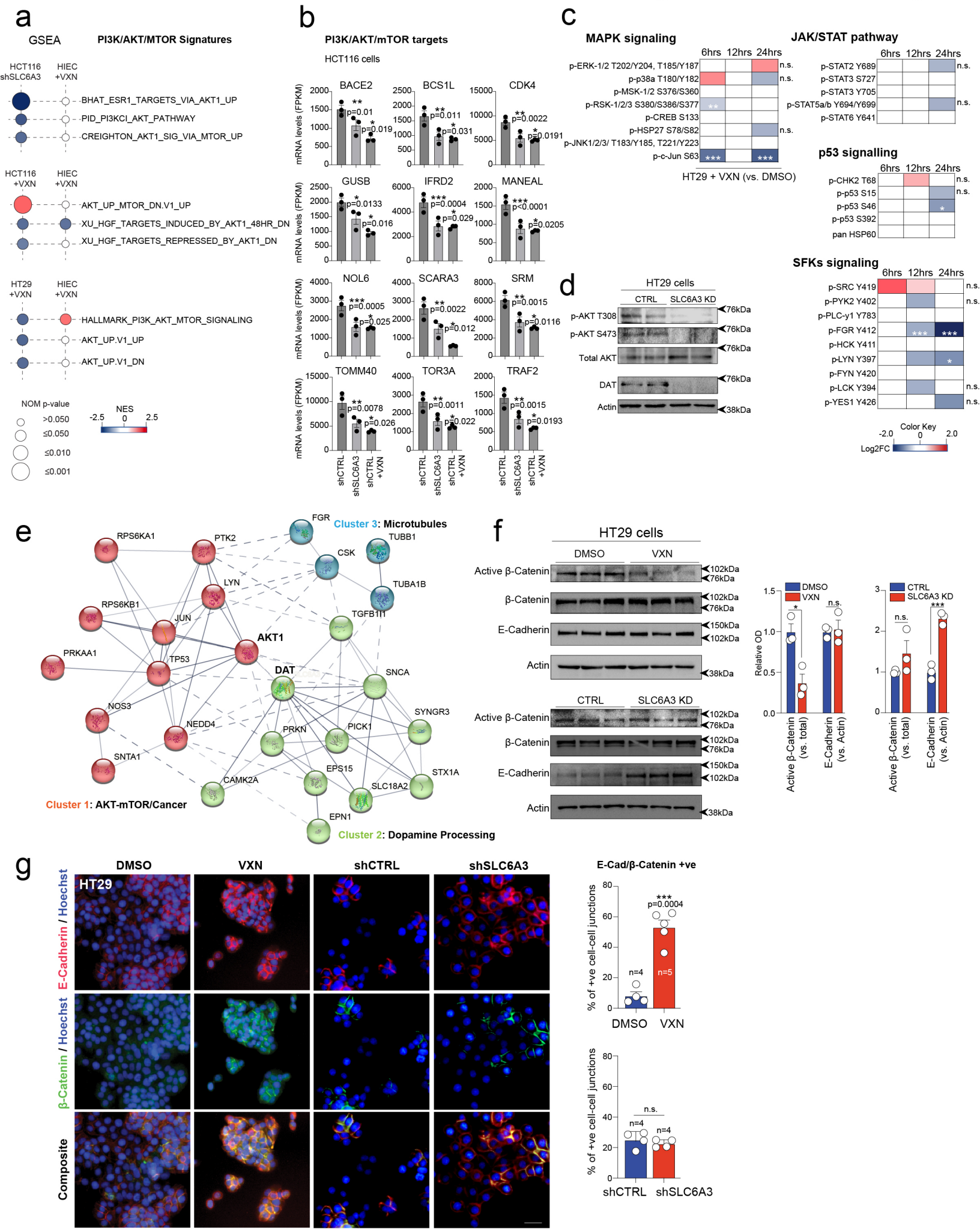

Bergin et al. Extended Data Figure 7

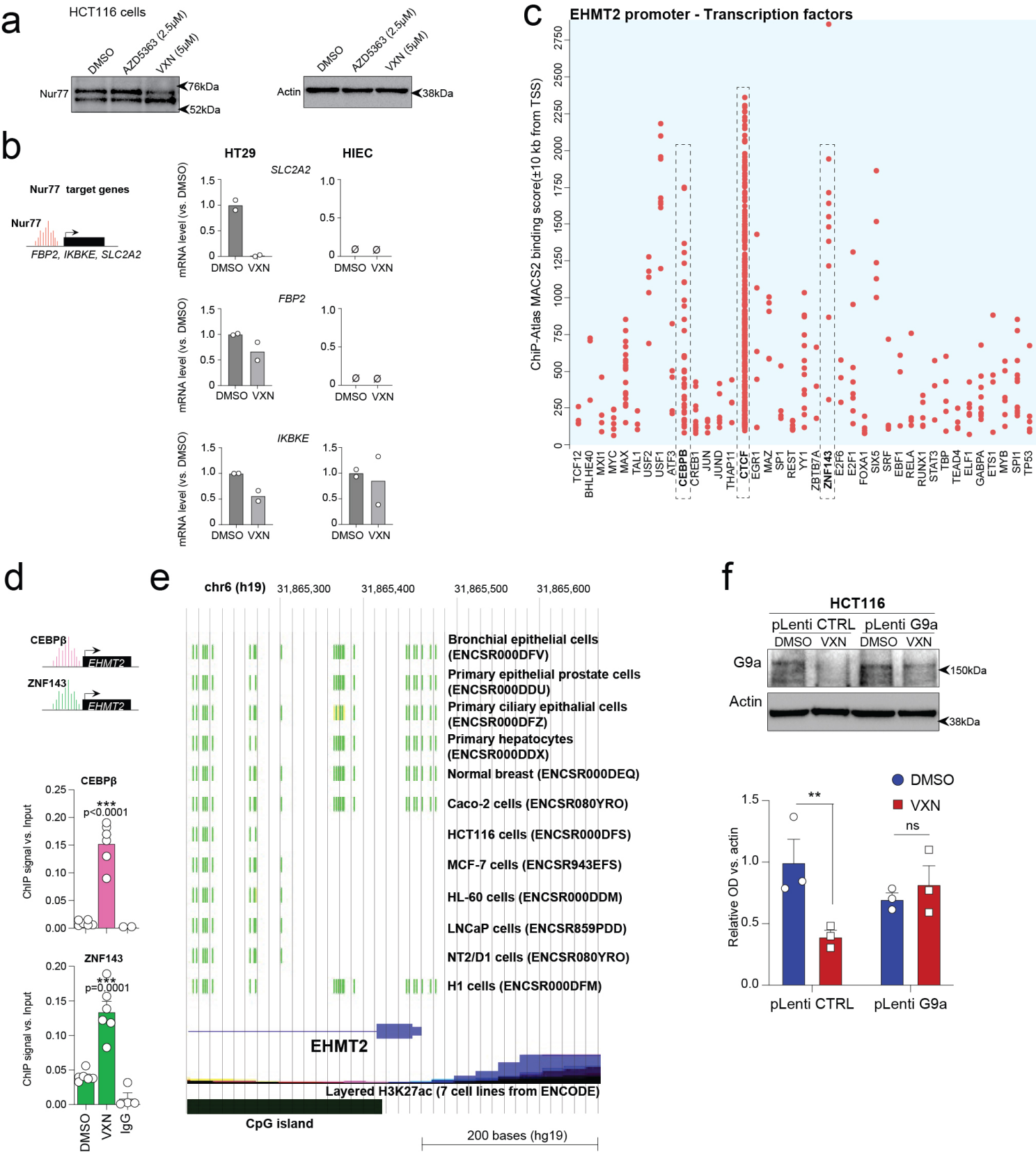

Bergin et al. Extended Data Figure 8

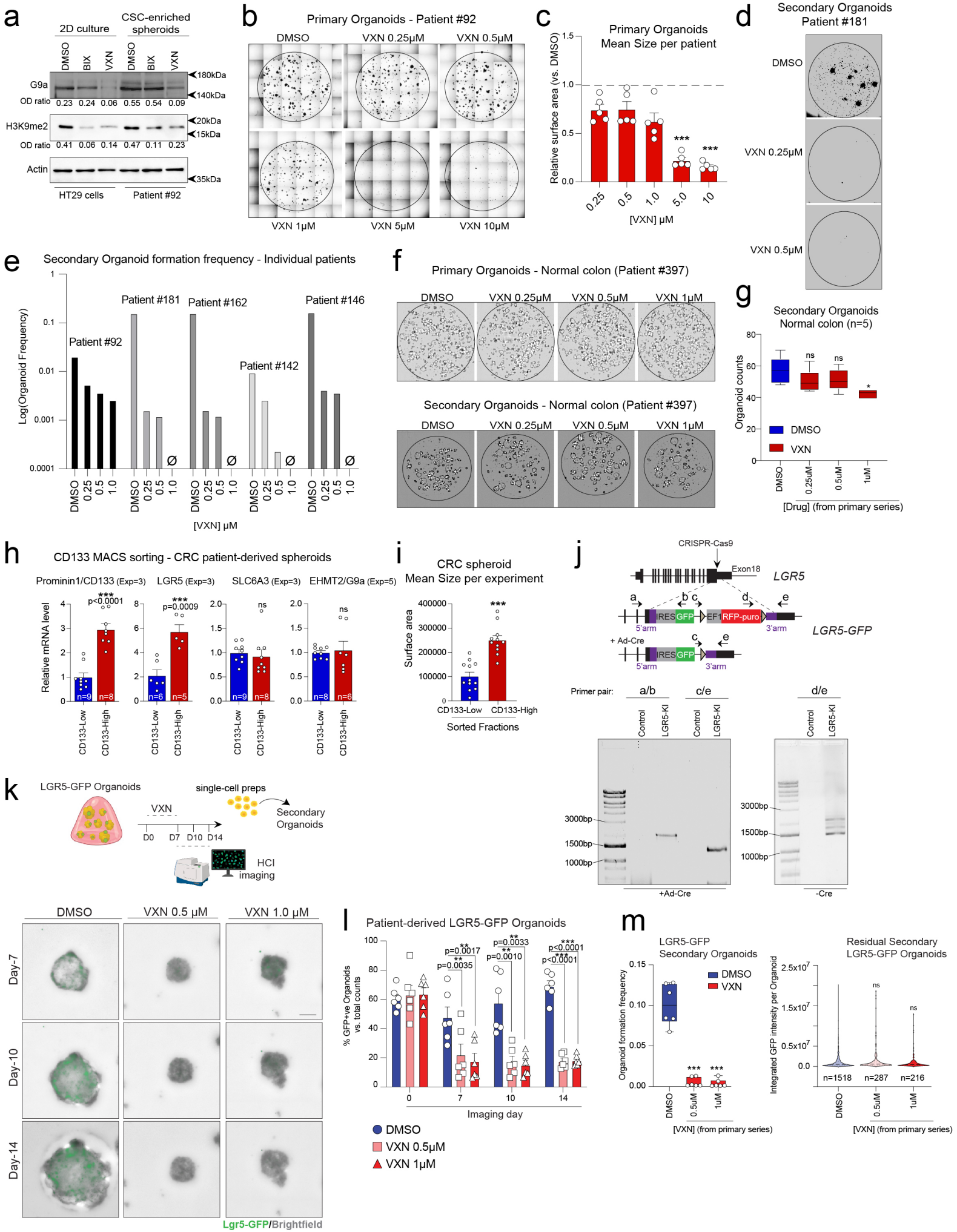

Bergin et al. Extended Data Figure 9

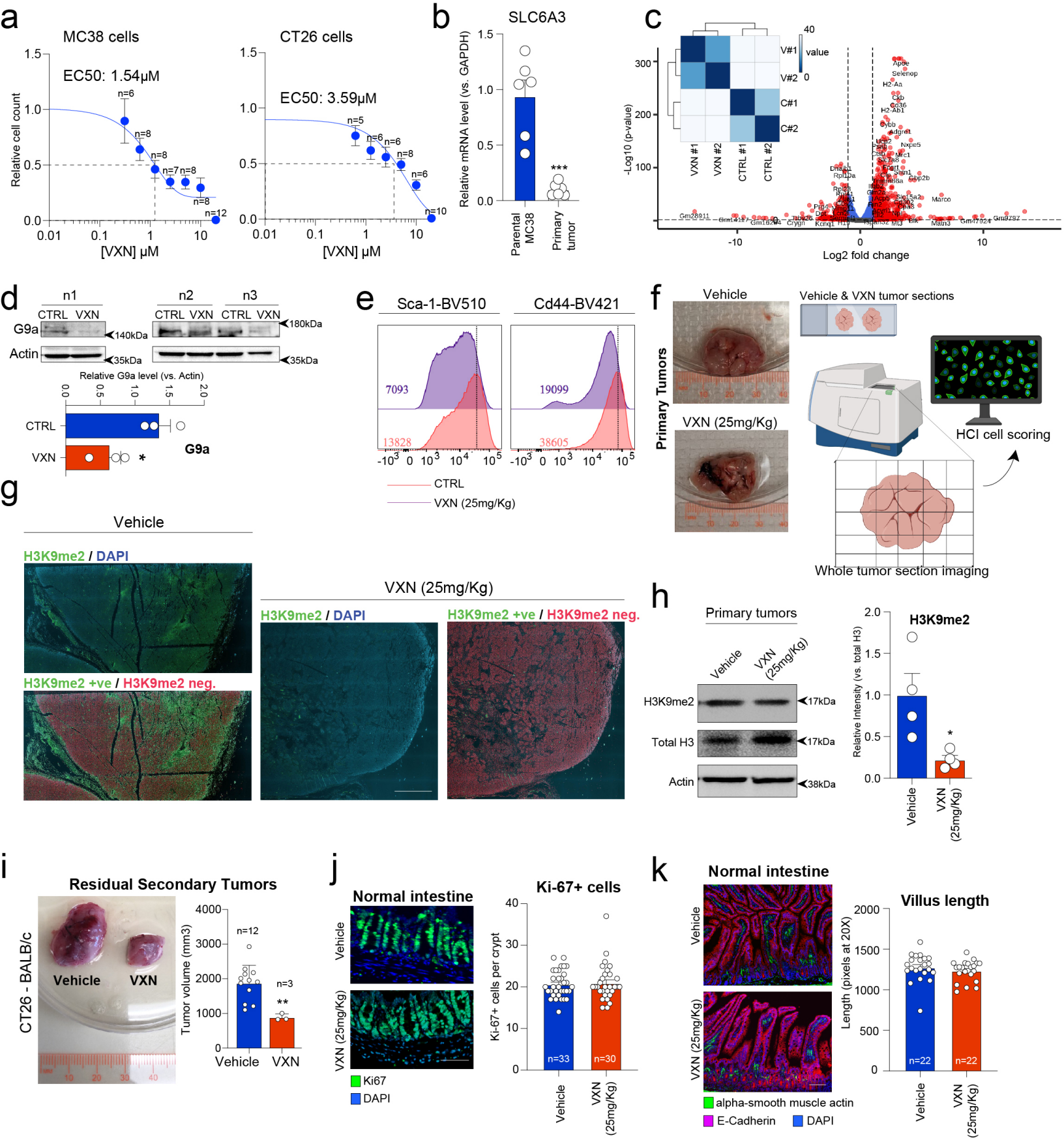

Bergin et al. Extended Data Figure 10